

5-24-2012

Magnetic Resonance Elastography of the Brain: from Phantom to Mouse to Man

Erik Clayton

Washington University in St. Louis

Follow this and additional works at: <https://openscholarship.wustl.edu/etd>

Recommended Citation

Clayton, Erik, "Magnetic Resonance Elastography of the Brain: from Phantom to Mouse to Man" (2012). *All Theses and Dissertations (ETDs)*. 684.

<https://openscholarship.wustl.edu/etd/684>

This Dissertation is brought to you for free and open access by Washington University Open Scholarship. It has been accepted for inclusion in All Theses and Dissertations (ETDs) by an authorized administrator of Washington University Open Scholarship. For more information, please contact digital@wumail.wustl.edu.

WASHINGTON UNIVERSITY IN ST. LOUIS
School of Engineering and Applied Science
Department of Mechanical Engineering and Materials Science

Dissertation Examination Committee:

Philip V. Bayly, Chair

David L. Brody

Mark S. Conradi

Joel R. Garbow

Guy M. Genin

Ruth J. Okamoto

David A. Peters

Larry A. Taber

Magnetic Resonance Elastography of the Brain: from Phantom to Mouse to Man

by

Erik H. Clayton

A dissertation presented to the Graduate School of Arts and Sciences
of Washington University in partial fulfillment of the
requirements for the degree of

DOCTOR OF PHILOSOPHY

May 2012
Saint Louis, Missouri

copyright by
Erik H. Clayton
2012

ABSTRACT OF THE DISSERTATION

Magnetic Resonance Elastography of the Brain: from Phantom to Mouse to Man

by

Erik H. Clayton

Doctor of Philosophy in Mechanical Engineering

Washington University in St. Louis, 2012

Research Advisor: Professor Philip V. Bayly

The overall objective of this study is to develop magnetic resonance elastography (MRE) imaging to better understand brain deformation, brain tissue mechanical properties, and brain-skull interaction *in vivo*. The findings of this study provide parameters for numerical models of human head biomechanics, as well as data for validation of these models. Numerical simulations offer enormous potential to the study of traumatic brain injury (TBI) and may also contribute to the development of prophylactic devices for high-risk subjects (e.g., military personnel, first-responders, and athletes). Current numerical models have not been adequately parameterized or validated and their predictions remain controversial. This dissertation describes three kinds of MRE experiments, conducted in phantom (physical model), mouse, and man. Phantom studies provide a means to experimentally confirm the accuracy of MRE estimates of viscoelastic parameters in relatively simple materials and geometries. Studies in the mouse provide insight into the dispersive nature of brain tissue mechanical properties at frequencies beyond those that can be measured in humans. Studies in human subjects provide direct measurements of the human brain's response to dynamic extracranial loads, including skull-brain energy transmission and viscoelastic properties.

Acknowledgments

Dr. Philip Bayly provided me with an extremely rewarding research project, one with tremendous opportunity. The attention this work has received within the biomechanics community is a reflection on him, his keen foresight, and his penchant for asking the right questions. Above all, he was a great mentor to me.

Drs. Ruth Okamoto, Mark Conradi, Joel Garbow, and Guy Genin provided hours of helpful counsel on this research. Dr. Okamoto spearheaded mechanical bench-top validation studies in this work, and Ms. Kate Wilson assisted her with some of these tests. Dr. Conradi supported MR coil development.

Colleagues in the Biomedical Magnetic Resonance Laboratory are also acknowledged for additional assistance. Dr. Bill Spees and Mr. John Engelbach were key assets in making small animal studies a success.

Drs. Bradley Bolster and Agus Priatna at Siemens Healthcare supported MR elastography pulse sequence development for human studies. Technologists Glenn Foster, Scott Love, and Mark Nolte at Washington University's Center for Clinical Imaging Research assisted with MRI data collection on human volunteers.

Mr. Gene Bulfin kept my computer running and its contents secured, permitting me to sleep soundly each evening. Mr. James Ballard, Ms. Seema Dahlheimer, and Ms. Sandra Matteucci made sure my i's and t's were respectively dotted and crossed. Some numerical simulations performed in this study were completed on the Cloud computing cluster at Washington University's School of Engineering.

Financial support for this work was provided by the National Institutes of Health RO1 NS055951.

Erik H. Clayton

Washington University in Saint Louis
May 2012

To my parents.
&
In memory of Prof. Srinivasan “Sri” Sridharan.
(1942-2011)

Contents

Abstract	ii
Acknowledgments	iii
List of Tables	ix
List of Figures	x
1 Quantitative Imaging Methods for the Development and Validation of Brain Biomechanics Models	1
1.1 Overview	1
1.2 Introduction	2
1.2.1 Mechanical strain and strain rate are crucial factors in traumatic brain injury	2
1.2.2 Computer models are highly promising but require data for parameterization and validation	3
1.2.3 Challenges in making meaningful measurements of brain motion	6
1.3 Technical Requirements for Imaging Rapid Brain Deformation	6
1.3.1 Displacement and strain fields	7
1.3.2 Spatial and temporal resolution, discretization, and noise	8
1.4 Imaging Studies in Physical Brain Surrogates, Animals, and Cadavers	9
1.4.1 Imaging studies of deformation in physical models	9
1.4.2 Visualization of brain deformation in animal studies	10
1.4.3 Visualization of brain deformation in cadavers	12
1.5 Measurement of Human Brain Motion by Phase-contrast Imaging and Magnetic Resonance Elastography	13
1.5.1 Principles of magnetic resonance elastography	15
1.5.2 Estimation of elastic properties from magnetic resonance elastography data	16
1.5.3 Estimation of viscoelastic properties from magnetic resonance elastography data	18
1.5.4 Anisotropic material models	19
1.5.5 Magnetic resonance elastography imaging studies	19
1.6 Discussion and Conclusions	23
1.7 Summary	25
1.8 Specific Aims and Organization of this Work	26

1.8.1	Specific aims	27
1.8.2	Organization of this work	27
2	Theoretical Framework	29
2.1	Overview	29
2.2	A Brief Review of Continuum Mechanics	30
2.2.1	Kinematics	30
2.2.2	Equilibrium	31
2.2.3	Constitutive behavior	33
2.3	Wave Propagation in Unbounded Homogeneous Linear Elastic Media	37
2.3.1	Isotropic media	37
2.3.2	Transversely isotropic media	39
2.3.3	Treatment of viscoelastic effects	40
2.3.4	Energy transport in harmonic waves	42
2.4	Imaging Methods	43
2.4.1	Magnetic resonance elastography	43
2.4.2	Diffusion tensor imaging	46
2.4.3	Application of MRE and DTI data for anisotropic material inversion	48
3	Viscoelastic Properties of Soft Gels: Comparison of Magnetic Resonance Elastography and Dynamic Shear Testing	51
3.1	Overview	51
3.2	Introduction	52
3.3	Methods	54
3.3.1	Gelatin preparation: MRE phantoms and DST samples	54
3.3.2	MRE data acquisition and analysis	55
3.3.3	DST data acquisition and analysis	60
3.4	Results	64
3.4.1	Estimates of viscoelasticity from MRE data	64
3.4.2	Estimates of viscoelasticity from DST data	69
3.4.3	Comparison of MRE and DST viscoelastic estimates	71
3.5	Discussion	71
3.6	Conclusions	77
4	Frequency-dependent Viscoelastic Parameters of Mouse Brain Tissue Estimated by MR Elastography	78
4.1	Overview	78
4.2	Introduction	79
4.2.1	Motivation: traumatic brain injury and other brain pathology	79
4.2.2	Magnetic resonance elastography	80
4.3	Methods	81
4.3.1	Acquisition of spatiotemporal wave fields	81

4.3.2	Steady-state harmonic viscoelastic material response	82
4.3.3	Data Acquisition	85
4.3.4	Data processing	88
4.3.5	Inversion validation	89
4.4	Results	90
4.4.1	Inversion validation	90
4.4.2	Mouse brain elastography	91
4.5	Discussion	94
4.6	Conclusions	98
5	Transmission, Attenuation, and Reflection of Shear Waves in the Human Brain	99
5.1	Overview	99
5.2	Introduction	100
5.3	Materials and Methods	101
5.3.1	Motion-sensitive magnetic resonance imaging	101
5.3.2	Measurement procedure and equipment	103
5.3.3	Analysis of the distortional component of motion	105
5.4	Results	111
5.4.1	Extracranial pressure and brain deformation	111
5.4.2	Quantitative analysis of shear wave energy transmission into the brain	113
5.4.3	Quantitative analysis of shear wave energy attenuation within the brain	113
5.4.4	Reflection of shear waves at anatomical interfaces	113
5.4.5	Estimates of viscoelastic parameters from shear wave fields	114
5.5	Discussion	116
5.6	Conclusions	118
5.7	Supplementary Material	120
6	Preliminary Work: 3D MRE and DTI in Human Subjects	121
6.1	Overview	121
6.2	3D Strain Dilation and Distortion Estimated in the Living Human Brain from MR Images of Propagating Shear Waves.	122
6.2.1	Introduction	122
6.2.2	Methods	122
6.2.3	Results & Discussion	124
6.2.4	Conclusions	124
6.3	Estimating Transversely Isotropic Material Parameters with Magnetic Resonance Elastography and Diffusion Tensor Imaging	126
6.3.1	Introduction	126
6.3.2	Methods	127
6.3.3	Results & Discussion	129

6.3.4	Conclusions	131
7	Summary, Conclusions, and Future Directions	133
7.1	Summary of Work	133
7.2	Limitations	134
7.2.1	Imaging resolution and signal	135
7.2.2	Wave propagation in viscoelastic media	135
7.2.3	Isotropic viscoelastic inversion	136
7.2.4	Wave interference and shadowing	136
7.2.5	Anisotropic inversion	137
7.3	Future Directions	137
7.4	Conclusion	138
Appendix A	Local Least-squares Inversion	139
Appendix B	A Method to Temperature-correct Shear Moduli	142
Appendix C	Design of an Actively-decoupled Transmit Volume Coil for Small Animal MRI	145
References	148
Vita	164

List of Tables

1.1	Magnetic resonance elastography (MRE)-based estimates of brain elastic or viscoelastic mechanical properties (healthy living human subjects).	24
3.1	DST sample properties ($n = 16$).	70
3.2	Rheological model best-fit parameters (DST data).	71
4.1	Validation of inversion methods. Estimates of viscoelastic parameters were obtained from simulated (FE) data for each of three inversion methods. (Poisson's ratio of 0.49.)	91
4.2	Material property estimates of <i>in vivo</i> mouse brain tissue measured by MRE.	95
5.1	Viscoelastic properties of brain tissue (mean ± 1 standard deviation).	114
6.1	Properties of simulated TI medium. Engineering constants E_T , E_L , μ_T , and μ_L (Pa). Poisson ratios ν_{LT} , ν_{TL} , and ν_T (dimensionless).	128
6.2	Properties of simulated TI medium in Spencer's [156] notation (Pa).	128
6.3	Inversion performance in a homogeneous TI medium as the axis of material symmetry $\bar{\mathbf{a}}$ is varied. ($\cos \theta = \bar{\mathbf{a}} \cdot [1, 0]$)	130
6.4	Inversion performance in heterogeneous anisotropic media. In domain I-IV a unique axis of material symmetry $\bar{\mathbf{a}}$ is specified. ($\cos \theta = \bar{\mathbf{a}} \cdot [1, 0]$) Domain III is mechanically isotropic, so theoretically $\mu_T = \mu_L$. (True μ_T and μ_L are 750 Pa and 1500 Pa, respectively. True μ_{iso} is 1500 Pa.)	130
C.1	Bill of materials.	147

List of Figures

1.1	The technology underlying the physical discretization of computational models of the human head can now produce remarkable anatomic accuracy and predictions of mechanical fields at very fine spatial resolution. However, mathematical models and material data for the tissues, structures, and interactions within the brain have lagged behind, as have data for validation of model predictions. Adapted from Reference [61].	5
1.2	The earliest estimates of acceleration-induced shear strain fields within the human brain are those of Holbourn [63], who observed shear deformation patterns within gelatin-filled skulls due to occipital impact and angular acceleration/lateral impact. The scale bar represents the relative magnitude of shear in arbitrary units. Recent magnetic resonance imaging data have shown that shear strain patterns within a gelatin-filled skull differ fundamentally from those within a living human owing to several factors including brain architecture, vasculature, and attachment to the skull. Reproduced from Reference [63].	9
1.3	High-speed and high-resolution videography techniques have enabled studies of physical models of the brain that undergo large deformations at high strain rates. The skull of a miniature pig was filled with two layers of silicone gel; a grid pattern was painted between the layers. The assembly was subjected to angular accelerations of 50,000–200,000 rad/s ² while grid deformation was recorded at 1,000 frames per second. Adapted from Reference [102].	10
1.4	Progress on understanding acceleration-induced strain in the animal brain in situ has been made through high-speed video studies. The exposed flat surface of the hemisected brain of a juvenile pig was marked with India ink (a), and the skull and brain were covered by a layer of lubricant and by a transparent Plexiglas cover plate. Strain fields were estimated from marker positions (b) during an angular acceleration pulse with a peak magnitude of $\approx 10,000$ m/s ² . Reproduced from Reference [65].	11
1.5	Phase-contrast MRI allows high spatial resolution imaging of the three-dimensional displacement and strain fields in the moving brains of live human subjects. Shown here is the strain-rate tensor field in the human brain due to normal pulsatile motion of the brain parenchyma. Box icons are color coded and scaled to represent the eigenvalues λ_i and scaled eigenvectors v_i of the strain-rate tensor at each voxel. Adapted from Reference [132].	14

1.6	Magnetic resonance elastography (MRE) produces estimates of intracranial displacement fields observed in response to dynamic pressure loading of the skull. These can be inverted to estimate spatially varying mechanical properties of brain tissue. Example displacement fields shown here are obtained from a single-slice multifrequency MRE experiment. (a) Standard MR anatomical images: T1-weighted (T1w), proton density (PD), and T2-weighted (T2w) contrast. (b) Wave images and parameter fields. U' and U'' denote the real and imaginary parts of the first harmonic component $U(x, y, \omega)$ of the displacement field. The complex modulus images (G' and G'') denote the real and imaginary parts of the complex shear modulus $G^*(x, y, \omega)$. The driving frequencies are given above the columns. Reproduced from Reference [142].	21
1.7	Magnetic resonance elastography (MRE) provides noninvasive estimates of living brain tissue in human volunteers. MRE-based estimates of brain tissue shear modulus vary among different studies but lie within the range of estimates obtained <i>in vitro</i> by direct mechanical tests. Adapted from Reference [24].	22
2.1	Deformation of two particles, A and B, in a deformable body D.	30
2.2	Stresses acting on an infinitesimal rectangular parallelepiped of volume $V = \delta x_1 \delta x_2 \delta x_3$.	32
2.3	(a) Transversely isotropic material model with fibers aligned with the x_1 -axis. (b-d) Application of shear stress along a face produces a corresponding shear strain in proportion to the shear modulus. In transversely isotropic media there are two shear moduli: μ_T describes shear in a plane normal to the symmetry axis, and μ_L in planes parallel to the symmetry axis. Biological media often exhibit $\mu_L > \mu_T$. ($\gamma_{ij} = 2\epsilon_{ij}$, for $i \neq j$.)	35
2.4	As a consequence of complete material symmetry, wave propagation in isotropic media will always produce three distinct waves, each corresponding to the direction of wave polarization. In general, this is not true for waves in anisotropic media. Wave degeneracy and quasi waves may present.	39
2.5	The basic concept of MRE imaging is described. Motion-sensitive MR image is used to record shear wave propagation in tissue. A tissue-simulating phantom with an embedded cylindrical inclusion of stiffer material is shown here. The governing equations of motion are inverted to produce an elastogram - an image with contrast proportional to shear modulus. Adapted from Reference [82].	43
2.6	In a magnetic resonance elastography pulse sequence, specialized magnetic-field gradients encode harmonic tissue motion produced by an actuator as a shift in NMR signal phase. Applying multiple motion-encoding gradients (MEG) on different channels simultaneously permits acquisition of any motion component. Temporal variations in motion are recorded by time-delaying MEG events relative to the applied mechanical actuation (ϕ). A 1-cycle MEG (dashed) is shown on each gradient channel, so the recorded motion would be perpendicular to an oblique plane in the imaged body. RF-pulse and magnetic-field gradient events required to create a standard MR image are also shown. Reproduced from Reference [29].	44

2.7	A spin-echo magnetic resonance imaging pulse sequence can be modified to measure diffusion by the addition of diffusion weighting magnetic-field gradients (DWG) on each side of the 180° refocusing RF pulse. Applying DWG of various duration (δ), spacing (Δ), and magnitude (G) along one or more gradient axes simultaneously creates diffusion weighted images (DWI) whose signal intensities can be related to the incoherent displacement of water of varying signal intensity.	47
2.8	(a) Each diffusion weighted image corresponds to a specific b_{ij} and is related to the amplitude and direction of an applied diffusion magnetic-field gradient vector G_j . Multi-variable regression permits reconstruction of the diffusion tensor with as little as seven non-collinear measurements. (b) Principal directions of diffusivity are obtained by diagonalizing the diffusion tensor and have been shown to be aligned parallel (λ_1) and perpendicular (λ_2, λ_3) to tissue fibers. (S002)	49
2.9	Diffusion tensor data can be used to align axes of material symmetry (x_i) with MRE displacement data acquired in a laboratory reference frame (X_i). (a) The native material orientation with respect to laboratory coordinate system. (b) The diffusion ellipsoid calculated from DTI data. (c) The eigenvectors of the diffusion tensor can be used transformation of material orientation to laboratory coordinates.	50
3.1	MRE experimental setup. (a) MR phantom; (b) orientation of phantom in scanner. The vertical dashed lines show approximate bounds of the transverse planes imaged. Reproduced from Reference [119].	55
3.2	A gradient echo MR imaging sequence was modified to acquire elastography data. Sinusoidal motion-encoding magnetic-field gradients (MEG) are included with standard RF and magnetic-field gradient events required to form an MR image. MEGs are synchronized with the applied mechanical motion by the phase shift parameter Φ . A 3-cycle MEG (dashed) is shown on each gradient channel. In this example, motion-encoded phase images are acquired with contrast proportional to displacements perpendicular to an oblique plane in the imaged body.	56
3.3	Dynamic shear test (a) sample and (b) setup. Samples were placed on the tester and subjected to small amplitude vibrations (0–200 Hz). Adapted from Reference [119].	60
3.4	Dynamic shear test sample nomenclature used in Equations 3.7–3.13. Adapted from Reference [119].	62
3.5	Images of the u_z displacement field support the plane wave assumption used for MRE data inversion. (a) Axial and (b) coronal images of the displacement field show that within the analysis volume, boxed in green, planes of wave symmetry exist along the z -axis. (250 Hz) Adapted from Reference [119].	64

3.6	Displacement fields and viscoelastic parameters at each excitation frequency. (top) Real and imaginary components of the fundamental time harmonic of the through-plane displacement u_z are shown for slice 6 of 11. (bottom) Elastograms calculated from the displacement fields after spatially filtering with a 3D Gaussian kernel of $13 \times 13 \times 7$ voxels ($3.0 \times 3.0 \times 3.0 \text{ mm}^3$). The diameter of the gelatin container was 45 mm. Reproduced from Reference [119].	65
3.7	Real and imaginary parts of the complex displacement field $U_z(x, y)$ obtained by MRE at (a) 150 and (b) 350 Hz. The orientation of the line-path ROI used for comparison of MRE data with the closed-form solution is shown as a yellow dashed line. Real and imaginary parts of unfiltered MRE displacement data (solid line) and the predicted closed-form solution (dotted line) are compared at (b) 150 Hz and (d) 350 Hz. Reproduced from Reference [119].	67
3.8	Viscoelastic shear moduli estimated from MRE displacement data via: direct inversion (solid line), and axisymmetric closed-form solution (dashed line). Error bars + or - 1 std. Adapted from Reference [119].	68
3.9	Viscoelastic shear moduli by direct inversion of MRE displacement data: as acquired (solid line), temperature corrected (dashed line). Error bars + or - 1 std. Adapted from Reference [119].	68
3.10	Typical results of DST. (a) Magnitude and (b) phase angle of apparent shear modulus. The phase angle changes rapidly at each shear wave peak. Experimental data (solid line) and best fits to standard linear solid (dotted line), fractional Zener (dashed line), and springpot (dash-dot line) models are shown. (c) Predicted G' and G'' from 0 to 400 Hz based on best-fit model parameters from test are shown. Reproduced from Reference [119].	69
3.11	Comparison of viscoelastic shear moduli estimated from DST (solid line) and MRE (dashed line) (DST: $n = 16$; MRE: $n = 6$). A fractional Zener model was used for DST parameter extraction and to extrapolate behavior beyond measured frequency range (dash-dot line). MRE data shown were obtained by direct inversion and temperature corrected. Error bars ± 1 std. Adapted from Reference [119].	72
3.12	Causality of MRE estimated viscoelastic moduli was checked by a local, low-order Kramers-Kronig (K-K) approximation (Equation 3.14). K-K was used to predict the storage modulus from the measured loss modulus. Experimental measurements (solid lines, circles, error bars ± 1 std); predicted storage modulus (dashed line, squares); and piecewise linear fit of loss modulus (dash-dot line, crosses). Adapted from Reference [119].	74

4.1	The modified spin echo magnetic resonance pulse sequence used for elastography data acquisition. In addition to RF and magnetic-field gradient events required to create a spin echo MRI, sinusoidal, motion-encoding gradients (MEG) are placed on each side of the 180° RF pulse. MEG events and the mechanical actuation signal may be temporally shifted by the parameter Φ . By varying the delay Φ temporal variations in the wave field are recorded. In this example, a 1-cycle MEG (dashed) is shown on each gradient channel. As a result, motion-encoded phase images are acquired with contrast proportional to displacements perpendicular to an oblique plane in the imaged body. Reproduced from Reference [29].	86
4.2	The custom-built stereotaxic mouse head holder used for elastography studies. The head of each mouse was secured between the ear bars and incisor bar. Light tension on the incisor bar ensures contact throughout the actuator stroke. An MR-compatible, amplified piezoceramic actuator drives the incisor bar harmonically, inducing mechanical vibration of the mouse skull along the rostral-caudal axis. Reproduced from Reference [29].	87
4.3	(Top) Finite element model geometry and imposed boundary conditions used for validation of the inversion techniques. (Bottom, left) Real and imaginary parts of the fundamental harmonic displacement component u_3 . (Bottom, right) Estimates of the viscoelastic parameters shown as functions of location in the central plane. (2 mm vertical scale bar shown.) Reproduced from Reference [29].	89
4.4	Example anatomical images, displacement fields and estimates of viscoelastic parameters for each excitation frequency. (Row 1): Magnitude images of a central (A/P) region of the brain; four contiguous slices 250 μm thick were averaged (1 mm total thickness). (Rows 2 & 3): External mechanical motion induces propagating waves within mouse brain tissue. The real, U'_3 , and imaginary, U''_3 , component of the fundamental harmonic of the through-plane displacement is shown for slice two of three contiguous slices used for inversion. (Rows 4 & 5): Elastograms (images of storage modulus, G' , and loss modulus, G'') calculated from the displacement fields of Rows 2 & 3. Reproduced from Reference [29].	92
4.5	The frequency dependence of the average viscoelastic mechanical parameters estimated for the central region of the mouse brain ($n = 6$). Estimates were obtained by fitting a single motion component of the complex displacement harmonic to Equations 4.6. A power-law fit of the form $G(\omega) = \kappa\omega^\alpha$ is shown as a dashed line. (G' : $\kappa = 0.04 \times 10^{-3}$, $\alpha = 1.29$; G'' : $\kappa = 1.24 \times 10^{-3}$, $\alpha = 0.83$) Reproduced from Reference [29].	93
4.6	Comparison of the apparent dispersive properties of mouse brain tissue as obtained by three different inversion methods: “1D” - Equations 4.6, $i = 3$; “3D” - Equations 4.6, $i = 1, 2, 3$; “3D-curl” - Equations 4.10. Mechanical property estimates obtained from fitting 3D displacement fields to the viscoelastic equations of motion are within a standard deviation of estimates obtained by fitting only a single displacement component. (1D: $n = 6$; 3D: $n = 1$). Reproduced from Reference [29].	94

4.7	Average, root-mean-square (RMS) shear-strain $\frac{\partial u_3}{\partial y}$ amplitudes (left); and average, RMS shear-strain rates $\frac{\partial^2 u_3}{\partial t \partial y}$ observed in 1D experimental data (right); $n = 6$, standard deviations shown. Reproduced from Reference [29].	97
5.1	(a) High resolution anatomic images of the brain slice in which displacement data were recorded highlight anatomic structures and boundaries (e.g., gray and white matter, lateral ventricles, etc.). Displacement data were acquired on approximately transverse slice planes through the superior corpus callosum. (b) In-plane spatiotemporal displacement Fields were used to calculate the through-plane component of distortion Γ . Transmission, attenuation, and reflection of distortion within the living human cranium were analyzed in this study. (S014, 45Hz)	103
5.2	(a) Schematic diagram of the experimental apparatus for inducing shear waves in the brain by extracranial pressure loading. (b) The specialized gradient-recalled echo (GRE) magnetic resonance imaging pulse sequence used for data acquisition. In addition to the standard radio frequency (RF) pulses and orthogonal magnetic-field gradient orientations (SS: slice select, RO: readout, PE: phase encode) required to create the GRE MR image, a trapezoidal motion-encoding gradient is included.	104
5.3	(a-f) Vector fields of amplitude-weighted average propagation direction in a homogeneous cylinder of gelatin in which both the container and a central rod are coupled to a piezoelectric actuator. Vector fields are superimposed on (a,b) estimated distortion fields Γ and (c,d) high resolution “anatomical” images. (e,f) Divergence of the propagation direction field highlights energy production (source) and dissipation (sink). (a,c,e) At 150 Hz shear waves propagate predominantly outward. (b,d,f) At 400 Hz shear waves propagate both inward and outward, and interfere destructively at intermediate radial locations. Standing waves due to constructive interference are also possible. Standing waves in this system would be indicated by distortion fields with significant amplitude but near-zero average propagation velocity.	109
5.4	The presented viscoelastic inversion scheme was tested on MRE data obtained in gelatin [119]. (a) Distortion wave field (Γ). Viscoelastic moduli (b) G' and (c) G'' . (150Hz)	110
5.5	(Top) Waveforms of the pressure applied to the skull in one subject: (a) 45 Hz; (b) 60 Hz; (c) 80 Hz. (Bottom) Distortion wave fields (Γ , dimensionless) observed in the human brain in response to the applied pressure fields above. Arcs on the left and right denote the locations of passive actuator pads. (S008)	111

5.6	Pressure-normalized distortion Γ/P (Equation 5.8) was used to evaluate transmission and attenuation. (a) The amplitude of Γ/P was spatially averaged over the entire brain (shown right) and plotted for each subject. Subject-to-subject variability exists; however when data were acquired at all three frequencies in the same subject, the amplitude consistently decreased with increasing acoustic frequency. (b) The amplitude of Γ/P was spatially averaged in a 1.5 cm-wide annular region of brain tissue immediately interior of the skull/dura mater (shown right) and plotted as a function of acoustic frequency. Transmission coefficients were extracted by exponential curve fit: $\Gamma/P = A_f \exp(-\beta_f f)$; min $\beta_f = 0.046 \text{ Hz}^{-1}$ (S014), max $\beta_f = 0.058 \text{ Hz}^{-1}$ (S009), mean $\beta_f = 0.050 \text{ Hz}^{-1}$. (c) The amplitude of Γ/P was regionally averaged in concentric annular elliptical rings (shown right) and plotted as a function of depth from the brain skull boundary. Attenuation coefficients were extracted by exponential curve fit: $\Gamma/P = A_d \exp(-\alpha d)$; 45 Hz: $\alpha = 23.7 \text{ m}^{-1}$; 60 Hz: $\alpha = 51.1 \text{ m}^{-1}$; 80 Hz: $\alpha = 54.3 \text{ m}^{-1}$	112
5.7	Vector fields of amplitude-weighted average propagation direction superimposed on (a-c) estimated distortion fields and (d-f) high resolution anatomical images in one human subject at three frequencies. Shear waves in the brain appear to propagate inward from the brain-skull boundary toward the ventricles. (g-i) Divergence of the propagation direction field at the anterior/posterior falx and above the tentorium indicates that these membranous structures may act like sources of shear wave excitation. (a,d,g) 45 Hz; (b,e,h) 60 Hz; (c,f,i) 80 Hz. (S008)	115
5.8	Spatial maps of the viscoelastic material properties of intact, living human brain were calculated using a distortion-based LFE approach (Equation 5.13). (a) T1-weighted anatomical image of the analysis slice. Viscoelastic moduli (b) G' and (c) G'' . (S005, 45Hz)	116
5.9	Vector fields of amplitude-weighted average propagation direction superimposed on the distortion field Γ in each subject at 45 Hz.	120
5.10	Divergence of propagation direction vector fields in each subject at 45 Hz.	120
6.1	Oscillatory pressure was generated by an acoustic actuator and transmitted to a passive actuator pad positioned near the right pterion bone via flexible tubing.	123
6.2	Measured displacement fields shown above were used to calculate strain and local rotation fields (S002, Slice 3 of 5).	125
6.3	Calculated strain fields in the living intact human brain resulting from extracranial acoustic pressure load (S002).	125
6.4	Calculated local rotation fields indicate significant distortional wave motion (S002).	126

6.5	A thin slab finite element model used for inversion validation. Subdomains are color coded and labeled I-IV. All subdomains are connected so that displacement continuity exists. The four quadrants create one monolithic structure; however, the material properties within each subdomain may be uniquely specified. Harmonic steady-state motion, polarized in the x_3 -direction, was applied to the sides of domains I, II and IV, simultaneously. The wave normals associated with this motion are denoted as $\bar{\mathbf{n}}_1$ and $\bar{\mathbf{n}}_2$. Orientation of the material symmetry axis $\bar{\mathbf{a}}$ is specified as $\cos \theta = \bar{\mathbf{a}} \cdot [1, 0]$. Plane symmetry boundary conditions were applied as shown.	127
6.6	Validation of the TI inversion algorithm on a homogeneous anisotropic medium in various orientations. The material symmetry axis orientation $\bar{\mathbf{a}}$ and u_3 -displacement field are simulated inputs to the inversion algorithm. Elastograms of shear moduli μ_T and μ_L are algorithm outputs. (True μ_T and μ_L are 750 Pa and 1500 Pa, respectively.)	129
6.7	Validation of the TI inversion algorithm on a heterogeneous medium. The material symmetry axis orientation $\bar{\mathbf{a}}$ and u_3 -displacement field are simulated inputs to the inversion algorithm. Elastograms of shear moduli μ_T and μ_L are algorithm outputs. Note subdomain III is an isotropic material. (True μ_T and μ_L are 750 Pa and 1500 Pa, respectively. True μ_{iso} is 1500 Pa.) . . .	131
6.8	DTI and MRE data have been acquired in human brains. The principal diffusion direction $\lambda_1(\bar{v}_1)$ is used to orient the axis of material symmetry \bar{a} . In each voxel, \bar{a} and displacement components u_1, u_2, u_3 are specified. It may be possible to estimate mechanical anisotropy locally with these measurements. This will be the target of future studies.	132
A.1	The concept of total least squares versus ordinary least squares best-fit. Notice that error in both x and y are considered in a total least squares fit (green), $\lambda = 1$ in the case presented. Only error in y is considered in an ordinary least squares fit (red).	140
B.1	(a) Normalized components of the viscoelastic shear moduli estimated from MRE displacement data at 150 Hz and 400 Hz taken over a period of 7 hours. Measurements of G'/G''_{eq} (circles) and G''/G''_{eq} (squares) are shown with open symbols (150 Hz) or filled symbols (400 Hz). Solid and dashed lines show decaying exponential function for G'/G''_{eq} and G''/G''_{eq} respectively, with parameters given in text. (b) Temperature measured using probe at center of another gel phantom. The gel reached an equilibrium temperature of 21°C after 4 hours. Dashed line shows exponential fit to temperature with time constant of 1.3 hours. Adapted from [119].	143
C.1	Coil form components.	146
C.2	Circuit diagram.	146
C.3	The completed coil.	147

Chapter 1

Quantitative Imaging Methods for the Development and Validation of Brain Biomechanics Models

1.1 Overview

Rapid deformation of brain tissue in response to head impact or acceleration can lead to numerous pathological changes, both immediate and delayed. Modeling and simulation hold promise for illuminating the mechanisms of traumatic brain injury (TBI) and for developing preventive devices and strategies. However, mathematical models have predictive value only if they satisfy two conditions. First, they must capture the biomechanics of the brain as both a material and a structure, including the mechanics of brain tissue and its interactions with the skull. Second, they must be validated by direct comparison with experimental data. Emerging imaging technologies and recent imaging studies provide important data for these purposes. This review describes these techniques and data, with an emphasis on magnetic resonance imaging approaches. In combination, these imaging tools promise to extend our understanding of brain biomechanics and improve our ability to study TBI *in silico*.

A portion of material presented in this chapter is accepted for publication in Annual Review of Biomedical Engineering (Bayly, Clayton, Genin, 2012).¹

1.2 Introduction

1.2.1 Mechanical strain and strain rate are crucial factors in traumatic brain injury

Traumatic brain injury (TBI) is a major health problem in both children and adults; approximately 1.7 million new cases arise each year in the United States [38]. In 1999, more than 5 million Americans had disabilities resulting from TBI, incurring costs estimated at \$56.3 billion annually [167]. TBI is a global health issue, with the incidence of brain injury due to traffic accidents even higher in Latin America and sub-Saharan Africa (150–170 per 100,000) than in the United States and Europe [66]. Mild TBI is the most prevalent form of head injury, with more than 300,000 sports-related concussions per year in the United States [155]. Concussions have been observed in American football at skull accelerations estimated to be in the range of 800–1,000 m/s² [124]. Furthermore, blast-induced TBI has emerged as one of the most important medical problems related to military deployment [62]. The effects of brain trauma can be lasting – TBI is an established risk factor for Alzheimer’s disease, especially in combination with the $\epsilon 4$ allele of apolipoprotein E [109, 96]. The mechanism of this increased risk is not clear, but it is plausible that TBI affects the brain via mechanically induced changes in handling and metabolism of amyloid β peptide, as supported by studies reporting accelerated amyloid β deposition following TBI in mice expressing mutant human amyloid precursor protein [153, 171].

The physical process underlying most TBI is rapid deformation of brain tissue caused by acceleration of the skull [46]. In concussions, mild tissue strain is thought to cause diffuse, mechanically induced depolarization of cortical neurons [147]. In severe trauma, diffuse axonal injury occurs throughout the white matter of the brain, as

¹Author Contributions: P.V.B. directed and performed the literature review and wrote the article. E.H.C. performed the literature review, adapted figures, prepared tables, and co-wrote the article. G.M.G. performed the literature review and co-wrote the article.

axons are stretched beyond a physiological injury threshold [46]. The clearest studies of the relationship between rapid neural tissue deformation and injury have been performed outside the brain – for example, on the guinea pig optic nerve [8] and in *in vitro* cell cultures or tissue slice preparations [66, 43, 67]. These studies show clearly the effects of large strain on functional and morphological properties of axons (e.g., 13). Although *in vitro* experiments are essential to understand the pathology of brain injury, to be relevant they should replicate the key physical conditions experienced by neurons and axons in the intact brain.

For decades, the details of brain deformation in human TBI have remained the subject of much speculation and indirect study. An example is injury in the frontal lobe of the brain that presents from occipital impacts far from the impact site—known as contrecoup injury [46, 130]. Many explanations of contrecoup injury have been proposed [147, 130], but definitive measurements of brain deformation needed to evaluate competing hypotheses have only recently become available. This review summarizes the state of the art in acquiring these data.

1.2.2 Computer models are highly promising but require data for parameterization and validation

Computer simulations of TBI offer enormous potential, especially to replace experiments that cannot be performed for ethical reasons (e.g., injury-level accelerations in humans) or that are extremely difficult or expensive. However, simulations require accurate models of tissue and tissue connectivity and, most importantly, experimental data to confirm the accuracy and predictive ability of these models. Lacking such data, numerical predictions of brain deformation remain uncertain. One of the most important reasons to measure deformation in the human brain is to improve the quality and credibility of numerical models.

Computer models of slow (quasi-static) brain deformation have been developed by Miga and coworkers [104, 105], Miller and coworkers [106, 108, 107], and Ji et al. [68] for neurosurgical applications. The goals of such models are to update presurgical magnetic resonance (MR) or computed tomography (CT) scans of the brain during surgery and to assist in surgical planning. Although these quasi-static deformations

are not a focus of this review, several commonalities exist in the associated imaging needs and technologies, including the need for validation, the need for accurate material data, and the need for careful consideration of boundary conditions.

A great many finite-element (FE) models describe human head and brain motion during rapid acceleration [163, 164, 181, 175, 75, 61]. We highlight one example to describe both the successes and challenges associated with this type of modeling and to set the stage for the role of imaging studies. The Wayne State University Brain Injury Model [182] is a FE model of an adult human male head, with accurate geometry and anatomical features [e.g., scalp, skull, dura, falx cerebri, tentorium, blood vessels, white and gray matter, cerebrospinal fluid (CSF)] represented by different material properties in different interacting regions, each connecting to its neighbors through prescribed boundary and interaction conditions. Although the technology available to input detail into this model is remarkable, that available to validate the model has lagged behind. The state of the art has been comparison with intracranial pressure data from cadaver impact tests [114, 169]. Measurements of pressure are coarse, and a broad range of tissue models can replicate a single pressure trace. Needs for spatial resolution and for validation at the level of the parameters implicated in TBI, such as tissue strain and strain rate fields, motivate the emerging class of noninvasive technologies described in this review.

Similarly, efforts to understand and prevent blast-induced TBI have motivated development of mathematical models of blast-induced pressure fields affecting the human head. The mechanical loading applied in such models takes advantage of decades of theoretical development and experimental validation of blast physics. These models also include detailed anatomy of the head and brain, determined by magnetic resonance imaging (MRI) (Figure 1.1). However, constitutive models of tissue used in these simulations are simplified and not calibrated to direct mechanical tests of tissue response in vivo. Taylor & Ford [165] use linear viscoelastic tissue, and Nyein et al. [117] use isotropic, hyperelastic brain tissue augmented with model viscoelastic behavior. These simplified models may be appropriate to predict the brain's responses to blast-induced mechanical loadings, but the accuracy of such predictions is yet to be established, which underscores the importance of direct comparison with experimental measurements.

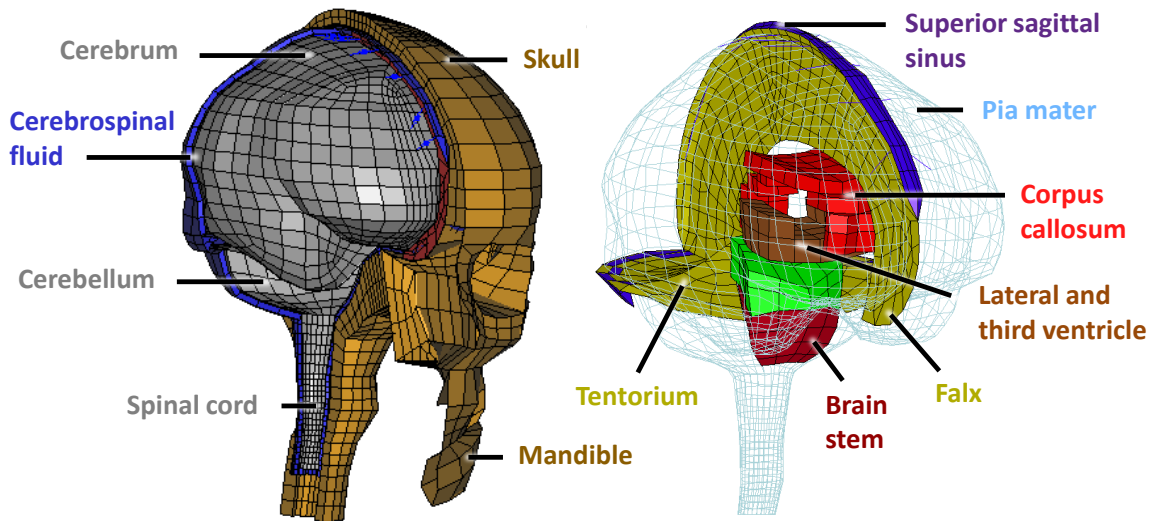


Figure 1.1: The technology underlying the physical discretization of computational models of the human head can now produce remarkable anatomic accuracy and predictions of mechanical fields at very fine spatial resolution. However, mathematical models and material data for the tissues, structures, and interactions within the brain have lagged behind, as have data for validation of model predictions. Adapted from Reference [61].

In summary, the development of imaging-based technologies for brain biomechanics is driven by three needs. The first is the need to estimate and validate material properties that serve as inputs to mechanical models. The brain is a heterogeneous structure whose different constituents (e.g., cortical gray matter, white matter, sub-cortical gray matter, and cerebellum) likely have different nonlinear, viscoelastic, and anisotropic mechanical properties. The second is the need to estimate and validate boundary conditions and interaction models. The brain is surrounded by CSF and attached by a variety of materials (vessels, membranes, sheathed nerves) to the skull. The skull has several bony prominences, particularly at the base, that restrict motion of the brain relative to the skull. The membranes surrounding the brain (pia mater, arachnoid mater, and dura mater) are all stiffer than the brain. The dura mater includes structures (the falx cerebri and tentorium) that clearly interact with and constrain the motion of the brain parenchyma. The third need is to test hypotheses and validate models and their predictions. For example, interfacial structures might be critically important to the mechanisms of impact- and blast-induced TBI, but data to test this hypothesis are only beginning to become available.

1.2.3 Challenges in making meaningful measurements of brain motion

The human brain is well-hidden, well-protected, delicate, metabolically active, and anatomically complex. These properties make the study of brain deformation daunting. Brain tissues of other large mammals have material and neurophysiological properties similar to those of the human brain, but geometry and boundary conditions unique to the human brain are likely important in determining its response to impact or blast. Cadaver studies are complicated by numerous factors, especially changes in the mechanical state of the brain and its environment *post mortem* [44]. Accordingly, imaging studies to illuminate TBI have been pursued along two general lines: (a) animal and cadaver studies that address general mechanisms of injury, particularly the material response of brain tissue, and (b) human studies that are noninvasive and that target TBI indirectly by determining the response of the intact brain to subinjurious mechanical stimuli.

In this review, we summarize the contributions of imaging to the understanding of TBI and to the development of accurate numerical simulations of brain biomechanics. We emphasize recent MRI-based studies, because they provide full-field measurements of time-varying deformation in the living brain. Finally, we discuss some of the many remaining challenges and possibilities for future work in this area.

1.3 Technical Requirements for Imaging Rapid Brain Deformation

TBI involves spatial and temporal variations in brain motion. Quantification of intracranial deformation has been approached in two ways. The first, exemplified by the studies of Hardy et al. [57] and Zou et al. [183], involves tracking a small number of physical markers. These authors imaged neutrally buoyant markers embedded within a cadaveric brain, using high-speed X-ray images taken in two orthogonal planes. Triangulation of marker positions over time yielded a time course of their displacements. The second approach uses the image contrast itself, typically resulting in much higher

spatial resolution. This method leads to a sequence of two-dimensional (2D) images (or 3D image volumes) acquired over time and stored as 3D arrays ($M \times N$ pixels $\times P$ sample times) or 4D arrays ($M \times N \times K$ voxels $\times P$ times). We summarize in this section the analysis of strain and deformation needed to interpret these data.

1.3.1 Displacement and strain fields

Deformation estimation typically begins with image processing to extract displacement fields. Deformation is quantified by comparing a deformed configuration of the imaged brain with an undeformed reference configuration of the imaged brain, in terms of a displacement field and its spatiotemporal derivatives. The location of each material point of the body is defined by its position \mathbf{X} in the reference configuration and its position $\mathbf{x}(\mathbf{X}, t) = \mathbf{X} + \mathbf{u}(\mathbf{X}, t)$ in the deformed configuration, where the displacement field $\mathbf{u}(\mathbf{X}, t)$ is a vector field representing the displacement at time t of the material point that was initially at position \mathbf{X} at time $t = 0$.

Displacement fields are commonly estimated by tracking markers in each image that identify material points. Because multiple markers are used to define a spatial field, establishing the correspondence between markers in deformed and reference configurations is a critical step. Some imaging techniques, such as phase-contrast MRI, provide direct measurements of displacement or velocity for each voxel, eliminating the problem of correspondence. Digital image correlation techniques may also be used to estimate displacement fields [182].

Displacement fields take into account deformation, rigid-body translation, and rigid-body rotation. Strain measures of interest isolate deformation and are based on the deformation gradient tensor field, $\mathbf{F}(\mathbf{X}, t)$, which maps an infinitesimal vector $d\mathbf{X}$ in the reference configuration to a corresponding vector $d\mathbf{x}(\mathbf{X}, t)$ in the deformed configuration:

$$d\mathbf{x}(\mathbf{X}, t) = \mathbf{F}(\mathbf{X}, t)d\mathbf{X} . \quad (1.1)$$

An example of an appropriate strain tensor is the Green–St. Venant strain tensor:

$$\mathbf{E}(\mathbf{X}, t) = \frac{1}{2} (\mathbf{F}^T(\mathbf{X}, t)\mathbf{F}(\mathbf{X}, t) - \mathbf{I}) . \quad (1.2)$$

where \mathbf{I} is the identity tensor. Whereas $\mathbf{F}(\mathbf{X}, t)$ includes the effects of rotation, $\mathbf{E}(\mathbf{X}, t)$ does not, so that $\mathbf{E}(\mathbf{X}, t)$ vanishes in a body that rotates but does not deform. Strain is a nondimensional measure of deformation. Normal strains can describe the change in the length of a line relative to its length in the reference configuration; for example, 0.05 strain corresponds roughly to a 5% change in length. In the limit of infinitesimal deformations, shear strains describe the change in angle between lines that are perpendicular in the reference configuration.

1.3.2 Spatial and temporal resolution, discretization, and noise

Converting from a series of pixelated images to a strain field involves tracking specific image features (markers) through the series and presents challenges associated with both spatial resolution and temporal resolution. Spatial resolution of displacement fields is determined by the spacing between tracked markers, which is typically larger than the pixel resolution. Because finite difference approximations are used to estimate the spatial derivatives in Equation 1.1, strain can be estimated accurately only if the distance between tracked points is much less than the characteristic wavelength or spatial feature of interest. Temporal sampling must be sufficiently fast to resolve displacements, and image acquisition must be sufficiently fast to avoid blurring. The timescales for impacts and pressure pulses associated with TBI pose challenges. As an alternative to studying short transient events directly, harmonic excitation can be used to characterize the behavior of the skull and brain, and the duality between frequency and time domain responses can be exploited [40]. For harmonic behavior, the sampling rate must exceed twice the frequency of the behavior itself [120], and to accurately capture transient response, the temporal sampling rate must be at least twice the highest frequency of interest. In practice, higher temporal sampling rates are always helpful to characterize continuous behavior.

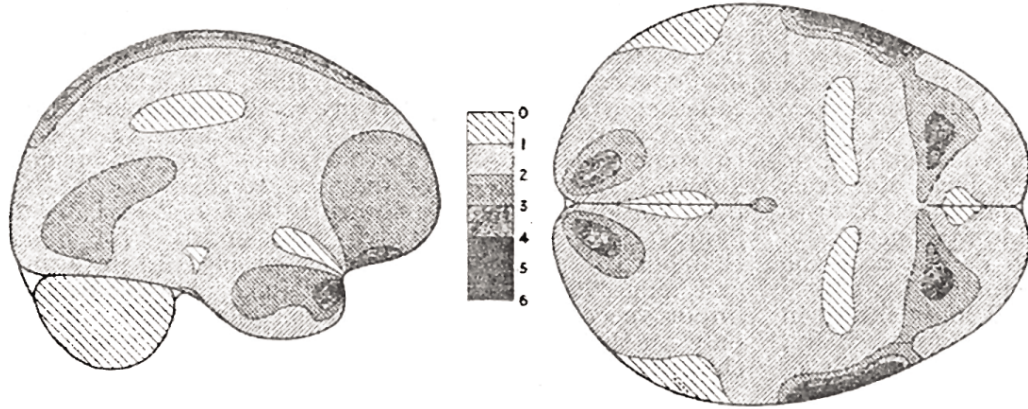


Figure 1.2: The earliest estimates of acceleration-induced shear strain fields within the human brain are those of Holbourn [63], who observed shear deformation patterns within gelatin-filled skulls due to occipital impact and angular acceleration/lateral impact. The scale bar represents the relative magnitude of shear in arbitrary units. Recent magnetic resonance imaging data have shown that shear strain patterns within a gelatin-filled skull differ fundamentally from those within a living human owing to several factors including brain architecture, vasculature, and attachment to the skull. Reproduced from Reference [63].

1.4 Imaging Studies in Physical Brain Surrogates, Animals, and Cadavers

1.4.1 Imaging studies of deformation in physical models

Much of our current insight into the mechanics of TBI comes from imaging of physical models: soft materials encased in rigid containers exposed to accelerations. In a classic study, Holbourn [63] filled models of a cross section of human skull with a gelatin mixture, sheared it by imposing large linear and angular accelerations of the skull, visualized strains with a polariscope, and depicted the strains using hand drawings (Figure 1.2). More recently, Margulies et al. [93] and Meaney et al. [102] filmed the motion of grid patterns in gel inside animal and human skulls during imposed angular acceleration (Figure 1.3). The amplitudes ($\approx 105 \text{ rad/s}^2$) and durations (15–20 ms) of angular acceleration used in these studies reached levels associated with diffuse axonal injury in pigs [102]. Large shear strains (0.10–0.30) were observed in these studies. Gel models, however, lack anatomic details such as vasculature, heterogeneous tissue

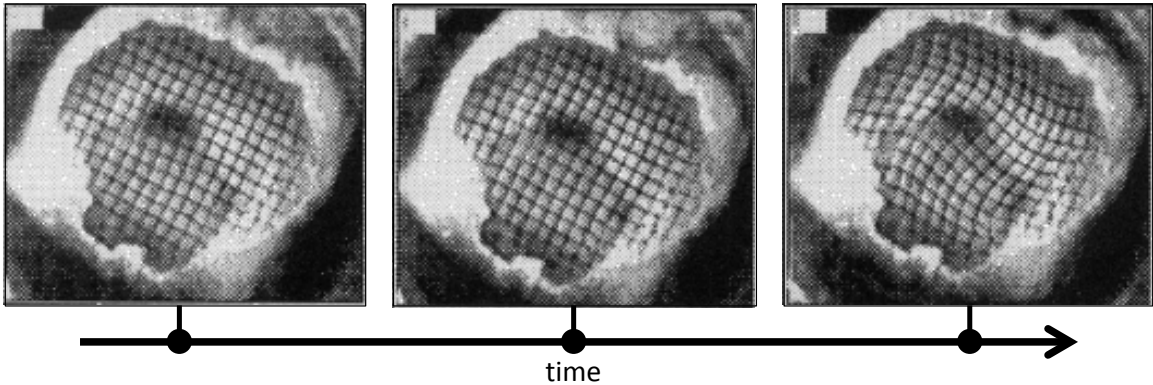


Figure 1.3: High-speed and high-resolution videography techniques have enabled studies of physical models of the brain that undergo large deformations at high strain rates. The skull of a miniature pig was filled with two layers of silicone gel; a grid pattern was painted between the layers. The assembly was subjected to angular accelerations of 50,000–200,000 rad/s^2 while grid deformation was recorded at 1,000 frames per second. Adapted from Reference [102].

structure, and CSF. This lack likely oversimplifies the response characteristics of the human brain, whose anatomic detail may, in fact, dramatically affect its response to impact or blast loading.

1.4.2 Visualization of brain deformation in animal studies

Imaging studies have long been performed in the brains of live animals, as well as *post mortem* in fresh animal brain specimens. Pudenz & Shelden [130] replaced the top half of the skull of a macaque monkey with transparent plastic and filmed the top of the brain during blunt impact at 2,000–3,000 frames per second. Results, presented as hand-drawn sketches in their 1946 paper, confirmed that impact leads to relative motion of the brain within the skull and that the brain rotates and deforms after impact. Nonetheless, internal brain deformations could not be visualized, and deformations were not quantified.

Two recent high-speed optical imaging studies of deformation of the pig brain, *post mortem*, illustrate the potential and challenges associated with these methods. Ibrahim et al. [65] studied the response of the piglet brain *in situ* (*post mortem*, but within

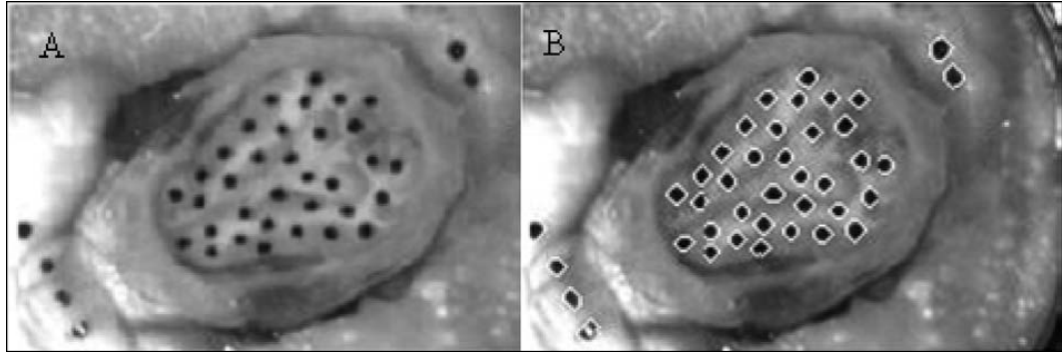


Figure 1.4: Progress on understanding acceleration-induced strain in the animal brain in situ has been made through high-speed video studies. The exposed flat surface of the hemisected brain of a juvenile pig was marked with India ink (a), and the skull and brain were covered by a layer of lubricant and by a transparent Plexiglas cover plate. Strain fields were estimated from marker positions (b) during an angular acceleration pulse with a peak magnitude of $\approx 10,000 \text{ m/s}^2$. Reproduced from Reference [65].

the skull) to high angular acceleration (Figure 1.4). The head of the piglet was transected so that an interior plane of the brain was exposed. This surface was marked, and the entire transected head was held securely in a container with a transparent cover. The assembly was subjected to angular accelerations believed to be adequate to cause injury, and high-speed (2,500 frames per second) images were acquired. Peak shear strains estimated from the displacements of surface marks (strain estimation methods are discussed below) typically exceeded 0.2. Lauret et al. [84] accelerated to $\approx 2,000 \text{ m/s}^2$ sagittal slices of pig brain, 4 mm thick, contained within a flat, stiff container with a skull-shaped cross section and a transparent cover. Images acquired at 1,600 frames per second were analyzed using digital image correlation to compute the displacement field of a random speckle pattern painted on the exposed brain surface. Peak strains of 0.10 to 0.20 were observed. The strength of these two studies is the ability to image at strains and strain rates similar to those observed in TBI. The shared drawback is the restriction to image strains on the surface of a portion of the brain *ex vivo*, with dramatically altered boundary conditions.

Studies in the intact living animal brain have been performed on small animals using MRI methods. Using MR tagging, Bayly et al. [16] measured strain fields in response to closed-skull indentation in a juvenile rat. The combined response of the deformable skull and of the heterogeneous, compliant, partitioned brain determined the strain field; this theme is consistent with the idea of the brain as a structure as well as

a material and consistent with observations taken on humans as described below. Using MR elastography, Clayton et al. [29] measured intracranial strains induced by harmonic loading in brains of living mice.

The great advantage of imaging studies in animals is the ability to characterize large deformation behavior in the intact brain. The most important shortcoming is that the anatomy of the human brain and skull differs greatly from those of other animals. The studies detailed below suggest that brain geometry and the details of the interface between the brain and skull are among the most important factors in the brain's mechanical response to mild impact, and this could well be the case for severe impact and blast loading as well. Although qualitative observations on the general features of brain injury can be derived from brain indentation studies in rodents, relating these to acceleration-induced injury in humans is challenging. A key limitation is the scaling effect [94, 92]: The acceleration required to attain a specific level of strain in an animal model scales nonlinearly with brain mass and size. As a result, the acceleration levels needed to produce closed-head acceleration-induced TBI in the mouse are not feasible for MR studies.

1.4.3 Visualization of brain deformation in cadavers

Hardy et al. [57] used high-speed (250–1,000 frames per second) biplanar X-ray imaging to track the displacement of 11 neutral-density radio-opaque markers in the brains of cadavers during impacts. Although these displacement fields are informative, the limited spatial resolution of the markers made it impossible to determine local tissue strain [57]. In addition, the mechanical properties of the cadaver brain differ significantly from those of a live subject [91], notwithstanding the considerable efforts taken to maintain perfusion of the tissue [44]. Despite these challenges, Zou et al. [183] reanalyzed these data and obtained informative estimates of brain motion relative to the skull that likely provide a lower bound on actual displacements, and they described qualitative features of the displacement field consistent with those of earlier MR studies, including an important role for brain rigid-body rotation at lower accelerations.

1.5 Measurement of Human Brain Motion by Phase-contrast Imaging and Magnetic Resonance Elastography

Inherently noninvasive and benign, MRI is particularly well suited to study brain tissue. Its signal derives from the spin precession of hydrogen nuclei in a strong magnetic field. Spins, which align predominantly with the magnetic field, are “tipped” by radiofrequency (RF) pulses; the frequency and phase of the ensuing precession are associated with spatial location (“encoded”) by gradients in the magnetic field. In classic anatomical MRI, image contrast arises from tissue-specific differences in water content or rates of signal decay. Different tissues, such as white or gray matter, exhibit differences in the decay of longitudinal (T1) or transverse (T2) components of spin magnetization, enabling acquisition of detailed static T1-weighted or T2-weighted anatomical images. Whereas such images are the most common application of MRI, manipulation of spin amplitude and phase by magnetic gradients and RF pulses can be used to measure motion. These techniques have been applied and adapted to the study of brain biomechanics increasingly over the past decade. Here we review some of the techniques that have recently produced valuable data and summarize the insight into brain deformation mechanisms provided by these data.

Phase-contrast MRI methods measure the relative angular position (i.e., phase) of the net transverse magnetization vector for each isochromat (spin packet). Because for each isochromat the magnetization vector precession rate (frequency) depends on the local magnetic field strength, isochromats moving in the presence of a spatially varying magnetic field (gradient) have a different phase than those that remain motionless in the same magnetic field. Muthupillai et al. [112] harnessed this concept to develop magnetic resonance elastography (MRE). They imaged steady-state, harmonic shear wave propagation in biological materials by synchronizing an applied mechanical vibration with an oscillatory magnetic field gradient, and they estimated the material’s shear modulus from the shear wave velocity. MRE was developed originally to calculate elastic properties of tissue and to detect diseased or degenerating tissue through differences in propagation speed associated with differences in stiffness [111, 113]. Poncelet et al. [127] demonstrated the use of phase-contrast MRI to measure motion

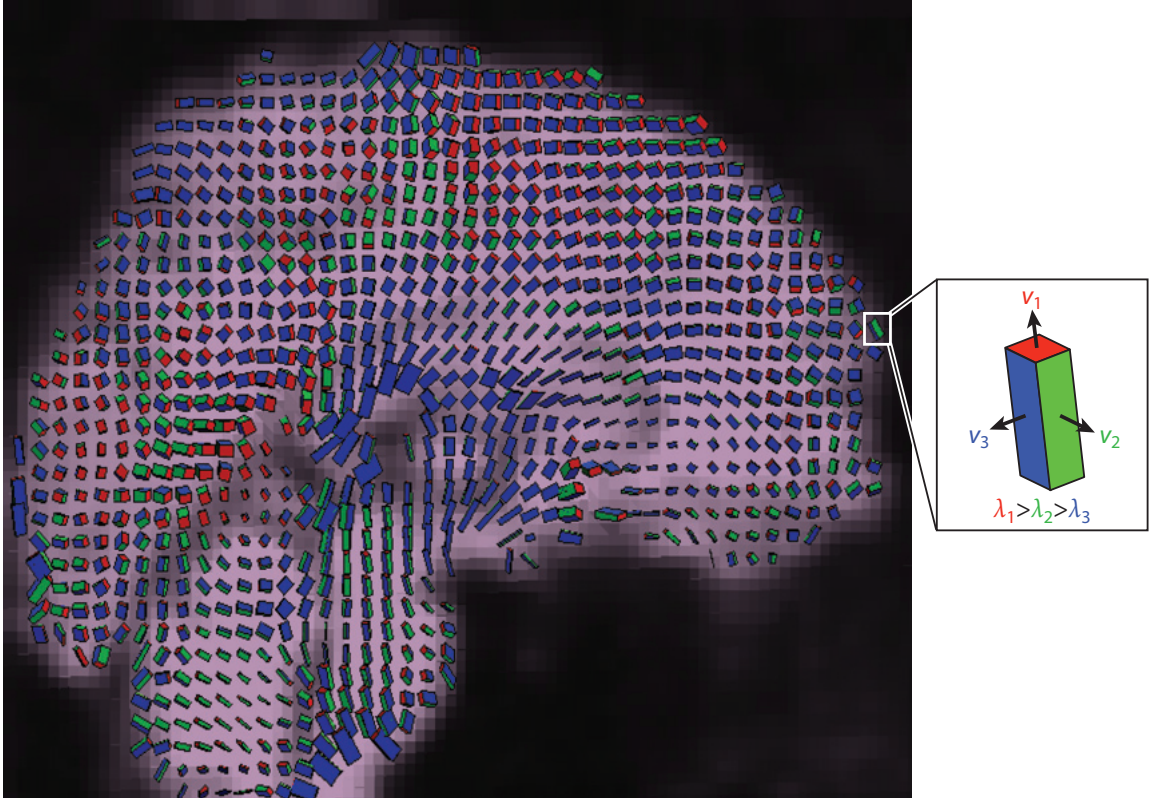


Figure 1.5: Phase-contrast MRI allows high spatial resolution imaging of the three-dimensional displacement and strain fields in the moving brains of live human subjects. Shown here is the strain-rate tensor field in the human brain due to normal pulsatile motion of the brain parenchyma. Box icons are color coded and scaled to represent the eigenvalues λ_i and scaled eigenvectors v_i of the strain-rate tensor at each voxel. Adapted from Reference [132].

in the brain parenchyma of human subjects during physiological pulsatile motion and voluntary head shaking. Reese et al. [132] used phase-contrast MRI to estimate 3D strain fields in the human brain due to pulsatile motion (Figure 1.5).

Described here are the initial implementations of MRE that targeted linear-elastic, homogeneous, isotropic materials, along with recent advances that enabled its application to brain tissue, which is viscoelastic, heterogeneous, anisotropic, and nonlinear. Our focus is data and methods for incrementally linear, homogeneous tissue that exhibits viscoelasticity, the latter property is especially important in brain tissue, which, like most biological materials, appears stiffer at higher rates of deformation.

1.5.1 Principles of magnetic resonance elastography

MRE measures oscillating shear displacements caused by harmonic vibration. Measurements of harmonic displacement are obtained by modulating the gradient field of the MR scanner at the vibration frequency [112]. Application of this sequence leads to images in which phase contrast is developed between vibrating spins.

If oscillating gradients of constant amplitude, frequency, and duration are applied in three orthogonal directions, a vector of motion-induced phase, ϕ , is obtained at each voxel in the image space. The oscillatory displacement, \mathbf{u} , of the voxel is proportional to the phase, ϕ , of the tissue spins obtained from elastography images. We define the position of a spin packet in a 3D sample as $\mathbf{x}(\mathbf{X}, t) = \mathbf{X} + \mathbf{u}(\mathbf{X}, t)$, where $\mathbf{u}(\mathbf{X}, t) = \mathbf{u}_0 \cos(\omega t - \mathbf{k} \cdot \mathbf{X} + \theta)$, in which \mathbf{u}_0 describes the vibration amplitude and direction and, \mathbf{X} , ω , \mathbf{k} , and θ are the initial position of the spin packet, vibration frequency, spatial frequency vector, and vibration phase, respectively. Then the component of the MR phase in the direction of the gradient is [113]

$$\phi_G(\mathbf{X}, \theta) = \gamma \int_0^{2\pi N/\omega} \mathbf{G}(t) \cdot \mathbf{x}(\mathbf{X}, t) dt = \frac{\gamma\pi N}{\omega} (\mathbf{G}_0 \cdot \mathbf{u}_0) \cos(\theta - \mathbf{k} \cdot \mathbf{X}), \quad (1.3)$$

where $\phi_G(\mathbf{X}, \theta)$ is the component of the MR phase vector in the direction of $\mathbf{G}(t)$, γ is the gyromagnetic ratio, N is the number of cycles, and $\mathbf{G}(t) = \mathbf{G}_0 \cos(\omega t)$ is the magnetic-field gradient. Thus, tracking phase in three orthogonal directions allows the three components of the displacement field to be obtained.

1.5.2 Estimation of elastic properties from magnetic resonance elastography data

Data from MRE studies consist of displacement fields. In order to obtain estimates of material parameters, these displacement fields must be interpreted in the context of elastodynamics. One approach is to fit the data directly to the differential equations governing elastic wave propagation. Alternative approaches include the application of the principle of virtual work, or the use of general signal processing techniques to estimate the local wavelength of the image data.

Fitting of elastic wave equations

The equation governing 3D wave propagation in a linear, homogenous, isotropic, unbounded medium is described by

$$\rho \frac{\partial^2 \mathbf{u}(\mathbf{X}, t)}{\partial t^2} = \mu \nabla^2 \mathbf{u}(\mathbf{X}, t) + (\lambda + \mu) \nabla (\nabla \cdot \mathbf{u}(\mathbf{X}, t)), \quad (1.4)$$

where ρ is the material density, λ and μ are the Lamé constants, and derivatives are relative to the reference configuration [80]. The dilatation ($\mathbf{u}_d(\mathbf{X}, t)$) and shear ($\mathbf{u}_s(\mathbf{X}, t)$) components of $\mathbf{u}(\mathbf{X}, t)$, where $\mathbf{u}(\mathbf{X}, t) = \mathbf{u}_d(\mathbf{X}, t) + \mathbf{u}_s(\mathbf{X}, t)$, satisfy Equation (4) independently and may be calculated from Equation (4) using the divergence and curl of $\mathbf{u}(\mathbf{X}, t)$, noting that $\nabla \cdot \mathbf{u}_s(\mathbf{X}, t) = 0$ and $\nabla \times \mathbf{u}_d(\mathbf{X}, t) = 0$. Dilatational waves (also known as pressure, compression, longitudinal, or irrotational waves) travel at a speed of $c_L = \sqrt{\frac{\lambda + 2\mu}{\rho}}$, and shear waves (also known as distortional, transverse, or equivoluminal waves) travel at a speed of $c_S = \sqrt{\frac{\mu}{\rho}}$. In general, the two modes are coupled through boundary conditions on $\mathbf{u}(\mathbf{X}, t)$ and on the stress field, which is related to through strain-displacement and constitutive relations [176]. For a displacement field due solely to shear deformation, Equation 1.4 reduces to

$$\rho \frac{\partial^2 \mathbf{u}_s(\mathbf{X}, t)}{\partial t^2} = \mu \nabla^2 \mathbf{u}_s(\mathbf{X}, t) \quad (1.5)$$

and can be solved to identify the elastic shear modulus, μ .

In general, within geometrically complex inhomogeneous media, dilatational and shear components of a wave field are coupled. The dilatational component of the displacement field (second term in Equation 1.4) may distort material parameter estimates if pure shear deformation is assumed and Equation 1.5 is used [152]. Taking the curl of the measured displacement field eliminates the dilatational component [152, 49]; the resulting data can be fitted to the equations above, after the curl operator has been applied. However, spatial derivatives involved in the curl operation amplify the effects of noise. Spatial filtering can remove long-wavelength components, but at the risk of mischaracterizing regions of unexpectedly high stiffness [152, 90]; the appropriate band limits of the spatial filter are seldom clear a priori. Clayton et al. [29] showed that estimates of mouse brain material properties differed slightly in measurements made between 600 and 1,800 Hz, depending on whether curl or spatial filtering was used to remove dilatational components.

When an imperfect theoretical model is used to interpret data from a physical system, evaluation of the goodness of fit, or applicability of the model to the data, is essential. Atay et al. [6] introduced the normalized residual error (the variance in the data that is not explained by the model) as a measure to evaluate confidence in local estimates of stiffness.

Local wavelength estimation

Elastic moduli may be estimated without explicitly fitting the equations of motion. A technique named local frequency estimation (LFE) [76] has been used to find the local wavelength λ of propagating mechanical waves from spatiotemporal images of the wave field. If one assumes only shear waves are imaged, the propagation speed is found simply from $c_S = \lambda f$, where $f = \omega/2\pi$ is the actuation frequency (Hz). The shear wave velocity relationship ($c_s = \sqrt{\mu/\rho}$) can then be used to infer material stiffness:

$$\mu = \rho c_S^2 = \rho \lambda^2 f^2. \quad (1.6)$$

Several investigators [90, 81] have used this approach to estimate the elastic shear modulus of tissues. The advantage of this approach is that the need for two or three numerical derivatives is circumvented, but, without a way to formally decouple shear and dilatational displacement components, estimates suffer from corruption by

dilatational waves. Our group has applied LFE to local rotation fields estimated from the curl of displacement fields measured during wave propagation in the human brain *in vivo* [30]. The use of local rotation in LFE is motivated by physics (it allows the decoupling of distortional and dilatational components of the wave field) and relative insensitivity to noise, as it requires only one spatial derivative.

Other methods

Other approaches to inverting MRE data involve energy principles. Romano et al. [138] employed a variational technique to invert a weak form of the equations of motion. Closely related is the work of Pierron and coworkers [47, 48], who used the virtual fields method to estimate material parameters from full-field displacement or strain data. Van Houten et al. [173] developed an inverse FE method to estimate material parameters in subzones of the image volume. Manduca et al. [90] describe LFE, algebraic direct inversion, and phase gradient approaches.

1.5.3 Estimation of viscoelastic properties from magnetic resonance elastography data

The viscoelastic correspondence principle allows the purely linear-elastic equations of motion to be generalized to analogous viscoelastic equations via Laplace or Fourier transform [131, 145, 86], allowing elastic moduli to be replaced with corresponding complex viscoelastic moduli without requiring a specific rheological model. The linear modulus μ in Equation 2.5 is replaced in Laplace or Fourier space by the transformed linear-viscoelastic complex shear modulus, $G^*(i\omega) = G'(\omega) + iG''(\omega)$, where $G'(\omega)$ and $G''(\omega)$ are the frequency-dependent storage and loss modulus, respectively, and viscoelastic estimates can be made.

Alternatively, in cases in which the wave field is well characterized by 1D propagation of plane waves or those in which it can be directionally decomposed into the superposition of several plane wave fields, logarithmic decrement methods can be used to extract the attenuation parameter α [80, 7]. The solution of plane distortional wave propagation in an isotropic viscoelastic medium relates storage $G'(\omega)$ and loss $G''(\omega)$

components of the complex shear modulus to the spatial attenuation constant α and wavenumber k , equivalent to $k = 2\pi/\lambda$, as follows [80, 7]:

$$\begin{bmatrix} k^2 - \alpha^2 & 2\alpha k \\ -2\alpha k & k^2 - \alpha^2 \end{bmatrix} \begin{Bmatrix} G' \\ G'' \end{Bmatrix} = \begin{Bmatrix} \rho\omega^2 \\ 0 \end{Bmatrix}. \quad (1.7)$$

1.5.4 Anisotropic material models

White matter, composed largely of aligned axonal fibers and associated myelin sheaths, is expected to be mechanically anisotropic [3]. In an anisotropic material, the speed of propagation varies with direction [80, 7], motivating approaches to quantify some aspects of material anisotropy using MRE [151]. However, to our knowledge, this has not been applied to brain tissue.

1.5.5 Magnetic resonance elastography imaging studies

MRE principles and techniques have now been used to estimate mechanical properties in a range of tissues and organs. MRE has also been applied to surrogate biomaterials, both for validating the technique and for characterizing the mechanical response of these materials.

Magnetic resonance validation studies

MRE is attractive because it is noninvasive, but is challenging to apply because it is inherently indirect: Mechanical properties are inferred from displacement fields arising from vibratory motion. Broad variation in reported MRE estimates of tissue mechanical properties has led to several efforts to evaluate the accuracy of MRE estimates through comparison with mechanical properties measured by direct mechanical tests [112, 6, 126, 54, 36, 134, 23, 125, 119]. The following conclusions were reached:

- Direct mechanical tests of biological tissue are difficult to perform, and results can vary significantly with variations in test procedure and experimental conditions [64]. Brain tissue is particularly compliant, fragile, and slippery, and

its properties vary with temperature, hydration, blood pressure, and time post-mortem.

- Brain tissue is viscoelastic. To be relevant, tissue phantoms used in studies to evaluate MRE should mimic the viscoelastic response of living tissue.
- Because viscoelastic material parameters are usually frequency dependent, direct mechanical tests performed for comparison with MRE should be performed at the same driving frequency.

Validation studies have been performed in animal brain tissue by comparing estimates from MRE *in vivo* with direct mechanical measurements *ex vivo*. Investigators have used MRE to quantify the components of the viscoelastic shear modulus of porcine brain tissue [174] and bovine liver tissue [71] and directly compared results with those yielded by oscillatory rheometry. Both studies showed qualitative agreement of trends in the values of $G'(\omega)$ and $G''(\omega)$ with frequency, but rheological tests of porcine brain tissue were performed at a much lower frequency (0.1 to 10 Hz) than that offered by MRE (80–140 Hz), making interpretation of results inconclusive.

However, more conclusive validation is available for gels. Okamoto et al. [119] developed a dynamic shear test to measure the complex shear modulus of a tissue-mimicking gel material at frequencies ranging from 20 Hz to 200 Hz. This allowed for direct comparison with MRE at the same frequencies. A close agreement between MRE results and dynamic shear test results at overlapping frequencies supports MRE applicability over a wide frequency range.

Magnetic resonance elastography studies of brain material properties

Numerous recent MRE studies of the brain in human subjects have been performed [49, 97, 72, 56, 141, 142, 180, 30], with high-resolution displacement fields resulting (Figure 1.6). Methods of Sinkus, Bilston, and collaborators [49, 180] are typical, involving harmonic motion to the skull through a vibrating bite bar. MRE data lie well within the range of data obtained by shear and indentation tests *ex vivo* (Figure 1.7) but are nevertheless somewhat variable. For example, McCracken and coworkers [97], who used 80-Hz excitation and fit a pure elastic model to their data, found shear

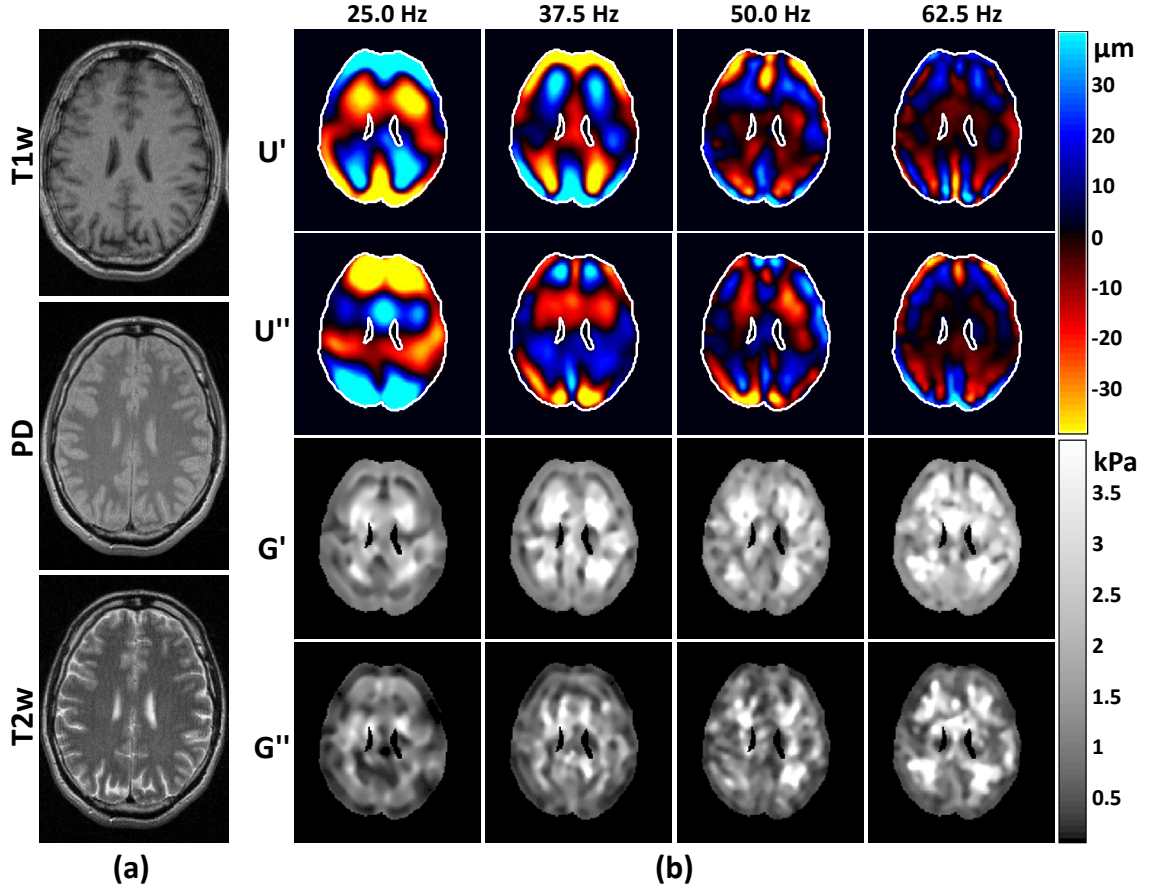


Figure 1.6: Magnetic resonance elastography (MRE) produces estimates of intracranial displacement fields observed in response to dynamic pressure loading of the skull. These can be inverted to estimate spatially varying mechanical properties of brain tissue. Example displacement fields shown here are obtained from a single-slice multifrequency MRE experiment. (a) Standard MR anatomical images: T1-weighted (T1w), proton density (PD), and T2-weighted (T2w) contrast. (b) Wave images and parameter fields. U' and U'' denote the real and imaginary parts of the first harmonic component $U(x, y, \omega)$ of the displacement field. The complex modulus images (G' and G'') denote the real and imaginary parts of the complex shear modulus $G^*(x, y, \omega)$. The driving frequencies are given above the columns. Reproduced from Reference [142].

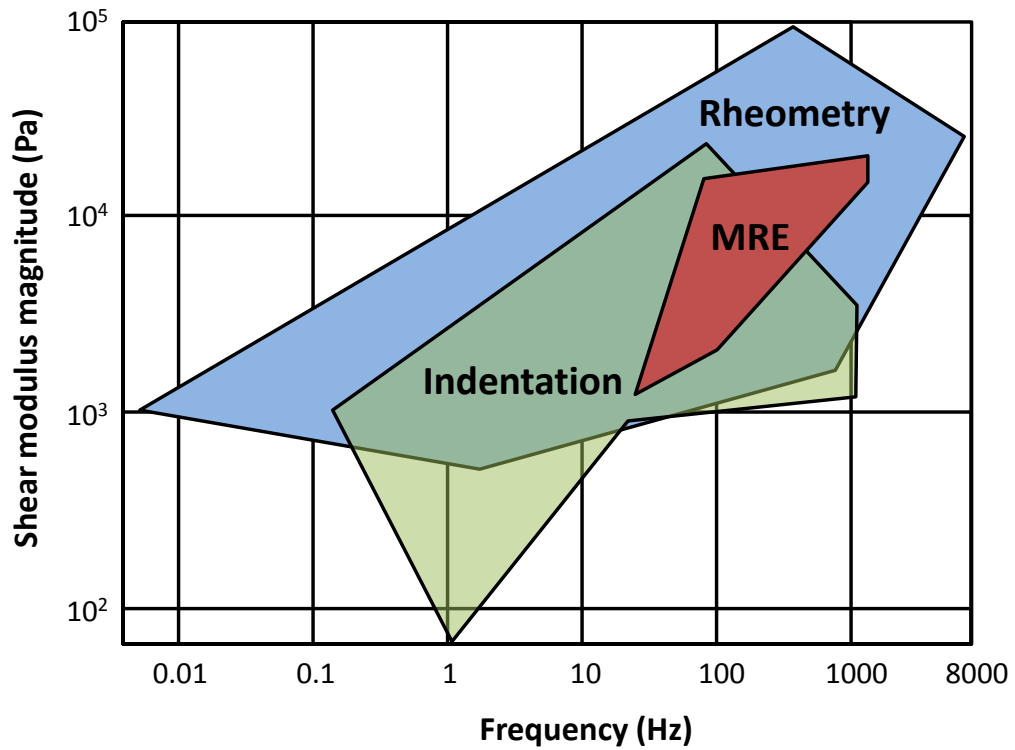


Figure 1.7: Magnetic resonance elastography (MRE) provides noninvasive estimates of living brain tissue in human volunteers. MRE-based estimates of brain tissue shear modulus vary among different studies but lie within the range of estimates obtained *in vitro* by direct mechanical tests. Adapted from Reference [24].

moduli of 5.3 ± 1.3 kPa for cortical gray matter and 10.7 ± 1.4 kPa for white matter. Kruse et al. [81], who applied LFE to displacement wave fields to estimate elastic parameters, found 5.2 ± 0.4 kPa for gray matter and 13.6 ± 1.3 kPa for white matter at 100-Hz driving frequency. Clayton and coworkers [30] recently used LFE on the isolated distortional component of the displacement field to calculate viscoelastic material parameters of gray and white matter at 45, 60, and 80 Hz and found that both gray and white matter storage moduli varied over this frequency range: 2.8–4.4 kPa (gray), and 3.7–4.7 kPa (white). Green et al. [49] used 90-Hz excitation and found cortical gray matter (3.1 ± 0.1 kPa) stiffer than white matter (2.7 ± 0.1 kPa). For reference, we note that Thibault & Margulies [166], using direct mechanical measurements (dynamic shear tests) of pig brain gray matter *ex vivo*, found $1.2+i0.8$ kPa at 50 Hz and $1.5+i1.3$ kPa at 100 Hz. Experimental approaches and parameter estimates from different MRE studies are summarized in Table 1.1.

1.6 Discussion and Conclusions

Imaging is an important component of the study of TBI mechanics, complementary and essential to efforts in modeling and simulation. It is likely that both simulation and imaging of biomechanics will play a major role in the effort to prevent TBI. Accurate computer models would also be valuable to those researching the neuropathology of TBI who wish to understand the direct effects of mechanical insult and separate these primary effects from delayed, or secondary, effects. However, without accurate mechanical parameters and careful validation by experimental studies such as those reviewed here, simulations will be neither reliable nor useful.

Important open questions remain, however. Perhaps the most important decision is which quantities to measure or calculate. Although strain and strain rate are known to be important metrics of tissue disruption, they may not be the only factors in injury severity. Imaging studies may help answer these questions. An example is the recent study of closed-head injury in the juvenile rat [14, 16], in which images of mechanical strain, obtained by MR tagging, are compared directly with histological images (Figure 14) to gain insight into neuropathological mechanisms [16]. This study shows not only that local measures of strain are important to the outcome in

Table 1.1: Magnetic resonance elastography (MRE)-based estimates of brain elastic or viscoelastic mechanical properties (healthy living human subjects).

Study	Frequency (Hz)	G' (kPa)			G'' (kPa)			Actuator
		Gray	White	Avg	Gray	White	Avg	
[142]	25	–	–	1.1 \pm 0.2	–	–	0.5 \pm 0.1	Head rocker
[142]	37.5	–	–	1.3 \pm 0.3	–	–	0.6 \pm 0.1	Head rocker
[30]	45	2.8 \pm 0.5	3.7 \pm 0.8	–	0.80 \pm 0.2	1.3 \pm 0.4	–	Acoustic pressure
[142]	50	–	–	1.5 \pm 0.2	–	–	0.6 \pm 0.1	Head rocker
[30]	60	3.1 \pm 0.3	3.3 \pm 0.1	–	1.7 \pm 0.3	2.0 \pm 0.1	–	Acoustic pressure
[142]	62.5	–	–	2.0 \pm 0.2	–	–	0.8 \pm 0.1	Head rocker
[97]	80	5.3 \pm 1.3	10.7	–	–	–	–	Bite bar
[30]	80	4.4 \pm 0.3	4.7 \pm 0.6	–	2.3 \pm 0.2	2.4 \pm 0.5	–	Acoustic pressure
[180]	80	2.3 \pm 0.2	2.4 \pm 0.2	–	1.1 \pm 0.0	1.2 \pm 0.2	–	Bite bar
[49]	90	3.1 \pm 0.1	2.7 \pm 0.1	–	2.5 \pm 0.2	2.5 \pm 0.2	–	Bite bar
[81]	100	5.2	13.6	–	–	–	–	Bite bar

an injury-level event but also that other (biological) factors play an important role. Strain fields correlate with, but do not replicate, patterns of neuronal apoptosis. The pattern of neuronal apoptosis was well explained, however, by the intersection of the strain field with the axonal tracts connecting these neurons to their synaptic partners.

The pervasive technical challenge that underlies all work on the biomechanics of TBI is predicting the response of the human brain to high loading without performing direct tests. Because it is impossible to study directly the mechanics of TBI in humans, different models (gel surrogates, animal, cadaver, and human) and imaging techniques are required to span the range of necessary data. For example, to understand the effects of the human anatomy, data must be acquired in humans at safe, physiologically relevant levels of strain and strain rate; yet data from animal models or *in vitro* studies are needed to understand the nonlinear properties of the brain during large deformation. Results from studies in gel surrogate phantoms can be compared with carefully controlled laboratory tests and closed-form solutions. The complete picture of brain biomechanics will be a mosaic of the results of such complementary studies.

1.7 Summary

Imaging studies have been pursued for decades to understand the motion of the brain that occurs in response to impact or acceleration of the skull. Recent advances have exploited high-speed video, digital image correlation, and MRI techniques developed specifically to visualize and characterize fast events. We believe that MRI-based techniques in particular provide a window into the complex structural interactions that modulate mechanical injury in the human brain.

Imaging studies will continue to help develop a comprehensive picture of the brain's behavior when the skull accelerates and to illuminate how the transduction of mechanical stresses to the brain relates to brain injury. Continued effort in these directions promises to have great impact on our scientific understanding of TBI and our ability to prevent and treat brain injury.

Summary Points

- Imaging of brain biomechanics is important for validation and calibration of biomechanical models and for testing of hypotheses about the mechanical response of the brain.
- At physiologically relevant acceleration magnitudes, the meninges, vessels, and sheathed cranial nerves arrest brain motion; wave motion is not observed; and higher strains associated with brain-skull attachment appear at sites associated with contrecoup injury.
- Strains on the order of 5% are common in the brain in response to daily activity.
- At high acceleration levels in cadavers, high-speed biplanar X-ray images suggest that the meninges are unable to resist inertial forces, and broad brain-skull contact may occur.
- High-speed video imaging allows measurement of large deformations at high strain rates in brain slices or brain sections *in situ* or *in vitro*.
- MRE provides both visualization of wave propagation patterns and noninvasive estimates of frequency-dependent brain biomechanical properties.

1.8 Specific Aims and Organization of this Work

This work aims to develop and use magnetic resonance elastography for the purposes of quantitatively measuring dynamic brain response to validate numerical models of the human head. Brain material properties, boundary conditions, and basic response characteristics to dynamic loading must be validated *in vivo*. Until numerical models of brain biomechanics are validated with appropriate *in vivo* data, they will remain controversial within the scientific community. Their predictions will be treated with skepticism and their utility limited.

1.8.1 Specific aims

Experimental techniques which provide direct measures of brain biomechanics *in vivo* and non-invasively are limited. MR elastography is a recently developed imaging technique and provides new means to acquire biomechanical information on the living, intact brain. This study investigates the utility of MRE for these purposes, and to do so three (3) specific aims are proposed:

- Aim 1: Develop and validate an isotropic viscoelastic inversion algorithm for MR elastography data.
- Aim 2: Develop capabilities to perform high-throughput longitudinal MR elastography screening at high actuation frequencies in the living mouse brain.
- Aim 3: Develop experimental capabilities to perform MR elastography in the living human brain and novel algorithms to extract biomechanical information from these data.

1.8.2 Organization of this work

The requisite mathematical preliminaries to perform this work are outlined in Chapter 2. This includes a brief development of continuum mechanics and magnetic resonance imaging theory.

Chapter 3 is an exposition of the elastography validation study. The viscoelastic properties of a tissue analog were characterized by bench-top mechanical test and used as a calibrated phantom for MRE experiments.

A displacement-based viscoelastic isotropic inversion algorithm was developed for MRE data and applied to the mouse brain in Chapter 4. Dispersion of brain tissue shear modulus was assessed at high actuation frequencies. Brain response to rapid loading is an important consideration in understanding and modeling traumatic brain injury.

The structural-functional dynamics of the intact living human head were assessed in Chapter 5. Shear motion in brain tissue is suspected to cause axonal damage, thus inducing brain injury; as such, the transmission, attenuation, and reflection of shear wave propagation in the human brain was investigated.

Chapter 6 introduces a preliminary study of a method to detect and quantify anisotropic mechanical properties of tissue. A unique feature of this work, structural properties of tissue, obtained via diffusion tensor imaging, are capable of being used to extract mechanical tissue properties from MRE elastography data.

Overarching conclusions, methodological limitations, and suggestions for future studies are discussed in Chapter 7.

Chapter 2

Theoretical Framework

2.1 Overview

In this chapter the equations of motion for steady-state harmonic wave propagation in extended media are developed within the limit of small displacement gradients. Equations of wave propagation in isotropic and transversely isotropic media are discussed because they are useful in approximating the response of biological tissues to harmonic excitation. Viscoelasticity is addressed in two ways: via the correspondence principle and by assumption of a rheological model *a priori*. The basic concepts underlying the use of magnetic resonance imaging to measure wave propagation fields (magnetic resonance elastography) and tissue structure (diffusion tensor imaging) are introduced. Details of parameter estimation vary based on application and are addressed in subsequent chapters.

Although biological tissue commonly undergoes large deformations, it is important to understand small-strain behavior in order to guide the selection of appropriate large-deformation models. In this work, imposed strain amplitudes are small ($\ll 1.0$) and much less than any threshold known to induce TBI. Questions regarding nonlinearity in both a kinematic and material sense are not addressed.

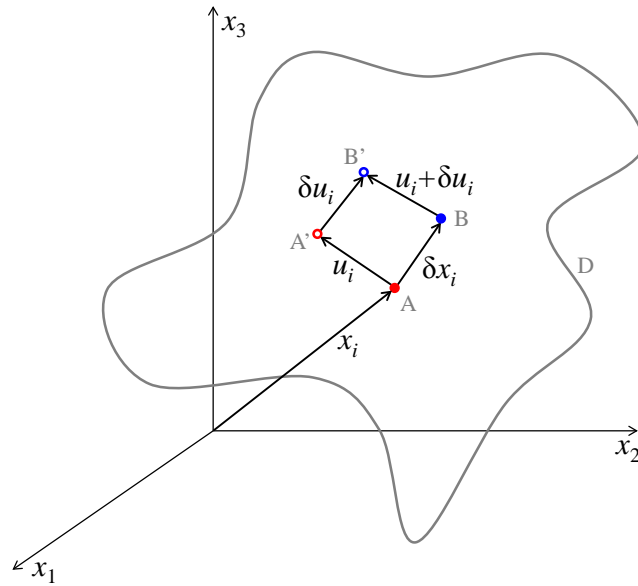


Figure 2.1: Deformation of two particles, A and B, in a deformable body D.

2.2 A Brief Review of Continuum Mechanics

2.2.1 Kinematics

The displacement of a particle at any point in a deformable body may be decomposed into coordinates parallel to an orthogonal reference system. A Cartesian system with reference axes x_1 , x_2 , and x_3 describing displacements u_1 , u_2 , and u_3 along those axes (Figure 2.1) is used here. Consider a particle within the body D at an undeformed position A: (x_1, x_2, x_3) with a corresponding deformed position A': $(x_1 + u_1, x_2 + u_2, x_3 + u_3)$. Material deformation is developed when particles within a body are displaced relative to each other. Now consider another point infinitesimally close to the reference position. Its undeformed position is B: $(x_1 + \delta x_1, x_2 + \delta x_2, x_3 + \delta x_3)$ with defined displacements $(u_1 + \delta u_1, u_2 + \delta u_2, u_3 + \delta u_3)$. The differential particle

displacement δu_i is then described by

$$\delta u_1 = \frac{\partial u_1}{\partial x_1} \delta x_1 + \frac{\partial u_1}{\partial x_2} \delta x_2 + \frac{\partial u_1}{\partial x_3} \delta x_3, \quad (2.1a)$$

$$\delta u_2 = \frac{\partial u_2}{\partial x_1} \delta x_1 + \frac{\partial u_2}{\partial x_2} \delta x_2 + \frac{\partial u_2}{\partial x_3} \delta x_3, \text{ and} \quad (2.1b)$$

$$\delta u_3 = \frac{\partial u_3}{\partial x_1} \delta x_1 + \frac{\partial u_3}{\partial x_2} \delta x_2 + \frac{\partial u_3}{\partial x_3} \delta x_3, \quad (2.1c)$$

or, in a more compact notation, as

$$\delta u_i = \frac{\partial u_i}{\partial x_j} \delta x_j. \quad (2.2)$$

$\partial u_i / \partial x_j$ is known as the displacement gradient matrix and is, by itself, a deficient measure of deformation because it does not distinguish rigid body motion from material deformation [7]. That is to say, a body undergoing rigid motion produces non-zero displacement gradients regardless of whether or not material deformation occurred.

A sufficient measure of deformation is strain:

$$\epsilon_{ij} = \frac{1}{2} \left(\frac{\partial u_i}{\partial x_j} + \frac{\partial u_j}{\partial x_i} \right). \quad (2.3)$$

This definition of strain ϵ_{ij} is known as linearized tensorial strain and is valid for small displacement gradients $\partial u_i / \partial x_j$. Tensorial strain differs from engineering strain by the leading factor of 1/2 on the shear strain terms (i.e., when $i \neq j$).

2.2.2 Equilibrium

Consider an infinitesimal rectangular parallelepiped with a general state of stress (Figure 2.2). The equations of equilibrium are obtained by considering an infinitesimal variation δ in stress across each face of the parallelepiped with respect to each coordinate axis and multiplying it by the face area. This geometric visualization tool used to invoke Newton's second law of motion. For example, the resultant force F_1

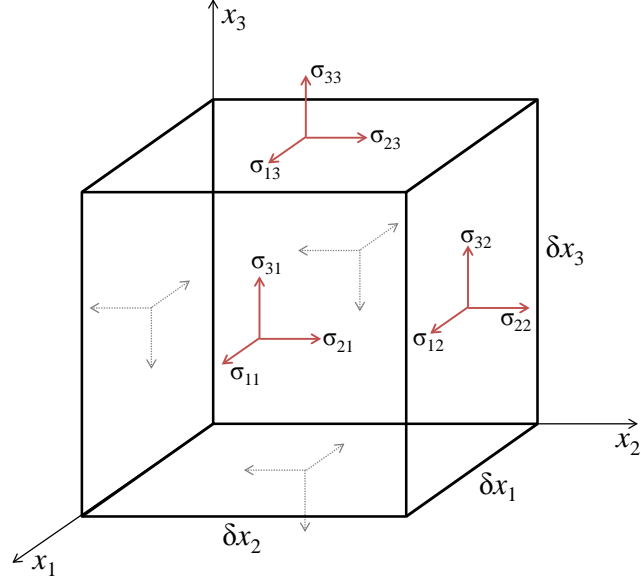


Figure 2.2: Stresses acting on an infinitesimal rectangular parallelepiped of volume $V = \delta x_1 \delta x_2 \delta x_3$.

acting in the x_1 -direction is

$$\begin{aligned}
 F_1 = & \left(\sigma_{11} + \frac{\partial \sigma_{11}}{\partial x_1} \delta x_1 \right) \delta x_2 \delta x_3 - \sigma_{11} \delta x_2 \delta x_3 + \\
 & \left(\sigma_{12} + \frac{\partial \sigma_{12}}{\partial x_2} \delta x_2 \right) \delta x_1 \delta x_3 - \sigma_{12} \delta x_1 \delta x_3 + \\
 & \left(\sigma_{13} + \frac{\partial \sigma_{13}}{\partial x_3} \delta x_3 \right) \delta x_1 \delta x_2 - \sigma_{13} \delta x_1 \delta x_2. \quad (2.4)
 \end{aligned}$$

Newton's second law states that forces acting along a particular line of action must balance the inertial load along that line of action. If body forces are neglected, then

$$F_1 = \rho (\delta x_1 \delta x_2 \delta x_3) \frac{\partial^2 u_1}{\partial t^2}, \quad (2.5)$$

where ρ is the material density and u_1 is the displacement component in the x_1 -direction.

Simplifying Equation 2.4 and using Equation 2.5, the x_1 -direction equation of motion is obtained. The process is repeated for the x_2 - and x_3 -directions to find all three

equations of motion with respect to a Cartesian reference frame:

$$\rho \frac{\partial^2 u_1}{\partial t^2} = \frac{\partial \sigma_{11}}{\partial x_1} + \frac{\partial \sigma_{12}}{\partial x_2} + \frac{\partial \sigma_{13}}{\partial x_3}, \quad (2.6a)$$

$$\rho \frac{\partial^2 u_2}{\partial t^2} = \frac{\partial \sigma_{21}}{\partial x_1} + \frac{\partial \sigma_{22}}{\partial x_2} + \frac{\partial \sigma_{23}}{\partial x_3}, \text{ and} \quad (2.6b)$$

$$\rho \frac{\partial^2 u_3}{\partial t^2} = \frac{\partial \sigma_{31}}{\partial x_1} + \frac{\partial \sigma_{32}}{\partial x_2} + \frac{\partial \sigma_{33}}{\partial x_3}. \quad (2.6c)$$

Equations 2.6 can be represented using the following compact notation:

$$\frac{\partial \sigma_{ij}}{\partial x_j} = \rho \frac{\partial^2 u_i}{\partial t^2}, \quad (2.7)$$

for $i, j = 1, 2, 3$.

2.2.3 Constitutive behavior

The intrinsic structure of a material dictates how it deforms under load. For an elastic medium, in the linear response regime, a generalized form of Hooke's law is applied: *The six components of stress at any point of an elastic solid body are connected with the six components of strain at the point* [87]. Hence,

$$\sigma_{ij} = C_{ijkl} \epsilon_{kl}, \quad (2.8)$$

for $i, j, k, l = 1, 2, 3$. C_{ijkl} is the rank four stiffness tensor and contains the elastic constants of the material. They are the coefficients of a homogeneous quadratic function W , known as the strain-energy function [87]. Symmetry of the stress σ_{ij} and strain ϵ_{ij} tensors requires the stiffness tensor to be symmetric ($C_{ijkl} = C_{jikl} = C_{ijlk} = C_{jilk}$, $C_{ijkl} = C_{klij}$) [80, 83, 18].

Voigt developed a convenient compact notation to facilitate visualization of the stress-strain relation:

$$ij \leftrightarrow m, n \equiv \begin{cases} 11 \leftrightarrow 1, & 22 \leftrightarrow 2, & 33 \leftrightarrow 3 \\ 23 \leftrightarrow 4, & 13 \leftrightarrow 5, & 12 \leftrightarrow 6 \end{cases}. \quad (2.9)$$

Hence, Equation 2.8 becomes

$$\begin{pmatrix} \sigma_1 \\ \sigma_2 \\ \sigma_3 \\ \sigma_4 \\ \sigma_5 \\ \sigma_6 \end{pmatrix} = \begin{bmatrix} c_{11} & c_{12} & c_{13} & c_{14} & c_{15} & c_{16} \\ & c_{22} & c_{23} & c_{24} & c_{25} & c_{26} \\ & & c_{33} & c_{34} & c_{35} & c_{36} \\ & \text{sym.} & & c_{44} & c_{45} & c_{46} \\ & & & & c_{55} & c_{56} \\ & & & & & c_{66} \end{bmatrix} \begin{pmatrix} \epsilon_1 \\ \epsilon_2 \\ \epsilon_3 \\ 2\epsilon_4 \\ 2\epsilon_5 \\ 2\epsilon_6 \end{pmatrix}. \quad (2.10)$$

The general strain-energy expression can now be expressed as:

$$W = \frac{1}{2} C_{mn} \epsilon_m \epsilon_n. \quad (2.11)$$

(In this abbreviated notation, note the factor of two on shearing strains to convert them from tensorial to engineering descriptions of strain.) Given a particular material, 21 constants in C_{ijkl} must be explicitly defined. If planes of material symmetry exist, the number of constants is reduced.

Isotropy

The simplest and by far most common material model used in engineering applications is isotropy. Under the conditions of isotropy, the material is said to have complete symmetry. No matter the set of rectangular axes chosen, only two independent constants remain. For such a material the strain-energy function has the form [156]

$$W = \frac{1}{2} \lambda \epsilon_{ii} \epsilon_{jj} + \mu \epsilon_{ij} \epsilon_{ij}. \quad (2.12)$$

Strain will produce an internal stress that depends only on two material constants,

$$C_{mn} = \begin{bmatrix} \lambda + 2\mu & \lambda & \lambda & & & \\ \lambda & \lambda + 2\mu & \lambda & & & \\ \lambda & \lambda & \lambda + 2\mu & & & \\ & & & \mu & & \\ & & & & \mu & \\ & & & & & \mu \end{bmatrix} \quad (2.13)$$

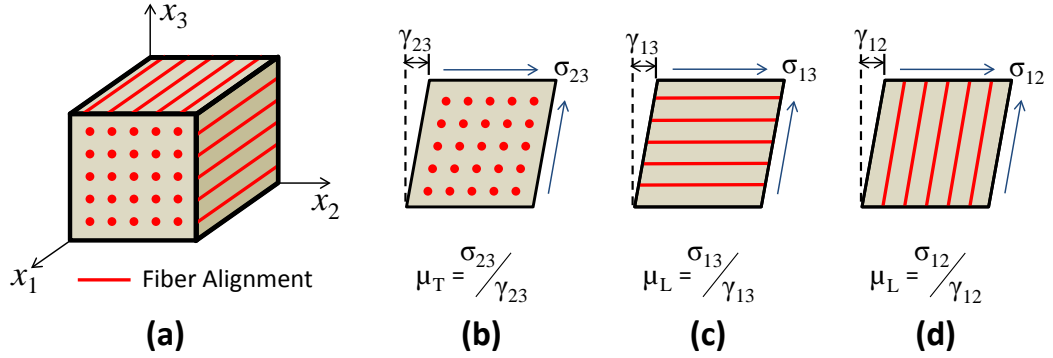


Figure 2.3: (a) Transversely isotropic material model with fibers aligned with the x_1 -axis. (b-d) Application of shear stress along a face produces a corresponding shear strain in proportion to the shear modulus. In transversely isotropic media there are two shear moduli: μ_T describes shear in a plane normal to the symmetry axis, and μ_L in planes parallel to the symmetry axis. Biological media often exhibit $\mu_L > \mu_T$. ($\gamma_{ij} = 2\epsilon_{ij}$, for $i \neq j$.)

where λ and μ are known as the Lamé constants [80]. In practice, μ is known simply as the shear modulus since it governs shear deformation in the stress-strain relation. Contrarily, λ is coupled in the stress-strain relation. Its effect is perhaps better understood in terms of the engineering constant governing uniaxial tension (i.e., Young's modulus) [80]:

$$E = \frac{\mu(3\lambda + 2\mu)}{(\lambda + \mu)}.$$

It is also helpful to define Poisson's ratio in these terms [144]

$$\nu = \frac{\lambda}{2(\lambda + \mu)}.$$

Transverse isotropy

In biological media, a material model imposing transverse isotropy (hexagonal anisotropy) is often employed since it approximates the fibrous composition of many types of tissue. In this case, the stiffness tensor can be described in terms of five independent constants. The strain-energy function has the form [156]

$$W = \frac{1}{2}\lambda\epsilon_{ii}\epsilon_{jj} + \mu_T\epsilon_{ij}\epsilon_{ij} + \alpha a_i\epsilon_{ij}a_j\epsilon_{kk} + 2(\mu_L - \mu_T)a_i\epsilon_{ij}\epsilon_{jk}a_k + \frac{1}{2}\beta a_i a_j \epsilon_{ij} a_k a_l \epsilon_{kl}, \quad (2.14)$$

where a_i is the vector defining the axis of symmetry. Following Spencer's notation [156], if fibers are assumed to be aligned along the x_1 -axis ($a_1 = 1, a_2 = a_3 = 0$), then the stiffness tensor will have the form

$$C_{mn} = \begin{bmatrix} \lambda + 2\alpha + 4\mu_L - 2\mu_T + \beta & \lambda + \alpha & \lambda + \alpha & & & \\ & \lambda + \alpha & \lambda + 2\mu_T & \lambda & & \\ & \lambda + \alpha & \lambda & \lambda + 2\mu_T & & \\ & & & & \mu_T & \\ & & & & & \mu_L \\ & & & & & & \mu_L \end{bmatrix}, \quad (2.15)$$

where μ_T and μ_L are the shear moduli describing shear acting on planes normal and parallel to the axis of symmetry (Figure 2.3). Similar to the isotropic material model, the constants λ , α , and β are difficult to interpret in terms of the stress-strain relationship. The following expressions provide relationships between all five constants and the engineering constants that govern uniaxial tension both parallel (E_L) and normal (E_T) to the fiber direction:

$$E_L = 4\mu_L - \mu_T + \beta - \frac{(\alpha - \mu_T)^2}{\lambda + \mu_T}, \text{ and} \\ E_T = 4\mu_T \frac{\beta\lambda + 2\alpha\mu_T + \beta\mu_T + 4\lambda\mu_L - \lambda\mu_T + 4\mu_L\mu_T - \alpha^2 - 2\mu_T^2}{\beta\lambda + 4\alpha\mu_T + 2\beta\mu_T + 4\lambda\mu_L + 8\mu_L\mu_T - \alpha^2 - 4\mu_T^2}. \quad (2.16)$$

It also helpful to define the three Poisson ratios in these terms:

$$\nu_T = \frac{-\alpha^2 + \beta\lambda + 4\lambda\mu_L - \lambda\mu_T}{\beta\lambda + 4\alpha\mu_T + 2\beta\mu_T + 4\lambda\mu_L + 8\mu_L\mu_T - \alpha^2 - 4\mu_T^2}, \\ \nu_{TL} = \frac{\mu_T(\alpha + \lambda)(\lambda + \mu_T)}{(\lambda + \mu_T)(\beta\lambda + 4\alpha\mu_T + 2\beta\mu_T + 4\lambda\mu_L + 8\mu_L\mu_T - \alpha^2 - 4\mu_T^2)}, \text{ and} \\ \nu_{LT} = \frac{\lambda + \alpha}{2(\lambda + \mu_T)}.$$

The Poisson ratios ν_{TL} and ν_{LT} are not equal, but must satisfy $\nu_{LT}/E_L = \nu_{TL}/E_T$ for symmetry of the stress-strain relation [20]. If $\alpha = \beta = 0$ and $\mu_T = \mu_L = \mu$, each expression above reduces to the isotropic Young's modulus E and Poisson's ratio ν .

2.3 Wave Propagation in Unbounded Homogeneous Linear Elastic Media

2.3.1 Isotropic media

By combining Equations 2.3, 2.7, and 2.8 with an isotropic constitutive relation (Equation 2.13), the equations of dynamic equilibrium for an unbounded, isotropic, homogeneous, linear, elastic solid are derived:

$$\rho \frac{\partial^2 u_i}{\partial t^2} = \mu u_{i,jj} + (\lambda + \mu) u_{j,ij}. \quad (2.17)$$

Plane waves propagating in a direction specified by direction cosines (n_1, n_2, n_3) are described by

$$(u_1, u_2, u_3) = A(p_1, p_2, p_3) e^{i(n_1 \cdot x_1 + n_2 \cdot x_2 + n_3 \cdot x_3 - ct)}, \quad (2.18)$$

or, more compactly, as

$$u_i = A p_i \exp[i(n_i \cdot x_i - ct)], \quad (2.19)$$

where n_i is the wave propagation direction unit vector, and p_i is the unit vector defining the direction of particle motion (often referred to as the “polarization direction”). The wavenumber k and wave frequency ω are related to the phase velocity $c = \omega/k$. By combining Equations 2.17 and 2.19, the Christoffel equation is obtained:

$$C_{ijkl} n_j n_l p_k = \rho c^2 p_i. \quad (2.20)$$

The Christoffel equation compactly expresses three-dimensional plane wave propagation in terms of propagation and polarization directions [80, 156, 22, 7]. Equation 2.20 can be further simplified to

$$Q_{ik}(n_j) p_k = \rho c^2 p_i \quad (2.21)$$

by introduction of the Christoffel (acoustic) tensor

$$Q_{ik} = C_{ijkl} n_j n_l. \quad (2.22)$$

Equation 2.21 states that the polarization direction p_i is an eigenvector of the Christoffel tensor $Q_{ik}(n_j)$ with an eigenvalue corresponding to ρc^2 . The Christoffel tensor is

always symmetric and positive definite because the elastic stiffness tensor C_{ijkl} is symmetric and positive definite. It is also a second rank tensor, so its characteristic equation describes three propagation speeds along three propagation directions. In general, depending on the orientation of material symmetries with respect to the wave propagation vector, propagation speeds may be degenerate in that some are duplicated and not all are detectable.

In isotropic media the Christoffel tensor takes the following form:

$$Q_{ik} = \begin{bmatrix} (\lambda + 2\mu)n_1^2 + \mu n_2^2 + \mu n_3^2 & (\lambda + \mu)n_1 n_2 & (\lambda + \mu)n_1 n_3 \\ (\lambda + \mu)n_1 n_2 & \mu n_1^2 + (\lambda + 2\mu)n_2^2 + \mu n_3^2 & (\lambda + \mu)n_2 n_3 \\ (\lambda + \mu)n_1 n_3 & (\lambda + \mu)n_2 n_3 & \mu n_1^2 + \mu n_2^2 + (\lambda + 2\mu)n_3^2 \end{bmatrix}. \quad (2.23)$$

Wave solutions in isotropic media are the same for any direction of propagation. The Christoffel tensor can be reduced by propagating waves along one of the axes of the material reference coordinate system.

For example, the Christoffel equation (2.20) for transmission along the direction $n_1 = 1$, $n_2 = n_3 = 0$ in isotropic media becomes

$$\begin{bmatrix} (\lambda + 2\mu) & 0 & 0 \\ 0 & \mu & \\ 0 & 0 & \mu \end{bmatrix} \begin{Bmatrix} p_1 \\ p_2 \\ p_3 \end{Bmatrix} = \rho c^2 \begin{Bmatrix} p_1 \\ p_2 \\ p_3 \end{Bmatrix}, \quad (2.24)$$

and provides three wave velocities corresponding to three wave polarizations. There are two shear waves, SH: $p = (0, 1, 0)$ and SV: $p = (0, 0, 1)$, both with velocity $c = \sqrt{\mu/\rho}$, and one pressure wave P: $p = (1, 0, 0)$ with velocity $c = \sqrt{(\lambda + 2\mu)/\rho}$.

A key concept lies in this example. Isotropic media are universally symmetric; therefore the material reference coordinate system can always be aligned with the direction of wave propagation to produce a diagonalized Christoffel tensor like that presented in Equation 2.24. In general, this is not true for wave propagation in anisotropic media (Figure 2.4).

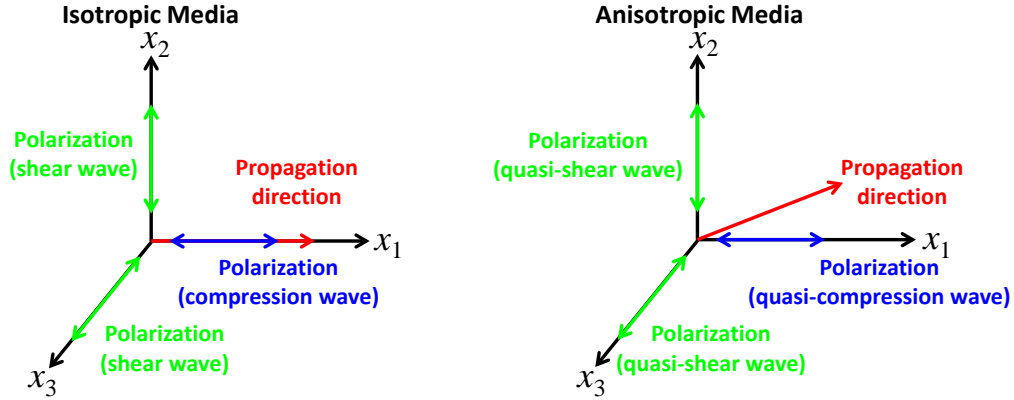


Figure 2.4: As a consequence of complete material symmetry, wave propagation in isotropic media will always produce three distinct waves, each corresponding to the direction of wave polarization. In general, this is not true for waves in anisotropic media. Wave degeneracy and quasi waves may present.

2.3.2 Transversely isotropic media

The equations of dynamic equilibrium for an unbounded, transversely isotropic, homogeneous, linear, elastic solid are derived in the same fashion as the isotropic case, with one distinction; a transversely isotropic constitutive relation (Equation 2.15) is utilized. An explicit compact form of equilibrium in terms of material constants, like that presented for the isotropic case Equation 2.17, is not readily available. The reader is referred to others [2] for these expressions.

In transversely isotropic media, when the axis of material symmetry is along x_1 , the Christoffel tensor takes the following form:

$$Q_{ik} = \begin{bmatrix} (\lambda + 2\alpha + 4\mu_L - 2\mu_T + \beta)n_1^2 + \mu_L n_2^2 + \mu_L n_3^2 & (\alpha + \lambda + \mu_L)n_1 n_2 & (\alpha + \lambda + \mu_L)n_1 n_3 \\ (\alpha + \lambda + \mu_L)n_1 n_2 & \mu_L n_1^2 + (\lambda + 2\mu_T)n_2^2 + \mu_T n_3^2 & (\lambda + \mu_T)n_2 n_3 \\ (\alpha + \lambda + \mu_L)n_1 n_3 & (\lambda + \mu_T)n_2 n_3 & \mu_L n_1^2 + \mu_T n_2^2 + (\lambda + 2\mu_T)n_3^2 \end{bmatrix}. \quad (2.25)$$

Consider now only waves traveling in a plane such that $n_1 = \cos \theta$, $n_2 = \sin \theta$, and $n_3 = 0$, where θ is the angle between the symmetry axis and the propagation direction.

The Christoffel tensor expressed as Equation 2.25 is recast into

$$Q_{ik} = \begin{bmatrix} (\lambda + 2\alpha + 4\mu_L - 2\mu_T + \beta)c^2 + \mu_L s^2 & (\lambda + \alpha + \mu_L)sc & 0 \\ (\lambda + \alpha + \mu_L)sc & \mu_L c^2 + (\lambda + 2\mu_T)s^2 & 0 \\ 0 & 0 & \mu_L c^2 + \mu_T s^2 \end{bmatrix}, \quad (2.26)$$

with $s = \sin \theta$ and $c = \cos \theta$.

At the limit of incompressibility, only shear waves exist. Ergo, the polarization must be perpendicular to the propagation direction and only two propagation velocities exist: $\mathbf{m}^{S1} = \mathbf{a} \times \mathbf{n}$ and $\mathbf{m}^{S2} = \mathbf{n} \times \mathbf{m}^{S1}$. The first shear wave is polarized so particle displacements are perpendicular to both the fiber direction and the propagation direction; the second wave involves particle displacements perpendicular to the propagation direction, but not to the fiber axis. Hence the propagation speeds are:

$$\mathbf{m}^{S1} : \quad \frac{\omega^2}{k^2} \rho = \mu_L \cos^2 \theta + \mu_T \sin^2 \theta \quad (2.27)$$

and

$$\mathbf{m}^{S2} : \quad \frac{\omega^2}{k^2} \rho = \mu_L + \beta \cos^2 \theta \sin^2 \theta. \quad (2.28)$$

2.3.3 Treatment of viscoelastic effects

If a medium exhibits time-dependent response to loading, it is said to be viscoelastic. In these media internal stresses are developed from components of elastic (Equation 2.8) and viscous response. The precise nature or form of the viscous mechanism(s) in biologic tissue remains elusive. Variations in viscous stress may present uniquely over broad time scales; however in practice, limitations in experimental hardware often results in frequency-limited observations by which multiple models may fit. In this work, viscoelasticity is addressed in two ways: (i) via the correspondence principle, and (ii) by *a priori* constitutive modeling.

Correspondence Principle. The correspondence principle allows the purely elastic equations of motion to be transformed into analogous viscoelastic equations via

Laplace or Fourier transforms [131, 86, 41, 18]. Invoking the correspondence principle allows the real elastic moduli to be replaced with the corresponding complex viscoelastic moduli, without requiring a specific rheological model. For example, the real elastic parameters in an isotropic model are transformed into their complex viscoelastic analogs as follows:

$$\begin{aligned}\mu &\rightarrow G^*(i\omega) = G' + iG'' \text{ and} \\ \lambda &\rightarrow \lambda^*(i\omega) = \lambda' + i\lambda'',\end{aligned}$$

in which the real and imaginary components describe elastic and viscous response, respectively.

Kelvin-Voigt Rheological Model. Alternatively, a specific viscoelastic constitutive model could be assumed *a priori* and the equations of motion developed accordingly. A reasonable model for biological media is the Kelvin-Voigt viscoelastic model. In this model, internal stresses are described by the contributions of elastic and viscous forces in the following way:

$$\sigma_{ij} = C_{ijkl}\epsilon_{kl} + \eta_{ijkl}\dot{\epsilon}_{kl}, \quad (2.29)$$

where the viscosity tensor η_{ijkl} [83] takes an analogous form to the stiffness tensor as

$$\eta_{mn} = \begin{bmatrix} \eta_{11} & \eta_{12} & \eta_{13} & \eta_{14} & \eta_{15} & \eta_{16} \\ & \eta_{22} & \eta_{23} & \eta_{24} & \eta_{25} & \eta_{26} \\ & & \eta_{33} & \eta_{34} & \eta_{35} & \eta_{36} \\ & & \text{sym.} & \eta_{44} & \eta_{45} & \eta_{46} \\ & & & & \eta_{55} & \eta_{56} \\ & & & & & \eta_{66} \end{bmatrix}. \quad (2.30)$$

In a Kelvin-Voigt material, viscous stresses are developed in proportion to the material strain-rate, i.e.,

$$\dot{\epsilon}_{ij} = \frac{\partial \epsilon_{ij}}{\partial t} = \frac{1}{2} \left(\frac{\partial^2 u_i}{\partial t \partial x_j} + \frac{\partial^2 u_j}{\partial t \partial x_i} \right). \quad (2.31)$$

The resolution and time-scale over which elastography measurements are acquired lend well to an isotropic form of the viscosity tensor. In this case, η_{mn} consists of

only two independent viscous constants, ζ and η :

$$\eta_{mn} = \begin{bmatrix} \zeta + 2\eta & \zeta & \zeta & & & \\ \zeta & \zeta + 2\eta & \zeta & & & \\ \zeta & \zeta & \zeta + 2\eta & & & \\ & & & \eta & & \\ & & & & \eta & \\ & & & & & \eta \end{bmatrix}. \quad (2.32)$$

2.3.4 Energy transport in harmonic waves

The application of this work is geared toward better understanding structural-biomechanical properties of the living intact brain. Poynting vectors may prove useful in quantifying shear wave propagation fields measured by magnetic resonance elastography imaging. Poynting vectors describe the direction and rate of the energy-flux crossing a wave surface [18, 7]. The mathematical preliminaries are presented here for future application to MRE data [27].

The Poynting vector P_i is calculated from the product of stress and velocity:

$$P_i = -\sigma_{ij}\dot{u}_j, \quad (2.33)$$

with the stress tensor σ_{ij} and velocity vector \dot{u}_i at each measurement point. With MRE data the constitutive behavior of the medium (brain tissue) is unknown, yet the dominate deformation mode is known to be shear. As such, the Poynting vector could be specialized quantify energy-flux due only to propagating shear waves. Then in cases when an isotropic linear elastic material is assumed, shear stress and shear strain are directly proportional to one another via shear modulus μ . Accordingly, the following approximation to a scaled Poynting vector is suggested:

$$\mathcal{P}_i = -\hat{\epsilon}_{ij}\dot{u}_j, \quad (2.34)$$

with $\hat{\epsilon}_{ij}$ denoting the deviatoric strain tensor.

$$\hat{\epsilon}_{ij} = \epsilon_{ij} - \epsilon_{kk}\delta_{ij}/3. \quad (2.35)$$

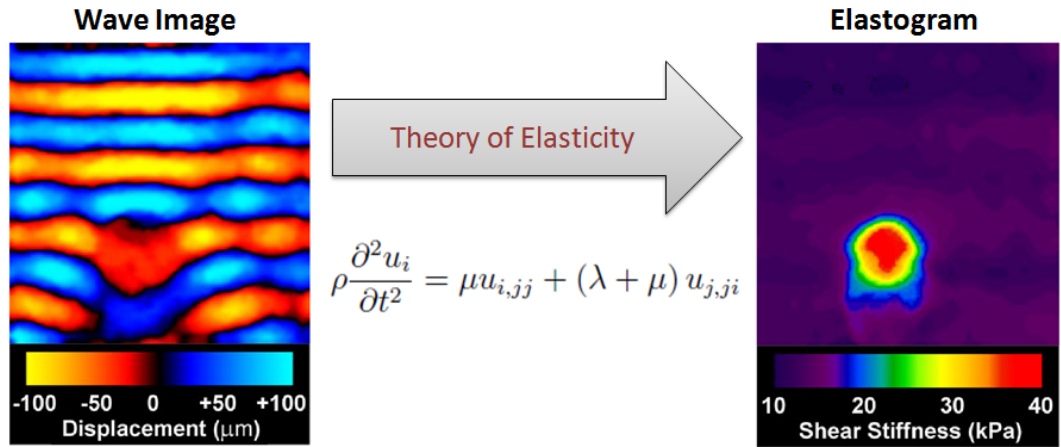


Figure 2.5: The basic concept of MRE imaging is described. Motion-sensitive MR image is used to record shear wave propagation in tissue. A tissue-simulating phantom with an embedded cylindrical inclusion of stiffer material is shown here. The governing equations of motion are inverted to produce an elastogram - an image with contrast proportional to shear modulus. Adapted from Reference [82].

This vector, \mathcal{P}_i , possibly called the “pseudo-Poynting”, then would not carry the usual units of energy-flux, but could be scaled by the shear modulus to quantitatively describe the direction and energy transport of shear waves. This vector could be a reasonable descriptor of the true energy-flux even though the brain is viscoelastic and probably anisotropic in some regions.

2.4 Imaging Methods

2.4.1 Magnetic resonance elastography

Magnetic resonance elastography (MRE) is a novel magnetic resonance imaging (MRI) technique that allows the viscoelastic mechanical properties of biologic tissue to be probed *in vivo* and non-invasively [112]. MRE data are rich in information; four spatiotemporal dimensions (i.e., x , y , z , t) are readily acquired. These specialized MR data can be used to invert the governing equations of wave propagation to approximate isotropic tissue parameters spatially. The result is MR parametric maps (elastograms) with intensity proportional to tissue shear modulus, Figure 2.5.

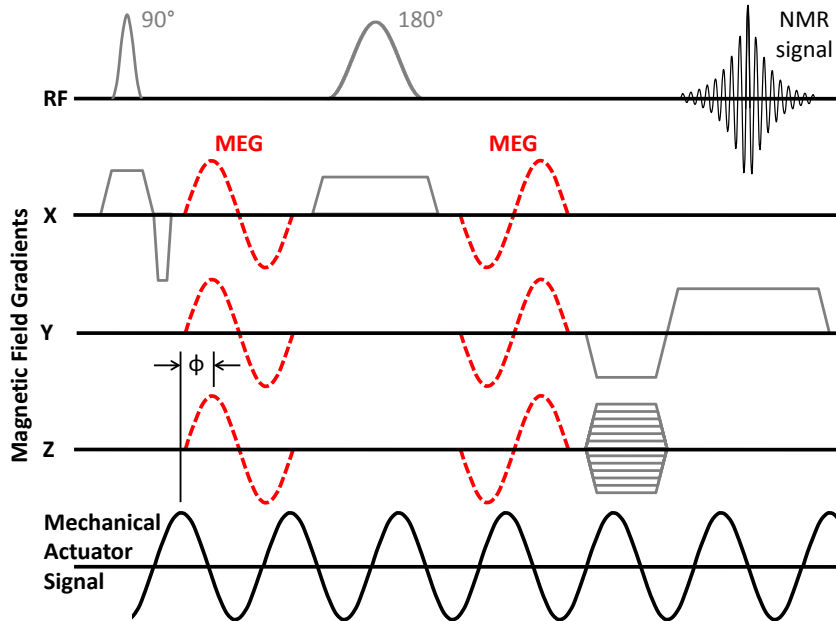


Figure 2.6: In a magnetic resonance elastography pulse sequence, specialized magnetic-field gradients encode harmonic tissue motion produced by an actuator as a shift in NMR signal phase. Applying multiple motion-encoding gradients (MEG) on different channels simultaneously permits acquisition of any motion component. Temporal variations in motion are recorded by time-delaying MEG events relative to the applied mechanical actuation (ϕ). A 1-cycle MEG (dashed) is shown on each gradient channel, so the recorded motion would be perpendicular to an oblique plane in the imaged body. RF-pulse and magnetic-field gradient events required to create a standard MR image are also shown. Reproduced from Reference [29].

MRE provides many advantages for the study of tissue mechanics: (1.) high spatial and temporal resolution permit heterogeneous and viscoelastic material property reconstruction; (2.) *in vivo* and non-invasive experiments preserve structural integrity, anatomical connectivity, and metabolic state during measurement; and (3.) reconstructed material properties can be coalesced with other MRI modalities to elucidate structural and functional properties of tissue, e.g. diffusion tensor imaging (DTI) viz. local diffusion coefficients. MRE measurements provide steady-state harmonic response data at spatial and temporal resolutions of $250 \mu\text{m}$ – 3 mm and 10 – 2000 Hz , respectively, with displacement sensitivities approaching 200 nm [112, 29].

The vast majority of medical (biological) MRI involves imaging of the ^1H nuclear spins of water in tissue. The physical quantity acquired to produce MR images are the radio-frequency (RF) signals produced by nuclear spins precessing in the plane

perpendicular to the static magnetic-field. An MRE pulse sequence differs from a standard MRI sequence in that additional temporally-varying “motion-sensitizing” magnetic-field gradients are included (Figure 2.6). These gradients shift the phase (i.e., accumulated frequency) of the detected signal in proportion to spin displacement. If the proton spin packet undergoes harmonic mechanical excitation and is subjected to a sinusoidal, motion-encoding magnetic-field gradient $G_i \sin(\omega_g)$ parallel to an orthogonal reference coordinate i , the shift in NMR signal phase θ_i at position x_0, y_0, z_0 , is governed by:

$$\theta_i(x_0, y_0, z_0, \phi) = \gamma \int_0^t G_i \sin(\omega_g \tau + \phi) u_i \sin(\omega_d \tau) d\tau. \quad (2.36)$$

In this equation, G_i and ω_g are the motion-encoding gradient amplitude and oscillating frequency, respectively; $u_i(x_0, y_0, z_0)$ is the amplitude of the displacement component of the spin packet at this location and ω_d is the mechanical actuator driving frequency; γ is the gyromagnetic ratio of ^1H nuclei.

The synchronization delay ϕ results in a temporal phase shift between the motion of a particular spin packet and the motion-encoding gradient. If multiple phase images are acquired, each with a different synchronization delay (corresponding to a fraction of the actuation period), a time history of spin phase (i.e., displacement) is measured. If the experiment is repeated three times, with the motion-encoding magnetic-field gradients aligned along a different axis of the reference coordinate system each time, all three components of spin-packet motion (i.e., u_1, u_2, u_3) can be imaged.

The amplitude of each spin-packet displacement component $u_i(x_0, y_0, z_0)$ is directly related to the amount of spin phase $\theta_i(x_0, y_0, z_0)$ accrued by a scaling factor proportional to the amplitude, frequency, and duration of the applied motion-encoding gradient. Sensitivity to motion is greatest when the mechanical actuation frequency ω_d and motion-encoding gradient frequency ω_g are equal ($\omega = \omega_d = \omega_g$) and the oscillating gradients are synchronized with the applied motion for an integer number of cycles n . In this case, for sinusoidal encoding and excitation motion, the spin-phase displacement sensitivity can be calculated, in general as:

$$\frac{u}{\theta} = \frac{\omega}{\gamma G \pi n}.$$

2.4.2 Diffusion tensor imaging

Diffusion is the process whereby material is transported from one part of a system to another as a result of random molecular motion [32]. In the context of MR imaging, measurement of tissue diffusivity means tracking the molecular motion of water (i.e., ^1H protons). Starting in the late 1950's, the concept of using magnetic resonance to measure apparent diffusion coefficients (ADC) in structurally isotropic and homogeneous media was established [168, 157, 158]. Later, Bassler and various colleagues [11, 10, 9] extended this work to measure diffusion coefficients in anisotropic media. They called this technique diffusion tensor imaging (DTI) and suggested it be used to quantify the micro-structural properties of biological tissues.

The basic concept of DTI and its potential utility as a clinical imaging tool are straightforward. Water will diffuse uniformly in tissues which possess structural isotropy (e.g., gray matter, etc.) because the molecular motion of water is not restricted by micro-structures such as membranes or fiber tracts. On the contrary, in tissues which possess structural anisotropy (e.g., white matter, muscle, etc.) water will diffuse non-uniformly since the molecular motion of water is more restricted in some directions by micro-structures. A change in the directional diffusivity of water in tissue might suggest an actual change in tissue structure and has been suggested as a marker of disease pathology and injury [12, 59, 88, 50, 74].

The theoretical tenants of DTI are well established [11, 10, 9], so only a brief overview is provided here. Diffusion of water in an anisotropic medium can be described by Fick's first law:

$$\begin{Bmatrix} J_1 \\ J_2 \\ J_3 \end{Bmatrix} = - \begin{bmatrix} D_{11} & D_{12} & D_{13} \\ D_{21} & D_{22} & D_{23} \\ D_{31} & D_{32} & D_{33} \end{bmatrix} \begin{Bmatrix} \frac{\partial C}{\partial x_1} \\ \frac{\partial C}{\partial x_2} \\ \frac{\partial C}{\partial x_3} \end{Bmatrix}, \quad (2.37)$$

where diffusive flux vector J_i is related to the concentration gradient vector $C_{,j}$ through the symmetric effective diffusion tensor D_{ij} [10]. Consider the spin-echo diffusion weighted imaging sequence presented as Figure 2.7. NMR signal intensity S can be related to an apparent diffusion coefficient through the applied diffusion weighting magnetic-field gradient vector G_i as follows:

$$\ln \left(\frac{S(b_{ij})}{S(b_0)} \right) = - [b_{11}D_{11} + b_{22}D_{22} + b_{33}D_{33} + 2b_{12}D_{12} + 2b_{23}D_{23} + 2b_{13}D_{13}]. \quad (2.38)$$

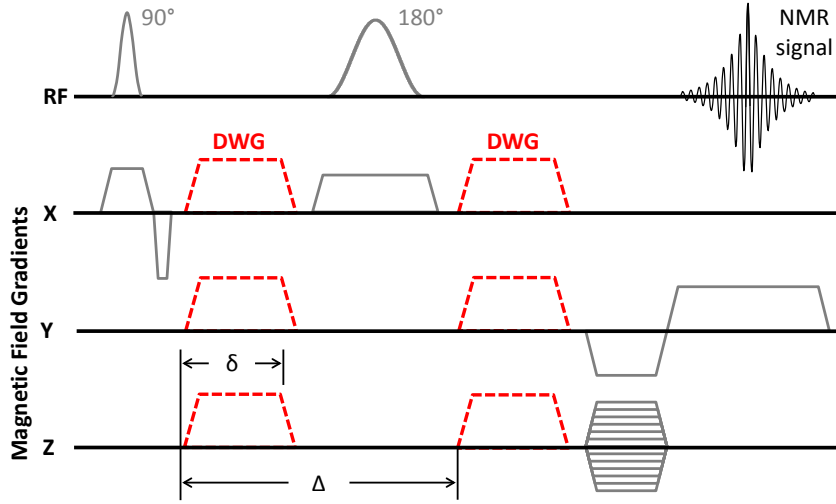


Figure 2.7: A spin-echo magnetic resonance imaging pulse sequence can be modified to measure diffusion by the addition of diffusion weighting magnetic-field gradients (DWG) on each side of the 180° refocusing RF pulse. Applying DWG of various duration (δ), spacing (Δ), and magnitude (G) along one or more gradient axes simultaneously creates diffusion weighted images (DWI) whose signal intensities can be related to the incoherent displacement of water of varying signal intensity.

$S(b_0)$ is the signal intensity absent a diffusion gradient vector and $S(b_{ij})$ is the signal intensity given a particular diffusion gradient vector orientation. Since b_{ij} will be coupled to both the applied diffusion gradients and those used for imaging, the specific form of the b_{ij} depends on the particular imaging sequence and protocol employed [115, 95]. In the absence of imaging gradients (e.g., spectroscopy experiment),

$$b_{ij} = \gamma G_i G_j \delta^2 (\Delta - 1/3\delta) \quad (2.39)$$

for trapezoidal diffusion gradients with negligible rise time having amplitude G , spacing Δ , and duration δ (Figure 2.7).

In principle, to solve for D_{ij} at each voxel only seven measurements are required – corresponding to six non-collinear G_i and one b_0 . However, in practice, measurement noise is a factor. Robustness is obtained by over-determining the problem with k

measurements:

$$\begin{Bmatrix} \ln[S(b_{ij}^1)] \\ \vdots \\ \ln[S(b_{ij}^k)] \end{Bmatrix} = - \begin{bmatrix} b_{11}^1 & b_{22}^1 & b_{33}^1 & b_{23}^1 & b_{13}^1 & b_{12}^1 & -\ln[S(b_0)] \\ & & & \vdots & & & \vdots \\ b_{11}^k & b_{22}^k & b_{33}^k & b_{23}^k & b_{13}^k & b_{12}^k & -\ln[S(b_0)] \end{bmatrix} \begin{Bmatrix} D_{11} \\ D_{22} \\ D_{33} \\ 2D_{23} \\ 2D_{13} \\ 2D_{12} \\ 1 \end{Bmatrix} \quad (2.40)$$

D_{ij} is a second rank tensor and can be diagonalized via eigenproblem. In the diagonalized form, the principal eigenvector λ_1 describes the direction of preferential diffusivity and is oriented with the tissue fiber direction (Figure 2.8). It should be noted that DTI data describe structural anisotropy of tissue. It does not describe mechanical anisotropy, which is the relationship between applied load and deformation.

2.4.3 Application of MRE and DTI data for anisotropic material inversion

Diffusion tensor imaging provides insight into tissue structure which could be harnessed to better characterize tissue mechanics when probed by magnetic resonance elastography. As previously discussed, propagation of pure shear waves in an incompressible transversely isotropic medium is governed by two shear moduli μ_L and μ_T , cf. Equation 2.26. The local shear wave velocity will depend on the wave propagation direction, particle polarization direction, and the axis of material symmetry (i.e., fiber axis) at each point in the medium. In theory, if shear waves are induced in the media that activate both shear moduli it is possible to iteratively solve for the two shear moduli by incrementally rotating the material fiber axis until an established error metric is minimized [151]. Computational expense and experimental measurement error make this “brute force” technique unattractive. However, DTI data could establish the material fiber axis relative to MRE displacement measurements, thereby eliminating the need to iteratively solve the equation of motion.

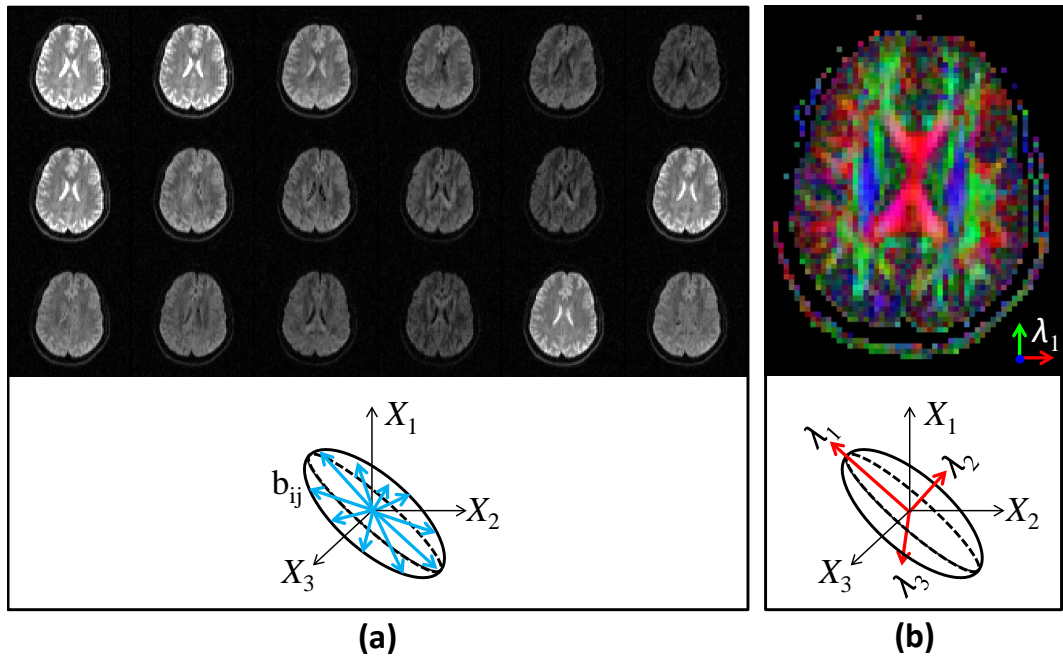


Figure 2.8: (a) Each diffusion weighted image corresponds to a specific b_{ij} and is related to the amplitude and direction of an applied diffusion magnetic-field gradient vector G_i . Multi-variable regression permits reconstruction of the diffusion tensor with as little as seven non-collinear measurements. (b) Principal directions of diffusivity are obtained by diagonalizing the diffusion tensor and have been shown to be aligned parallel (λ_1) and perpendicular (λ_2, λ_3) to tissue fibers. (S002)

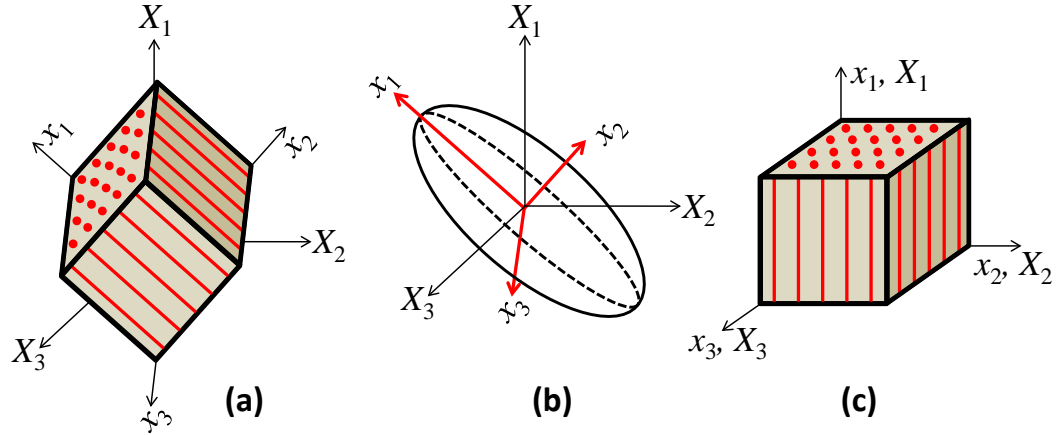


Figure 2.9: Diffusion tensor data can be used to align axes of material symmetry (x_i) with MRE displacement data acquired in a laboratory reference frame (X_i). (a) The native material orientation with respect to laboratory coordinate system. (b) The diffusion ellipsoid calculated from DTI data. (c) The eigenvectors of the diffusion tensor can be used transformation of material orientation to laboratory coordinates.

Here we propose to use the principal eigenvector λ_1 of the diffusion tensor to identify the axis of material symmetry x_i relative to the fixed laboratory reference frame X_i in which MRE displacement data components are measured (Figure 2.9). A spatiotemporal directional filter can be applied to shear wave fields calculated, from MRE displacement data, to extract the wave propagation direction relative to the same laboratory reference frame. The angle θ between the shear wave propagation direction and fiber axis can be calculated to extract the transversely isotropic shear moduli μ_L and μ_T based on local estimates of the shear wavelength k (Equation 2.26). Coalescing DTI and MRE data aims to reduce uncertainty in anisotropic material property estimates, as well as computational expense.

Chapter 3

Viscoelastic Properties of Soft Gels: Comparison of Magnetic Resonance Elastography and Dynamic Shear Testing

3.1 Overview

Previous MRE validation studies have been conducted with bench-top mechanical tests, but were performed at actuation frequencies lower than MRE. Noted disparities in the measurements obtained were owed to frequency-dependent viscoelastic effects. In this study, a novel dynamic shear test (DST) was used to measure the viscoelastic shear modulus of a tissue-mimicking material at frequencies high enough for direct comparison to those commonly employed for MRE. Viscoelastic properties were extracted from DST data obtained at 20–200 Hz by use of a closed form solution which considered inertial effects induced at these higher actuation frequencies. MRE was performed in cylindrical phantoms of the same material and at 100–400 Hz, in a frequency range overlapping the DST measurements. MRE measured displacement fields were fit to a viscoelastic form of Navier’s equation using a total least squares approach to obtain local estimates of viscoelastic shear modulus. DST estimates of the storage modulus G' increased with frequency from 0.868 kPa at 20 Hz to 0.973 kPa at 200 Hz ($n = 16$). MRE estimates of G' increased with frequency from 1.06 kPa at 100 Hz to 1.15 kPa at 400 Hz ($n = 6$). The loss factor ($\eta = G''/G'$) also

increased with frequency for both test methods: 0.06 to 0.14 for DST and 0.1 to 0.23 for MRE, over the same respective frequency ranges. Close agreement of measurements obtained with these two tests, at overlapping frequencies, indicates our MRE inversion technique is accurate over a wide frequency range. Low signal-to-noise ratio, long shear wavelengths, and boundary effects produced measurement artifacts that were found to increase residual fitting error. This reinforces the use of an error metric to assess confidence in local viscoelastic estimates obtained by MRE.

The material presented in this chapter is published in *Physics in Medicine and Biology* (Okamoto, Clayton, Bayly, 2011)².

3.2 Introduction

Magnetic resonance elastography (MRE) is a novel experimental technique for probing the dynamic shear modulus of soft biological tissue non-invasively in living subjects [112]. To perform MRE, shear waves are excited by external harmonic mechanical actuation, and a standard MRI scanner equipped with a specialized imaging sequence is used to capture spatiotemporal images of the propagating wave field. Regional estimates of tissue shear modulus are made by local analysis of the wave field using wavelength measurement, direct inversion of the wave equation, or inverse finite element methods. These modulus estimates can be used to assess baseline properties of healthy tissues or to identify local or regional changes in tissue properties associated with disease.

The majority of MRE studies have estimated the elastic shear modulus, often at a single frequency. The accuracy of the method has been assessed by comparing estimates of the elastic shear modulus in tissue analogs to those provided by mechanical tests or ultrasound elastography [121]. The most common phantom materials include agar [112, 54, 134] and gelatin [36, 23, 34, 6] or a blend of these materials [121, 60] with

²Author Contributions: R.J.O. and E.H.C. contributed equally to this study. R.J.O. designed, performed, and analyzed DST experiments. E.H.C. designed and performed MRE experiments and developed the MRE inversion algorithm. R.J.O. wrote the manuscript, formulated analytic solutions, and adapted MRE inversion to include TLS fitting. P.V.B. conceived the project. All authors reviewed and discussed the manuscript. For completeness and continuity, the entire study is recapitulated here; specific contributions of other authors are noted in the text.

shear modulus values reported in the range of 0.5 to 60 kPa. A variety of mechanical test methods have been used: static compression [112, 126, 54, 23], oscillatory linear shear [134], oscillatory rotational shear [6], and oscillatory compression [35, 125]. These studies have shown reasonable agreement between the elastic shear moduli measured with MRE and mechanical tests, even though the frequency range of direct mechanical testing is usually lower than the frequency range of MRE. Similar trends in the elastic shear moduli measured by MRE and transient ultrasound elastography were found for frequencies from 60 to 220 Hz [121].

More recently, MRE has been used to characterize the components of the viscoelastic shear modulus in brain, liver, and skeletal muscle tissue [152, 72, 49, 142, 73, 160, 177, 29, 133]. Substantial differences in viscoelastic shear modulus values of brain tissue have been reported. Differences in experimental setup, data collection, and data analysis may be confounding factors.

Oscillatory, or dynamic, shear testing (DST) has been frequently used to characterize soft biomaterials. Thin samples of the material are subject to oscillatory shear strains. These tests may be done on a commercial rheometer [174, 17, 64] or a custom-built system [4, 3, 89]. In these systems, shear force or shearing torque is measured and converted to shear stress, usually over a range of frequencies, and the data are analyzed to obtain the complex shear modulus. The data analysis method assumes that the shear displacement is linear and shear strain is constant through the thickness of the sample. In soft materials, very thin samples are used to avoid inertial effects (shear waves) at higher frequencies. As the thickness of the sample decreases, it is more difficult to cut samples of uniform thickness and to maintain their structural integrity. Without inertial correction, shear modulus estimates in soft materials are limited to low frequencies [89]. Investigators have used MRE to quantify the viscoelastic shear modulus of porcine brain tissue [174] and bovine liver tissue [71], and directly compared results to oscillatory rheometry. Both studies showed qualitative agreement in the trend of the viscoelastic response with frequency, but rheological tests of porcine brain tissue were performed at a much lower frequency (0.1 to 10 Hz) than MRE (80 to 140 Hz). Hence, quantitative interpretation of results is difficult. Hrapko and co-workers [64] have emphasized the wide range of values of brain tissue shear modulus obtained from mechanical tests, due to differences in temperature, hydration, sample size and boundary conditions.

This study a soft, homogeneous, tissue analog is used to assess the accuracy of MRE-based estimates of viscoelasticity. Bench-top mechanical tests and MRE were performed in an overlapping frequency range to allow direct comparison of frequency-dependent viscoelastic behavior. Dynamic shear testing in this study was deliberately performed in a regime in which shear waves affect the force-displacement relationship. Shear wave effects in DST are explicitly taken into account as they provide valuable information for comparison to corresponding MRE measurements.

MRE studies were carried out using the same tissue analog in a cylindrical geometry. Axial displacement of a central rod created radially propagating shear waves. MRE displacement data is analyzed both by (1) direct local inversion of the shear wave equation and (2) a closed-form solution of the specific boundary value problem. By using two different approaches for analysis of shear wave displacement fields, we are able to investigate the effect of numerical differentiation, discretization error and local fitting error on estimates of viscoelasticity.

3.3 Methods

3.3.1 Gelatin preparation: MRE phantoms and DST samples

Food grade gelatin (Knox) was mixed with de-ionized water and glycerol to produce a mixture of 2.8% w/w gelatin. Glycerol stabilizes gelatin mixtures by increasing their melting temperature [69] and shear modulus [116, 13], and was also found to reduce water loss during mechanical testing. First, 4.03 g of gelatin was sprinkled on 70 g of room-temperature deionized water and allowed to stand for approximately 10 minutes. 70 g of glycerol was heated to 50°C in a water bath, and added to the gelatin/water mixture, then heated to 60°C in a water bath to fully dissolve the gelatin. The final mixture had a density of approximately 1.1 g/cm³.

MRE phantoms were created by pouring 85 g of the warm gelatin mixture into a 45 mm diameter cylindrical container (Figure 3.1a), filling the container with gelatin to a depth of 48–50 mm. The actuator fit into a custom cap placed on top of the container. A 3 mm diameter polypropylene actuation rod extended approximately

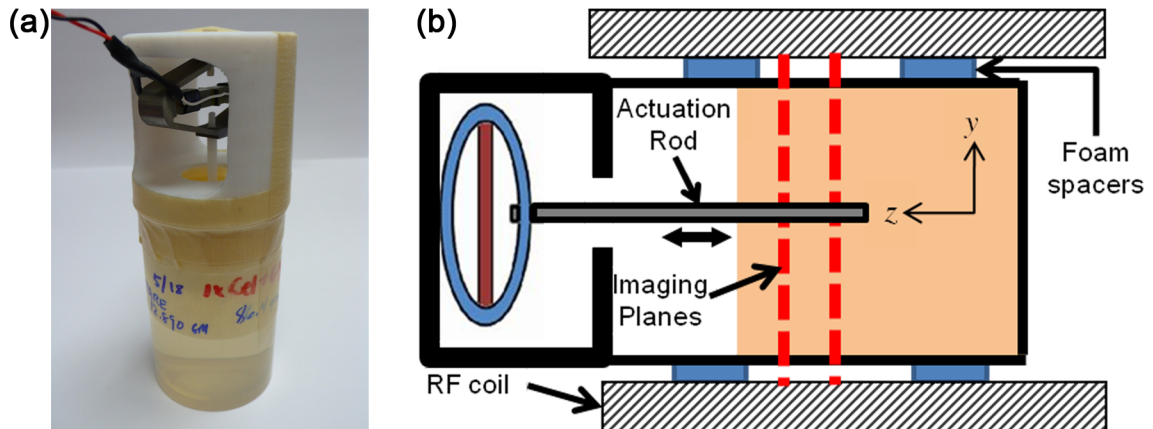


Figure 3.1: MRE experimental setup. (a) MR phantom; (b) orientation of phantom in scanner. The vertical dashed lines show approximate bounds of the transverse planes imaged. Reproduced from Reference [119].

20 mm into the mixture. After the mixture set, the entire container was sealed and refrigerated overnight at 4°C.

DST samples were prepared by pouring 39.8 g of the warm gelatin mixture into 100 mm cell culture dishes. The resulting samples were approximately 5.8 mm thick. After the gelatin mixture had set, the dishes were sealed and refrigerated overnight at 4°C. A circular punch (15 mm dia.) was used to punch cylindrical samples from the gel. Each cylindrical sample was weighed before and after testing.

3.3.2 MRE data acquisition and analysis

Elastography data were obtained for each phantom at 4.7 T using a Varian Direct-Drive small-animal MR scanner. The scanner consists of an Oxford horizontal-bore magnet, Magnex self-shielded gradient coils, and high-performance, gradient power amplifiers (Copley Controls Corp.) capable of providing 45 G/cm peak magnetic-field gradient amplitude within 0.20 msec. MRE data were collected with a commercial quadrature volume coil (Agilent/Varian).

As shown in Figure 3.1, the gelatin-filled container was placed inside the RF imaging coil horizontally. Small foam spacers were used to center the container in the

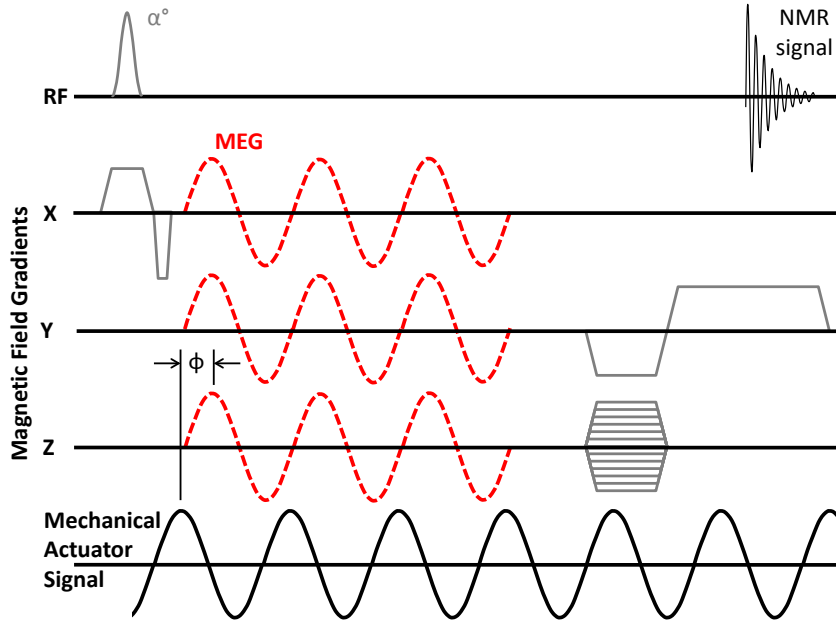


Figure 3.2: A gradient echo MR imaging sequence was modified to acquire elastography data. Sinusoidal motion-encoding magnetic-field gradients (MEG) are included with standard RF and magnetic-field gradient events required to form an MR image. MEGs are synchronized with the applied mechanical motion by the phase shift parameter Φ . A 3-cycle MEG (dashed) is shown on each gradient channel. In this example, motion-encoded phase images are acquired with contrast proportional to displacements perpendicular to an oblique plane in the imaged body.

coil. Mechanical vibrations were generated by an amplified piezoceramic-actuator (APA100M-NM, Cedrat Technologies) and transmitted to the sample via a polypropylene rod that had been embedded in the gelatin mixture before it set. The actuator was powered by a low-current, high-voltage amplifier (EPA 105, Piezo Systems Inc). A sinusoidal voltage waveform was supplied to the amplifier by a transistor-transistor logic (TTL) equipped function generator (FG-7002C, Ez Digital Co., Ltd.).

A customized gradient-recalled echo MRI pulse sequence was developed to record spatiotemporal partial motion as a shift in NMR signal phase for this study Figure 3.2. The imaging sequence was triggered by transistor-transistor logic (TTL) pulse, allowing a function generator to control image acquisition and scanner-actuator synchronization. Images at different points in time of a wave cycle were obtained by a programmable phase-delay Φ between the actuator and motion-encoding gradients.

The actuator was run uninterrupted for the duration of each experiment to ensure steady-state harmonic material response was measured.

A central section of each phantom was imaged with 11 contiguous trans-axial slices in an interleaved manner. The image acquisition parameters were: resolution: 250 x 250 x 500 μm^3 ; TR/TE: 200/13.75 msec; flip \angle : 25°. Two excitations were acquired and averaged. A magnetic field gradient amplitude of 8 G/cm was used throughout for motion encoding. The number of MR motion-encoding gradient cycles varied with the actuation frequency from 1 to 4 to accommodate constant TR/TE imaging parameters. Phase contrast was doubled by acquiring two sets of motion-encoded data, one each with positive and negative polarity motion-encoding gradients, which were subtracted from one another. Eight time points were acquired per actuation cycle.

MRE experiments were performed at actuation frequencies of 100, 150, 200, 250, 325, 350 and 400 Hz. With the exception of 100 and 400 Hz, the order of the actuation frequencies was randomized for each MRE experiment. The amplitude of the imposed displacement was independently measured with a special bench-top test rig and a capacitance probe. The z -displacement (u_z) amplitude of the gelatin-embedded polypropylene rod ranged from approximately 40 μm at 100 Hz to less than 10 μm at 400 Hz. During each experiment, all three displacement components [u_x, u_y, u_z], were acquired for a single frequency from 100 to 400 Hz. For all other frequencies in that experiment, only the through-image-plane component of motion u_z was recorded. Acquisition time was approximately 22 minutes per displacement component, and the total imaging time for each experiment was approximately 5 hours.

Phase wrapping artifacts, if present, were removed via commercial software (Phase Vision Ltd). The relationship between the phase and displacement is governed by the amplitude of the motion encoding gradient G_0 , and number of motion encoding cycles N . The proportionality constant for converting phase ϕ (in radians) into displacement u , including the factor of two introduced by positive and negative polarity image subtraction, is given by the following:

$$\frac{u}{\phi} = \frac{\omega}{2N\pi G_0\gamma}, \quad (3.1)$$

where ω is the driving frequency (rad sec⁻¹); γ is the gyromagnetic ratio for ¹H nuclei (26.537 x 10⁴ rad sec⁻¹ G⁻¹), and N is the number of motion encoding cycles. Equation 3.1 is valid for sinusoidal motion-encoding gradients with the frequency equal to the driving frequency.

For each voxel, displacement data from the eight acquisition phases $u_z(x, y, z, t)$ were Fourier transformed in the time domain, and the coefficient of the fundamental harmonic $U_z(x, y, z, \omega)$ was extracted, resulting in three-dimensional (3D) field of these complex frequency domain coefficients. A 3D Gaussian filter was applied to the entire 11 image stack of complex displacement data using the smooth3 function in MATLAB (R2009a, The MathWorks) with a filter kernel of 13 x 13 x 7 pixels (3.0 x 3.0 x 3.0 mm) in the x , y , and z directions and a filter standard deviation of 3 pixels (0.75 mm). To remove edge effects in the $x - y$ plane, only voxels whose entire smoothing kernel lay within the masked region of the field of view were included in the smoothed displacement field.

Direct least-squares inversion of the wave equation

The correspondence principle was used to transform the linear, isotropic, locally homogeneous, elastic Navier equation into its viscoelastic analogue. The components of the complex modulus G^* were estimated by fitting the axial component of displacement to a reduced equation of motion in which the dilatational component of displacement was neglected [29]:

$$(G' + iG'') \nabla^2 U_z(x, y, z, \omega) = -\rho\omega^2 U_z(x, y, z, \omega), \quad (3.2)$$

where ρ is the material density (1100 kg/m³). A simple central difference scheme was used to approximate the Laplacian of the displacement field. Inversion was performed by a local total least-squares (TLS) fit using a 13 x 13 x 7 kernel. Details of the inversion method are given in Appendix A. The mean value and standard deviation of G' and G'' were reported using only voxels in which the normalized residual error of the local fit was less than 0.5. The mean values of G' and G'' from different experiments were grouped by frequency. For each frequency, the mean values of G' and G'' for all six experiments and the corresponding standard deviations were computed.

Analytical model and closed-form solution

[R.J.O. contributed this section.]

The MRE phantom geometry and the axial displacement due to the harmonic vibration of the displacement rod can be described accurately by a straightforward mathematical model. The appropriate boundary value problem is posed, using the wave equation in cylindrical coordinates and the viscoelastic correspondence principle. This model was used to independently estimate the values of G' and G'' from shear wave displacement data. Since the system is approximately axisymmetric, the displacement field is assumed to depend only on the radius r , neglecting any variations in the angular coordinate θ . Under these conditions, the reduced equation of motion in cylindrical coordinates becomes:

$$(kr)^2 \frac{d^2 U_z}{d(kr)^2} + kr \frac{dU_z}{d(kr)} + (kr)^2 U_z = 0, \text{ where } k = \sqrt{\frac{\rho\omega^2}{G^*}}. \quad (3.3)$$

For a viscoelastic material, the wavenumber k and the displacement $U_z(kr)$ are complex quantities. The solution to the boundary value problem is the sum of Bessel functions of the first kind (J_0) and second kind (Y_0), both of order zero:

$$U_z(kr, \omega) = AJ_0(kr) + BY_0(kr). \quad (3.4)$$

We found analytical solutions to Equation 3.4, specifying boundary conditions at the outer radius of the actuating rod ($r = r_i$) and at the outer radius of the gel (r_0) that matched the measured displacements at those locations for each frequency and experiment. The values of the constants A and B were determined from the boundary conditions. For an outwardly propagating wave, the displacement at the outer radius, $U_z(r_0)$, is zero and, if the amplitude of the displacement at the actuating rod is u_{ri} , then:

$$A = \frac{u_{ri} Y_0(kr_0)}{J_0(kr_i) Y_0(kr_0) - J_0(kr_0) Y_0(kr_i)}; \quad B = -A \frac{J_0(kr_0)}{Y_0(kr_0)}. \quad (3.5)$$

At frequencies of 250 Hz and above, we also observed an inwardly propagating wave (i.e. the displacement at r_0 was not zero due to vibration of the gel container). With the same approach, we found the values of constants describing the inwardly

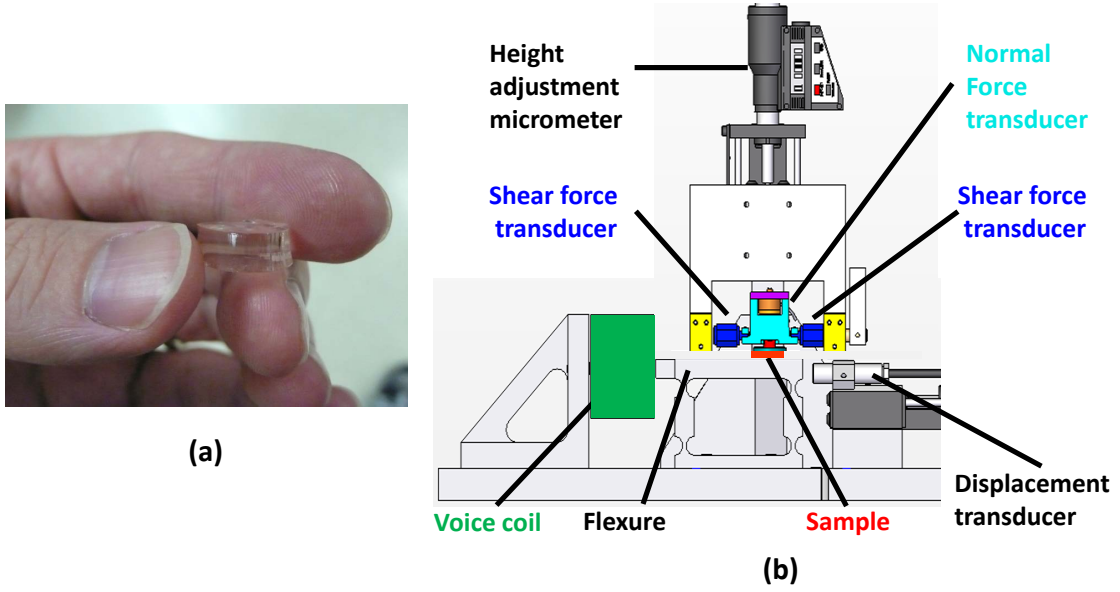


Figure 3.3: Dynamic shear test (a) sample and (b) setup. Samples were placed on the tester and subjected to small amplitude vibrations (0–200 Hz). Adapted from Reference [119].

propagating wave in terms of the displacement measured at the outer radius, u_{r_0} :

$$A' = \frac{u_{r_0} Y_0(kr_i)}{J_0(kr_0) Y_0(kr_i) - J_0(kr_i) Y_0(kr_0)}; \quad B' = -A' \frac{J_0(kr_i)}{Y_0(kr_i)}. \quad (3.6)$$

The four constants A , B , A' , B' were calculated determined from U_z values at r_0 and r_i for $\theta = 0$ and $\theta = 180$ at each frequency using a single imaging plane (slice 6 of 11). Then the values of the complex modulus that best fit the unfiltered z-displacement data at that frequency were determined using a non-linear fitting function. This produced a global estimate of G' and G'' based on a complete 2D displacement field.

3.3.3 DST data acquisition and analysis

[R.J.O. contributed this section.]

In order to overcome the frequency limits of conventional DST for our soft gel material, we extended the frequency regime of DST by deliberately introducing shear waves in the sample, which created corresponding peaks in the measured shear force. The frequency and magnitude of this peak allowed us to determine the complex shear

modulus of the material up to 200 Hz using a custom built DST system (Figure 3.3b). The mass, m , and the approximate thickness of each punched circular DST sample were measured prior to testing. A punched circular DST sample (Figure 3.3a) was placed on the flexure, which was displaced horizontally by the voice coil, causing the lower surface of the sample to undergo small amplitude (≈ 0.03 mm) horizontal oscillations. We used a circular sample because it was easier to punch circular samples than to trim rectangular samples of consistent size. The voice coil was excited with sinusoidal oscillations at a constant frequency or with a chirp, which sweeps through frequencies from 0 to 200 Hz in 15 seconds using a SigLab data acquisition system (Spectral Dynamics, Inc). The horizontal displacement of the flexure, u_x , was measured with a capacitance probe. The difference between the signals of two piezoelectric force transducers (Model PCB209C, PCB Electronics) was used to calculate the net shear force when the sample is in contact with the upper plate. The 200 Hz frequency limit was chosen to avoid mechanical resonances of the upper assembly which occurred at frequencies above 280 Hz, as measured by an accelerometer attached to the upper assembly.

With the flexure operating at a low frequency, the vertical position of an upper assembly was adjusted with a digital micrometer until the upper circular plate touched the sample, as indicated by the presence of a shear force signal and a slight change in normal force. Because the shear force transducers are stationary, inertial effects in the shear force measurement are limited to the sample. Once contact was established, the thickness of the sample was computed. The sample was compressed by 5% of this measured thickness h to provide consistent contact on the upper and lower surfaces [25] and a chirp signal was applied to the voice coil. Time domain signals from the force and displacement transducers were transformed into the frequency domain and a complex transfer function (net shear force/flexure displacement) was obtained.

Data analysis was performed using custom scripts in MATLAB. As shown in Figure 3.4, shear force F_s is divided by the sample cross-sectional area A to obtain an average shear stress. The amplitude of the harmonic shear strain is initially assumed uniform through the sample thickness and estimated as the amplitude of vibration u_o divided by sample thickness h . The apparent complex shear modulus G_{app}^* is calculated as

$$G_{app}^*(i\omega) = \frac{\tau(i\omega)}{\epsilon(i\omega)} = \frac{F_s(i\omega)/A}{u_o(i\omega)/h}. \quad (3.7)$$

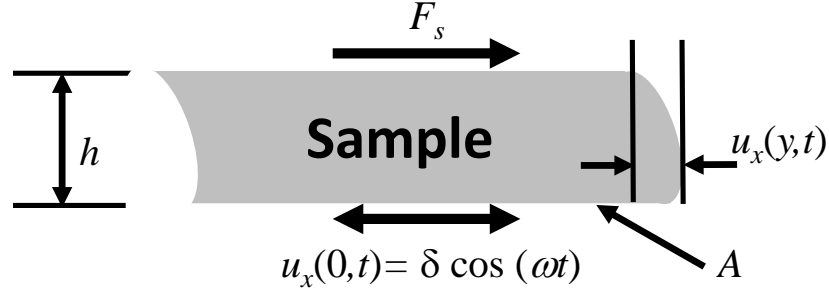


Figure 3.4: Dynamic shear test sample nomenclature used in Equations 3.7–3.13. Adapted from Reference [119].

Inertial load correction

[R.J.O. contributed this section.]

As other investigators [4, 89] have commented, sample inertia can cause shear waves to propagate within the DST sample. This invalidates the assumption of uniform shear strain and leads to deviations between the apparent shear modulus and the shear modulus of the material being tested. These deviations are usually avoided by using thin samples or testing at low frequencies. Because we wanted to directly obtain estimates of shear modulus of soft materials at frequencies above 100 Hz, we could not avoid measurements that included inertial effects in the sample. For thick samples of the gelatin/glycerol mixture, we found that two peaks in the shear force measurements were observed in the tested frequency range of 0 to 200 Hz.

Using an analytical model described by Berry [19], we derived a relationship between the measured force/displacement relationship and the complex shear modulus of the material. This equation is valid when the shear force is measured on the stationary surface of the gel, as in our test setup. Shuck and Advani [148] derived a similar relationship for thick circular samples of brain tissue undergoing torsional shear testing—in those experiments the shear force transducer was located on the oscillating surface, similar to the setup in most oscillatory rheometers.

The displacement, $u_x(y, t)$, is assumed to be the separable product $U_x(y) \exp(i\omega t)$. The one-dimensional wave equation

$$G^* \frac{d^2 U_x}{dy^2} + \rho \omega^2 U_x = 0 \quad (3.8)$$

is determined by force balance in the x -direction. G^* is the complex shear modulus and ρ is the material density. The homogeneous solution for $U_x(y)$ is:

$$U_x(y) = C_1 \cos(ky) + C_2 \sin(ky); \quad k^2 = \frac{\rho\omega^2}{G^*}. \quad (3.9)$$

Applying the boundary conditions $U_x(0) = u_0$ and $U_x(h) = 0$, the solution for the displacement is:

$$u(y, t) = u_0 [\cos(ky) - \cot(kh) \sin(ky)] \exp(i\omega t). \quad (3.10)$$

The shear stress at the stationary surface ($y = h$) is

$$\begin{aligned} \tau_{xy} &= G^* \frac{\partial u}{\partial y} \Big|_{y=h} \\ &= -G^* k u_0 [\sin(kh) + \cot(kh) \cos(kh)] \exp(i\omega t) \\ &= -G^* \frac{k u_0}{\sin(kh)} \exp(i\omega t). \end{aligned} \quad (3.11)$$

If the material is elastic, then G^* is a real quantity and τ_{xy} is unbounded when kh is equal to multiples of π , or when

$$h = \frac{n\pi}{k} = \frac{n\pi}{\omega} \sqrt{\frac{G}{\rho}}; \quad n = 1, 2, \dots \quad (3.12)$$

For a viscoelastic material $\sin(kh)$ is complex and the maximum magnitude of τ_{xy} is bounded. Given h , the value of ω at which τ_{xy} reaches a maximum will depend upon the specific functional form of G^* and the values of the function's parameters. In general, the ratio of maximum magnitude of τ_{xy} to u_0 will be smaller for more viscous materials. For the model, the relationship between the shear stress and the nominal shear strain (u_0/h), i.e. the apparent modulus, is given by:

$$G_{app}^* = \frac{\tau(i\omega)}{u_0/h} = -G^* \frac{kh}{\sin(hk)}. \quad (3.13)$$

DST data were fit to three different viscoelastic material models: (i) spring-pot [77], (ii) standard linear solid (or Zener) model, and (iii) fractional Zener model [78]. These models have been used for interpreting MRE data obtained at multiple frequencies [72, 150]. The best-fit values of material model parameters were obtained for each sample

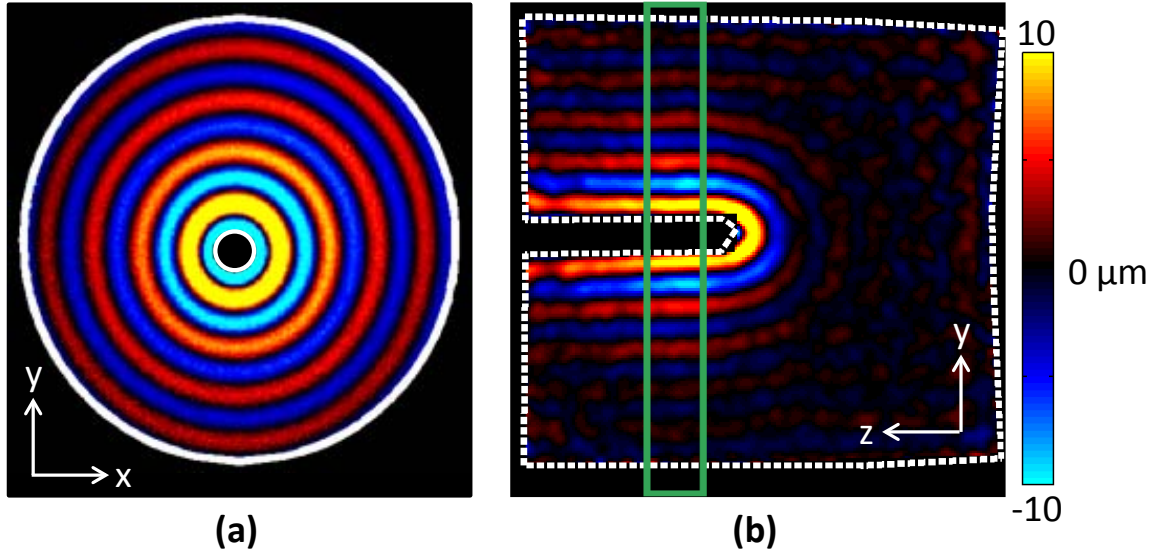


Figure 3.5: Images of the u_z displacement field support the plane wave assumption used for MRE data inversion. (a) Axial and (b) coronal images of the displacement field show that within the analysis volume, boxed in green, planes of wave symmetry exist along the z -axis. (250 Hz) Adapted from Reference [119].

by minimizing the difference between the apparent modulus given by Equation 3.7 and determined from experimental data and the predicted apparent modulus obtained from the closed-form solution given by Equation 3.13. These fits were performed in MATLAB using standard functions and customized scripts.

3.4 Results

3.4.1 Estimates of viscoelasticity from MRE data

MRE experiments were performed on six gelatin phantoms on six different days. In one experiment, we also acquired a set of images with the imaging plane parallel to the z -axis at 250 Hz (Figure 3.5). These images were used to verify that the displacements were uniform in the region where the transverse images were obtained (i.e., plane wave assumption). In addition, the magnitudes of U_x and U_y in transverse images were compared to the magnitude of U_z over the range of 100 to 400 Hz. The RMS magnitude of U_x and U_y was less than 25% of U_z at all frequencies, indicating that

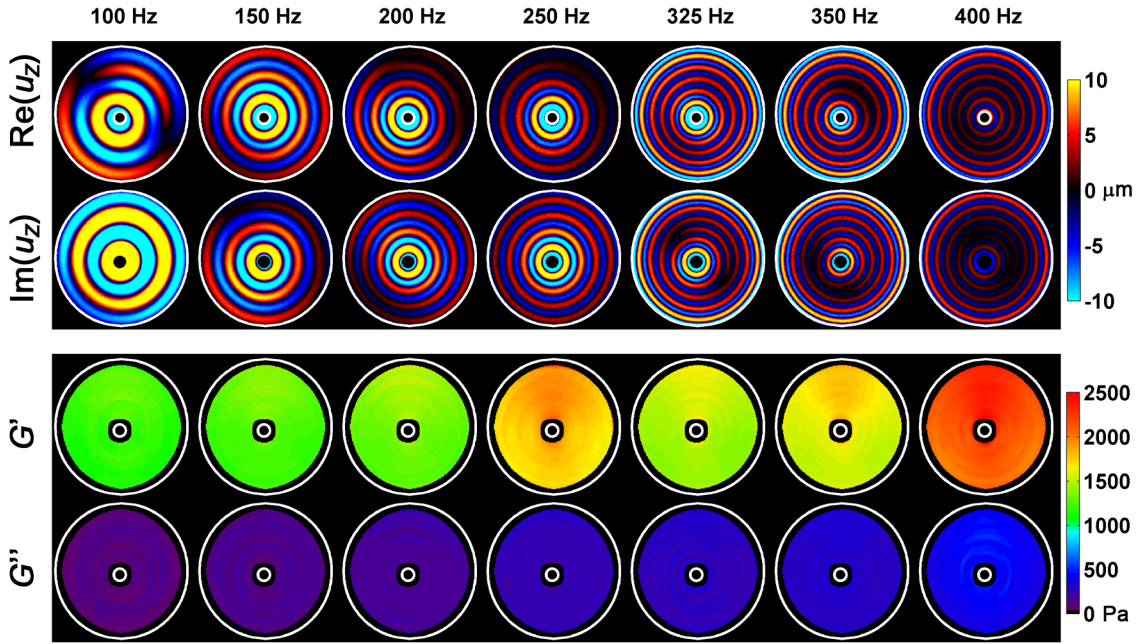


Figure 3.6: Displacement fields and viscoelastic parameters at each excitation frequency. (top) Real and imaginary components of the fundamental time harmonic of the through-plane displacement u_z are shown for slice 6 of 11. (bottom) Elastograms calculated from the displacement fields after spatially filtering with a 3D Gaussian kernel of $13 \times 13 \times 7$ voxels ($3.0 \times 3.0 \times 3.0 \text{ mm}^3$). The diameter of the gelatin container was 45 mm. Reproduced from Reference [119].

the dominant direction of displacement was along the z -axis. The real and imaginary parts of the fundamental time harmonic of the displacement field, $U_z(x, y, z, \omega)$, are shown in Figure 3.6 (rows 1 and 2) for one experiment at frequencies of 100 to 400 Hz. The data shown is not spatially filtered.

Direct least-squares inversion of the wave equation

Estimates of complex shear modulus obtained by direct inversion are shown in Figure 3.6. The modulus values at each pixel were spatially averaged to obtain mean values of G' and G'' for each frequency (Figure 3.8). The standard deviations of G' within the displacement field were less than 7% of the mean values; the standard deviations of G'' within the displacement field were less than 30% of the mean values.

Fit to the closed-form solution

Estimates of complex shear modulus obtained by direct inversion were verified by closed-form solution. MRE displacement data were evaluated along a line-path region of interest (ROI), passing through the center of the actuation rod (Figure 3.7a,c), and fitted to the closed-form solution of the boundary value problem in cylindrical coordinates. At frequencies below 250 Hz, shear waves propagated outward from the actuation rod and the shear wave amplitude decayed toward the outer radius of the cylinder (Figure 3.7b). At 250 Hz and above, there was also a noticeable inwardly propagating shear wave. This may have been caused by rigid body vibration of the gel cylinder container. In some cases this caused destructive interference of the inwardly and outwardly propagating wave in portions of the cylinder. However, it was possible to fit both wave fields simultaneously using a single estimate of G' and G'' (Figure 3.7d) by using the measured MRE displacements at both the inner and outer radii to determine the constants in Equations 3.5–3.6. In addition, using the best-fit coefficients for the closed-form solution, the maximum shear strain (dU_z/dr) at each frequency was also computed and averaged for frequencies between 100 and 400 Hz. The maximum shear strains were all less than 3% and generally occurred near the actuation rod. Estimates of G' and G'' for all six experiments using both direct inversion and the closed-form solution were averaged at each frequency (Figure 3.8b,c).

As noted in the methods section, we observed that the estimates of G' and G'' at a particular frequency were strongly influenced by the order in which frequencies were tested in each experiment. The test order was randomized for frequencies between 150 and 350 Hz, but was not randomized for 400 Hz (always the first frequency tested) and 100 Hz (usually the last frequency tested). We examined the effect of test order by performing two additional MRE experiments, each at a single frequency (150 Hz or 400 Hz), with repeated data acquisition over a six-hour period. The estimates of G' and G'' decreased monotonically in those experiments, reaching an equilibrium value after about four hours. As described in Appendix B, we found that this time-related decrease was likely caused by increasing temperature in the phantom over the course of each experiment and we developed a method to estimate the equilibrium values of G' and G'' for each experiment.

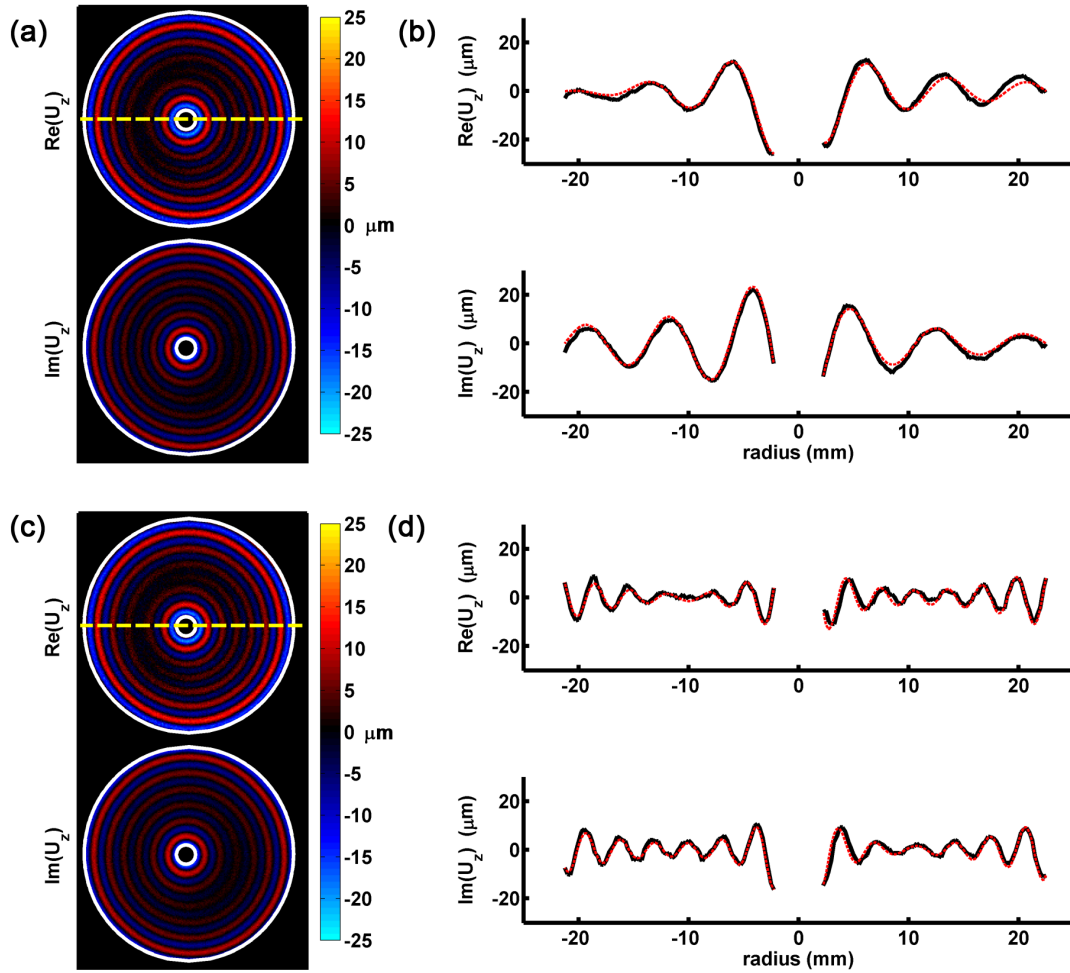


Figure 3.7: Real and imaginary parts of the complex displacement field $U_z(x, y)$ obtained by MRE at (a) 150 and (b) 350 Hz. The orientation of the line-path ROI used for comparison of MRE data with the closed-form solution is shown as a yellow dashed line. Real and imaginary parts of unfiltered MRE displacement data (solid line) and the predicted closed-form solution (dotted line) are compared at (b) 150 Hz and (d) 350 Hz. Reproduced from Reference [119].

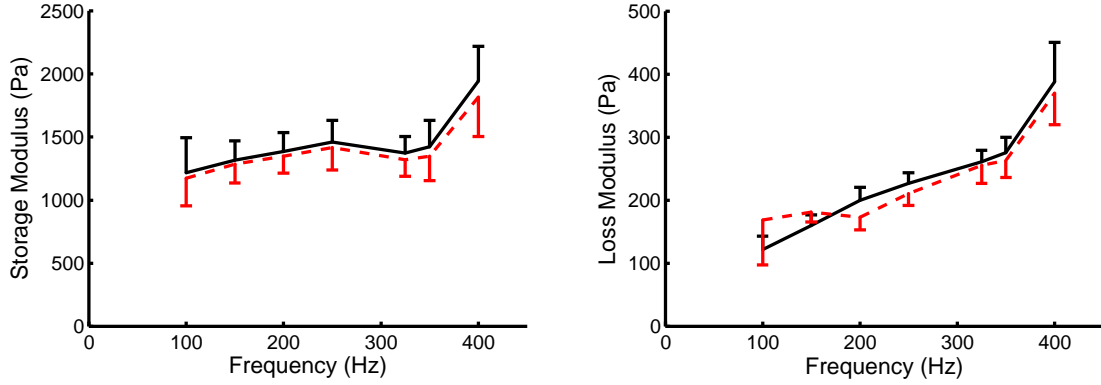


Figure 3.8: Viscoelastic shear moduli estimated from MRE displacement data via: direct inversion (solid line), and axisymmetric closed-form solution (dashed line). Error bars + or - 1 std. Adapted from Reference [119].

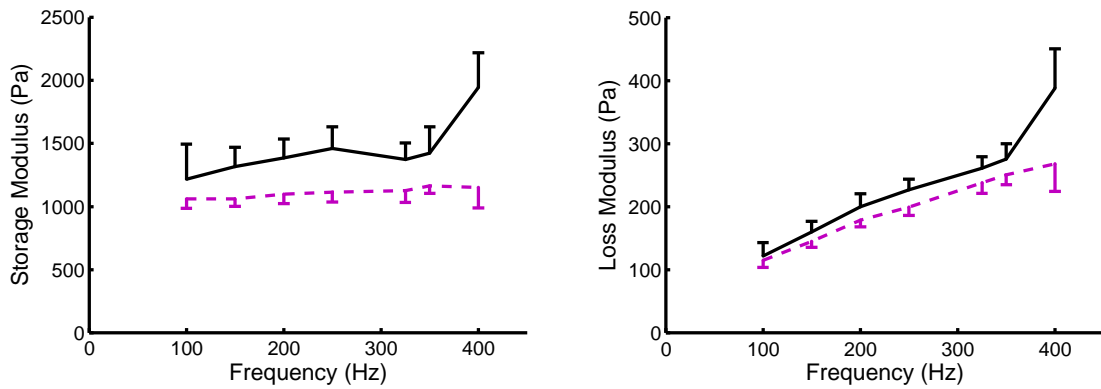


Figure 3.9: Viscoelastic shear moduli by direct inversion of MRE displacement data: as acquired (solid line), temperature corrected (dashed line). Error bars + or - 1 std. Adapted from Reference [119].

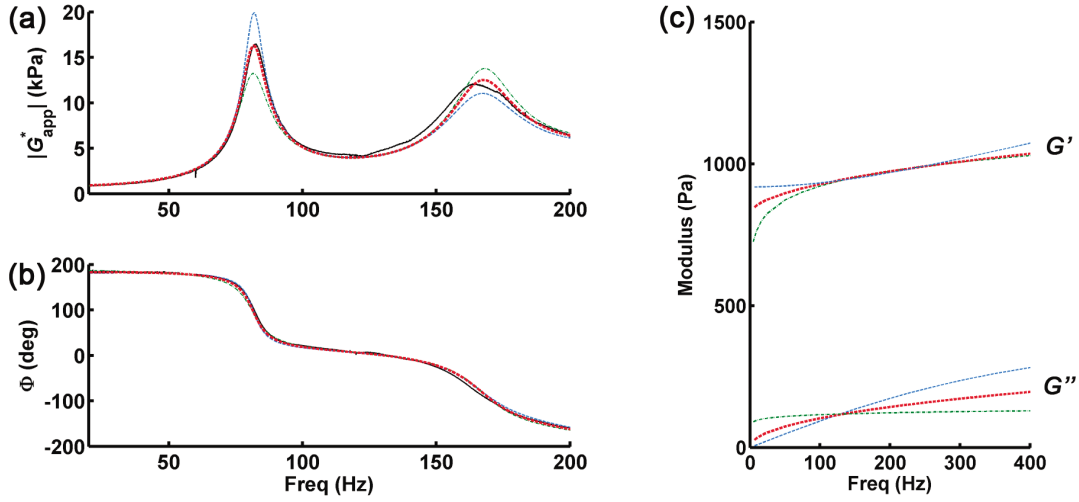


Figure 3.10: Typical results of DST. (a) Magnitude and (b) phase angle of apparent shear modulus. The phase angle changes rapidly at each shear wave peak. Experimental data (solid line) and best fits to standard linear solid (dotted line), fractional Zener (dashed line), and springpot (dash-dot line) models are shown. (c) Predicted G' and G'' from 0 to 400 Hz based on best-fit model parameters from test are shown. Reproduced from Reference [119].

A comparison of the measured values of G' and G'' and the estimated equilibrium values is shown in Figure 3.9. The equilibrium values of G' increased slowly from 1.06 ± 0.07 kPa (100 Hz) to 1.15 ± 0.16 kPa (400 Hz). G'' increased from 0.11 ± 0.01 kPa (100 Hz) to 0.27 ± 0.04 kPa (400 Hz). The loss factor increased from 0.11 to 0.23 over the same frequency range.

3.4.2 Estimates of viscoelasticity from DST data

For each MRE experiment, three samples from the same batch were tested by DST. During one experiment, two of the samples were damaged; hence data from a total of 16 samples were analyzed (Table 3.1). The presence of two shear wave peaks within the tested frequency range was consistent among all the samples.

Equations 3.9 and 3.13 were used to fit individual sets of experimental data to the three material models, as illustrated in Figure 3.10a,b. In this figure, the apparent shear modulus amplitude and phase are plotted because they clearly illustrate the

Table 3.1: DST sample properties ($n = 16$).

Property	Mean \pm 1 Std	Units
In-plane area, A	177 ± 6	mm^2
Thickness, h	5.5 ± 0.2	mm
Density, ρ	1.1	$\text{g}\cdot\text{cm}^{-3}$
First Resonance	83 ± 4	Hz
Second Resonance	167 ± 9	Hz

amplitude peaks at the frequencies where $|k| \approx \pi/h$ or $2\pi/h$. In general, we found that all three models could closely fit the data from DST tests. The primary difference in the model fits was the predicted magnitude of the first and second amplitude peaks. If the loss factor (G''/G') increases with frequency, the height of the second peak will be relatively smaller than the first.

The fractional Zener model was initially fit with the fractional exponent β fixed at values between 0.25 and 0.9. We found $\beta = 0.5$ to best-fit the height of both resonant peaks simultaneously (Figure 3.10). The values of τ and β tend to vary inversely if both parameters are fitted, therefore β was fixed (0.5) and best-fit values of the remaining three parameters were computed for each sample. In figure 3.10c, the predicted complex shear modulus for all three models are plotted as a function of frequency from 0 to 400 Hz for one sample. All models predict an increase in both G' and G'' with frequency.

The models differ primarily in their predictions of G' and G'' when extrapolated beyond the measurement range of 20 Hz to 200 Hz. The mean values of the parameters for each model (± 1 std) are shown in Table 3.2. We elected to use the fractional Zener model to compare DST predicted complex shear modulus with the estimates from MRE experiments because this model best approximated the height of both shear wave peaks in DST experiments.

Table 3.2: Rheological model best-fit parameters (DST data).

Model	Form	Mean \pm 1 Std
Springpot	$G^*(\omega) = \kappa(i\omega)^\alpha$	$\kappa = 557 \pm 46 \text{ Pa}\cdot\text{s}^{-\alpha}$ $\alpha = 0.08 \pm 0.14$
Zener	$G^*(\omega) = G_0 \frac{1+d(i\omega\tau_1)}{1+i\omega\tau_1}$	$G_0 = 918 \pm 68 \text{ Pa}$ $d = 1.79 \pm 0.21$ $\tau_1 = 0.24 \pm 0.14 \text{ ms}$
Fractional Zener	$G^*(\omega) = G_0 \frac{1+d(i\omega\tau)^\beta}{1+(i\omega\tau)^\beta}$	$G_0 = 820 \pm 57 \text{ Pa}$ $d = 6.75 \pm 1.64$ $\beta = 0.50 \text{ (fixed)}$ $\tau^\beta = (1.48 \pm 0.70) \cdot 10^{-6} \text{ s}^{0.5}$

3.4.3 Comparison of MRE and DST viscoelastic estimates

The values of complex shear moduli predicted by the individual fractional Zener model parameters were averaged for all DST tests and compared to the average MRE-predicted equilibrium values of G' and G'' , obtained by scaling the experimental values according to the method described in Appendix B. As shown in Figure 3.11, both MRE and DST estimates of the storage and loss moduli show a similar slow increase in G' and G'' with frequency. Above 200 Hz, DST predicted loss moduli are lower than MRE estimates. As shown in Figure 3.10c, predicted values of G'' are more sensitive to the choice of model than G' . For the fractional Zener model, increasing β will increase the predicted values of G'' at high frequencies, so there is greater variability in the predicted values of G'' in the Zener model, equivalent to the fractional Zener model with $\beta = 1.0$.

3.5 Discussion

We have estimated the complex shear modulus of a soft viscoelastic material over a broad range of frequencies. Previous validation studies have used MRE frequencies below 100 Hz [112, 36, 134, 34, 35, 123, 125], similar to frequencies used in MRE of human tissues. Other validation studies have performed MRE over a higher frequency ranges, e.g. Hamhaber et al. [54]: 125 to 400 Hz; Chan et al. [23]: 50 to 200 Hz;

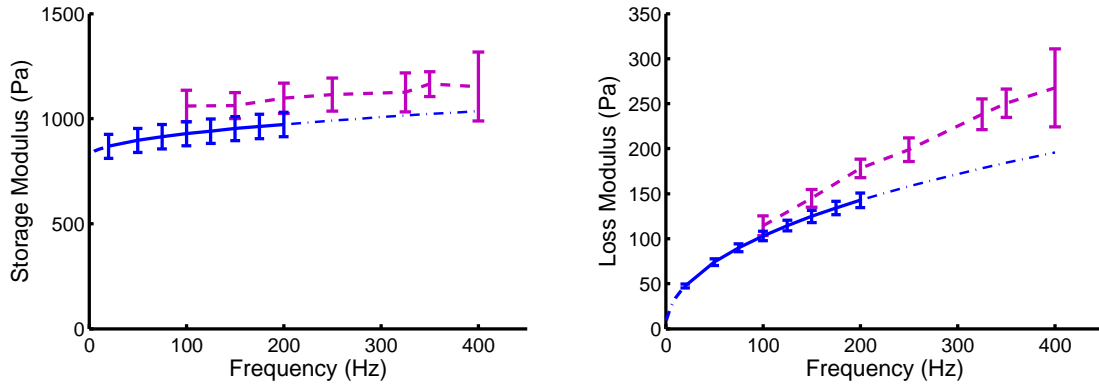


Figure 3.11: Comparison of viscoelastic shear moduli estimated from DST (solid line) and MRE (dashed line) (DST: $n = 16$; MRE: $n = 6$). A fractional Zener model was used for DST parameter extraction and to extrapolate behavior beyond measured frequency range (dash-dot line). MRE data shown were obtained by direct inversion and temperature corrected. Error bars ± 1 std. Adapted from Reference [119].

Atay et al. [6]: 200 to 800 Hz; but in these studies, mechanical tests were performed at frequencies below those used for MRE and only the elastic shear modulus was computed.

These are the first multi-frequency estimates of the viscoelastic shear modulus from direct mechanical tests and from MRE in an overlapping frequency range above 100 Hz. MRE data were analyzed by direct local inversion of the equation of motion and by globally fitting the displacement field to the closed-form solution of the axisymmetric boundary value problem. Both analyses yield similar estimates of viscoelasticity over the frequency range studied. DST was used to directly measure the storage and loss moduli. The frequency range of DST was extended by performing experiments in the shear wave regime and accounting for the induced inertial effect in our analysis.

Our novel DST method was validated. We checked that modulus values obtained from DST at driving high frequencies (>150 Hz), in the shear wave regime, were consistent with conventional DST at low driving frequencies (<50 Hz). The frequency of the shear wave peak and the sample thickness were used to estimate the storage modulus using Equation 3.12. Reference values of the viscoelastic shear modulus of the gelatin-glycerol blend we used were not available. Hence, samples of similar thickness were tested as the gelatin concentration was varied from 75% to 200% of the baseline value. A linear increase in the frequency of the shear wave peak was

observed. This is consistent with a previous report which notes a quadratic increase in modulus with increasing gelatin concentration [116]. We also tested different sample thicknesses at the baseline gelatin concentration. The frequency of the shear wave peak increased linearly with decreasing thickness, in agreement with Equation 3.12. As an additional consistency check during our study, we compared the apparent storage and loss moduli measured at 10 Hz in each sample with the model predicted values. At this low frequency, inertial effects are small. Model-predicted values using the fractional Zener model with $\beta = 0.5$ ($G' = 853 \pm 54$ Pa and $G'' = 34 \pm 2$ Pa) agreed closely with the measured values ($G' = 846 \pm 63$ Pa, $G'' = 39 \pm 34$ Pa).

When making quantitative estimates of the complex shear modulus using MRE, obtaining the displacement data is only the first in a series of data analysis steps. These steps include extraction of the fundamental time harmonic to separate the spatial and temporal variations in displacement, spatial filtering of displacement data, and calculation of G' and G'' on a point-wise basis or using a local fit to the wave equation. The end result of the data analysis is an elastogram (Figure 3.6; row 3,4), where the computed values of the storage and loss moduli are displayed spatially. Spatial averages may be calculated within an anatomical region of interest [150], in a region where the displacement amplitude is deemed sufficiently large [133], or where a goodness-of-fit parameter has been estimated [6, 29]. Since biological tissues may be heterogeneous, it is not always clear whether spatial variations in elastograms of G' and G'' are due to real differences in tissue properties or caused by limitations in the data collection or data analysis. In this study, we used a homogeneous material, so we do not expect G' and G'' to vary with location.

The normalized residual error (NRE) of the local fit of G' and G'' provides useful information about the reliability of the fitted values of G' and G'' at a particular location. In regions of the sample where displacement amplitude is small, NRE tends to be larger, reflecting the lower signal-to-noise values in those regions. Longer wavelengths relative to the field of view reduce the magnitude of the Laplacian and increase its sensitivity to noise in the displacement values.

In our study, the 3D Gaussian filtering of a single displacement component across a stack of images slightly reduced the NRE compared to using a single slice, because signal noise was smoothed across adjacent imaging planes. However, the in-plane filter

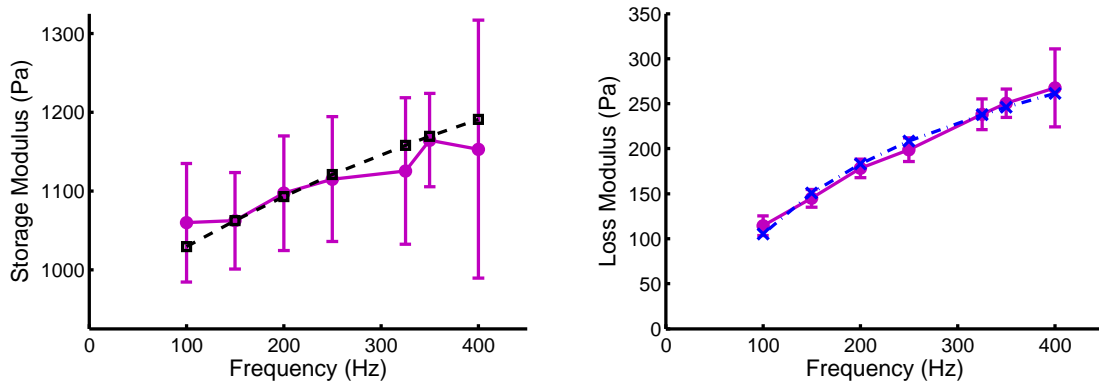


Figure 3.12: Causality of MRE estimated viscoelastic moduli was checked by a local, low-order Kramers-Kronig (K-K) approximation (Equation 3.14). K-K was used to predict the storage modulus from the measured loss modulus. Experimental measurements (solid lines, circles, error bars ± 1 std); predicted storage modulus (dashed line, squares); and piecewise linear fit of loss modulus (dash-dot line, crosses). Adapted from Reference [119].

parameters were the most important factor for decreasing NRE in regions of low signal amplitude. Increasing the Gaussian filter kernel size usually decreased NRE, but the Gaussian filter kernel should not span more than a wavelength. Furthermore, in possibly heterogeneous tissue samples, a large spatial filter kernel can span boundaries between different regions. Selection of a NRE threshold is specific to the experiment being performed and high NRE thresholds may be unavoidable. In general, using a larger NRE threshold implies a larger uncertainty in the estimated values of G' and G'' .

Agreement between MRE and DST results provides confirmation that local direct inversion of the equation of motion can estimate both the storage modulus and loss modulus of a viscoelastic material. The Kramers-Kronig (K-K) relation provides a way to check the required causal relationship between the storage and loss moduli. The exact K-K relation requires measurement of both G' and G'' as continuous functions of frequency over an infinite domain. This is practically infeasible. MRE data were obtained over a finite frequency domain and at discrete frequencies. To circumvent these limitations, local approximations of the K-K relation were employed [170]. We used a low-order, local approximation of the K-K relation to predict the storage

modulus from the measured loss modulus [170, 89]:

$$\frac{dG''(\omega)}{d(\ln \omega)} \approx \frac{2}{\pi} G'''(\omega). \quad (3.14)$$

This approximate K-K relation was applied to experimental data by piecewise-fitting the loss modulus to a series of first-order polynomials in $\ln \omega$,

$$G'''(\omega) = a_1 \ln \omega + a_0. \quad (3.15)$$

Equations 3.14 and 3.15 are combined and integrated to estimate the storage modulus as follows:

$$G'(\omega) - G'(\omega_0) = \frac{2}{\pi} \int_{\ln \omega_0}^{\ln \omega} [a_1 \ln \omega + a_0] d(\ln \omega) \quad (3.16)$$

$$= \left[\frac{a_1}{2} (\ln \omega)^2 + a_0 (\ln \omega) \right] \Big|_{\ln \omega_0}^{\ln \omega}. \quad (3.17)$$

This method gives a solution up to an arbitrary integration constant ω_0 , which was chosen to match the measured value of G' at one experimental frequency. The predicted storage modulus closely matches the measured (Figure 3.12). Hence, our data obeys the local, low-order K-K causality relation.

We found that our MRE phantoms reached temperature equilibrium three to four hours after the MRE experiments began. The initial rise in gelatin temperature appears to coincide with decreases in G' and G'' over the same time frame. One explanation for the time-dependent change in modulus is the sensitivity of the gelatin-glycerol blend to temperature. Our DST tests were conducted at room temperature, which was 22–24°C. DST samples are much smaller than the MRE phantom and will reach equilibrium with the surroundings faster. Since the DST samples experience significant mechanical work, including a brief pass through a type of mechanical resonance with the apparatus during the test, it is likely that the sample temperature increased above room temperature. When our MRE predicted storage and loss moduli are adjusted to equilibrium values (i.e., the values we would expect if the gel phantom had been in the scanner for 4–5 hours prior to MRE data collection), the values of G' and G'' in the overlapping frequency range show reasonable agreement and similar increase with frequency.

All of our measurements were made between 24 and 32 hours after mixing the gel ingredients. Frequency test order was randomized and modulus estimates were consistent with frequency after correcting for temperature change during the test, suggesting that sample mechanical behavior remains stable during the test period. Compared to gels made with gelatin and water only, gelatin-glycerol gels lose much less mass due to evaporation during storage, and can be stored for weeks without apparent degradation. We did not investigate whether mechanical properties were affected by extended storage.

The loss factor (G''/G') is used as a measure of a material's dissipative (viscous) behavior. Shear waves in a material with a large loss factor will attenuate over fewer wavelengths, making penetration of shear waves into a material more difficult. The loss factor for the gelatin-glycerol mixture was 0.12 to 0.20 over the range of 100 to 400 Hz, which is larger than values found for agar or agar-gelatin mixtures in rheologic measurements, but comparable to values reported for 15% gelatin-20% glycerol mixtures [125] at frequencies of 75 to 125 Hz or agar-gelatin blends at frequencies of 60 to 220 Hz [121]. Sack and co-workers [122, 133] have used an agar-glycerol-water mixture as a soft, visco-elastic tissue-mimicking phantom, but its properties have not been characterized with independent mechanical tests. Previous *in vivo* MRE studies suggest that the loss factor of brain tissue is in the range of 0.4 to 0.6 at 50 Hz [72, 142]. Thus, while the gelatin-glycerol mixture we used is viscoelastic, its behavior is still markedly more elastic than brain tissue.

The sensitivity of the viscoelastic properties of the gelatin-glycerol blend to temperature changes during testing is a limitation that should be considered when choosing a phantom material. Hall and co-workers [53] measured the elastic properties of agar and of gelatin crosslinked with formaldehyde to improve stability for ultrasound elastography. The cross-linking process takes several weeks to months to complete in the gelatin and the increase in melting temperature is accompanied by a large increase in elastic modulus, making fabrication of soft phantoms difficult. The authors also reported that agar gels exhibited non-linear elastic behavior. Ease of fabrication, cost and tunability are also important factors in choosing a phantom material, and in these areas the gelatin-glycerol blend has advantages. In future studies, the sensitivity to temperature changes can be mitigated by allowing the MRE phantoms to equilibrate

for several hours before use and should reduce time-dependent changes in the shear moduli that we observed and characterized.

3.6 Conclusions

The viscoelastic properties of a tissue-mimicking material were measured using a novel mechanical test technique (DST in the shear wave regime) and compared to properties obtained from MR elastography experiments. Storage and loss moduli were estimated from MRE displacement fields using (1) direct inversion and (2) by fitting a closed-form solution appropriate for our phantom geometry. The two methods gave similar values for both components of the shear moduli over the range of frequencies studied. We found that the trends in MRE storage and loss moduli were similar to those obtained from DST, though the mean values were about 10% higher in the overlapping frequency range. These results confirm that both storage and loss moduli of a moderately viscoelastic material can be reliably estimated using MRE. Confidence in these parameter estimates should be assessed by a “goodness-of-fit” measure such as normalized residual error. These findings can also provide a basis for assessing the quantitative accuracy of shear moduli obtained from MRE of soft tissues in vivo.

Chapter 4

Frequency-dependent Viscoelastic Parameters of Mouse Brain Tissue Estimated by MR Elastography

4.1 Overview

Viscoelastic properties of mouse brain tissue were estimated non-invasively, *in vivo*, using magnetic resonance elastography (MRE) at 4.7 T to measure the dispersive properties of induced shear waves. Key features of this study include (i) the development and application of a novel MR-compatible actuation system which transmits vibratory motion into the brain through an incisor bar, and (ii) the investigation of the mechanical properties of brain tissue over a 1200 Hz bandwidth from 600–1800 Hz. Displacement fields due to propagating shear waves were measured during continuous, harmonic excitation of the skull. This protocol enabled characterization of the true steady-state patterns of shear wave propagation. Analysis of displacement fields obtained at different frequencies indicates that the viscoelastic properties of mouse brain tissue depend strongly on frequency. The average storage modulus (G') increased from approximately 1.6 to 8 kPa over this range; average loss modulus (G'') increased from approximately 1 to 3 kPa. Both moduli were well approximated by a power-law relationship over this frequency range. MRE may be a valuable addition to studies of disease in murine models, and to pre-clinical evaluations of therapies. Quantitative measurements of the viscoelastic parameters of brain tissue at high frequencies are also valuable for modeling and simulation of traumatic brain injury.

The material presented in this chapter is published in *Physics in Medicine and Biology* (Clayton, Garbow, Bayly, 2011)³.

4.2 Introduction

4.2.1 Motivation: traumatic brain injury and other brain pathology

Traumatic brain injuries (TBI) are widespread in the United States and can result in permanent physical, cognitive, and/or behavioral impairment. Despite the prevalence and severity of TBI, the condition remains poorly understood and difficult to diagnose. Computer simulations of injury mechanics offer enormous potential for the study of TBI. Simulations can supplant experiments which are extremely difficult or expensive to perform, or cannot be performed for ethical reasons. However, computer models require accurate descriptions of tissue constitutive behavior and tissue connectivity (boundary conditions). Lacking such data, numerical predictions of brain deformation remain of questionable value. Quantifying tissue viscoelasticity is particularly important for understanding TBI, since rapid deformation of brain matter is a common feature among these injuries. MRE has also been suggested as a possible diagnostic or research tool for other brain disorders. Changes in material properties have been proposed as markers of tumor pathology [112] or progression of disease and degenerative processes, including Alzheimer's disease [123], multiple sclerosis [177], and aging [142].

³Author Contributions: E.H.C. designed, performed, analyzed experimental data, developed the inversion algorithm, and wrote the manuscript. J.R.G. and P.V.B. conceived the project. All authors reviewed the findings and discussed the manuscript.

4.2.2 Magnetic resonance elastography

Magnetic resonance elastography (MRE) is a non-invasive imaging technique for quantitative measurement of the mechanical properties of biological tissue [112]. To perform MRE the standard nuclear magnetic resonance imaging (MRI) method is modified to measure displacements due to wave propagation. The basic data in MR images are the radio-frequency (RF) signals produced by the precession of nuclear spins; ^1H is the predominant nucleus of interest in biological imaging. An MRE pulse sequence contains additional, temporally varying, “motion-sensitive” magnetic-field gradients which produce changes in spin-emitted RF signal phase that are proportional to spin displacement. These changes in spin phase can be measured throughout the imaging volume, producing displacement fields of high spatial resolution. Components of displacement in any direction can be measured by applying the motion-encoding gradients along that direction.

Several studies have explored the diagnostic value of MRE in the clinical setting. Interest has largely been driven by the empirical relationship between tissue health and stiffness. The mechanical properties of human tissues have been investigated using MRE. Plewes et al. [126] estimated isotropic elastic properties of breast tissue, whereas Sinkus et al. [151, 152] probed both isotropic and anisotropic viscoelastic properties. MRE has been applied to the human brain [81, 56], liver [5, 139, 178], heart [37, 143, 135], and prostate [70].

Fewer MRE studies have been conducted in animals. MRE has been applied to the canine prostate [26], porcine heart [79], and the murine and bovine eye [28, 31, 85]. In most animal studies, the primary research objective has been to demonstrate proof-of-concept for implementation as a clinical diagnostic tool. MRE studies in animal models have considerable value for monitoring disease staging and effects of therapy [33, 110, 123, 146, 179]. Of small animal models, the mouse is most frequently employed since it is low cost, small, relatively easy to handle, and its genomics are readily probed and manipulated.

Atay et al. [6] were the first to demonstrate feasibility of MR elastography in the mouse brain at 1200 Hz. Since then, others have performed studies at similar actuation frequencies (e.g., 1000, 1500 Hz) to investigate disease progression in the murine

brain and its effect on mechanical tissue properties [33, 110, 146]. The protocols of Atay et al. [6] and Murphy et al. [110] required an invasive procedure to affix the mechanical actuator to the mouse. Diguët et al. [33] and Schregel et al. [146] induced longitudinal waves into the skull using a mechanical transducer consisting of a coil and programmable pulse generator.

In this study, a novel, non-invasive, easy-to-use actuation setup was designed, built, and incorporated into animal studies. Mechanical vibrations were induced through an actuated incisor bar, allowing for efficient and well-tolerated studies. Experiments were performed at seven actuation frequencies, between 600 and 1800 Hz, to characterize the dispersive properties of mouse brain tissue. The analysis of experimental data was performed in three ways to cross check results: (i) using a single component of the displacement field (the most efficient approach); (ii) using all three components of the three-dimensional (3D) displacement field, and (iii) using the curl of the 3D displacement field (to eliminate longitudinal wave contributions).

4.3 Methods

4.3.1 Acquisition of spatiotemporal wave fields

Later work by Muthupillai and colleagues [113] describes in detail the physics of measuring harmonically-varying displacement fields with NMR spin-phase accumulation; the key points are summarized briefly in this section. Consider a single ^1H proton spin packet undergoing harmonic mechanical excitation and subjected to a sinusoidal, motion-encoding magnetic-field gradient, $G_i \sin(\omega_g t)$, parallel to an orthogonal reference coordinate i . The shift in NMR signal phase θ_i at position x_0, y_0, z_0 is governed by:

$$\theta_i(x_0, y_0, z_0, \Phi) = \gamma \int_0^\tau G_i \sin(\omega_g \tau) \cdot u_i \sin(\omega_d \tau + \Phi) d\tau. \quad (4.1)$$

G_i and ω_g are the motion-encoding gradient amplitude and oscillating frequency, respectively; $u_i(x_0, y_0, z_0)$ is the amplitude of the displacement component of the spin packet at this location and ω_d is the mechanical actuator driving frequency; γ is the gyromagnetic ratio of ^1H nuclei (protons). The synchronization delay, Φ ,

results in a temporal phase shift between the motion of a particular spin packet and the motion-encoding gradient. If multiple phase images are acquired, each with a different synchronization delay (corresponding to a fraction of the actuation period), a time history of spin phase is measured. Accordingly, each component of spin-packet motion, i.e., $u_i(x_0, y_0, z_0)$, can be imaged if the experiment is repeated three times and the motion-encoding magnetic-field gradients are aligned to a different axis of an orthogonal reference coordinate system each time.

The amplitude of each spin-packet displacement component, $u_i(x_0, y_0, z_0)$, can be determined directly from the amount of spin phase accrued, $\theta_i(x_0, y_0, z_0)$, by a scaling factor proportional to the amplitude, frequency, and duration of the applied motion-encoding gradient, $G_i \sin(\omega_g \tau)$. Sensitivity to motion is greatest when the mechanical actuation frequency, ω_d , and motion-encoding gradient frequency, ω_g , are equal ($\omega = \omega_d = \omega_g$) and the oscillating gradients are synchronized with the applied motion for an integer number of cycles, n . In this case, for sinusoidal encoding and excitation motion, the spin-phase displacement sensitivity can be calculated, in general, as, $\frac{u}{\theta} = \frac{\omega}{\gamma G \pi n}$.

4.3.2 Steady-state harmonic viscoelastic material response

The mechanical properties of biological tissue may be approximated by fitting measured displacement data to the equations governing wave propagation in an unbounded, isotropic, homogeneous, linear viscoelastic solid. Difficulty in this direct approach arises in selecting the appropriate viscoelastic model *a priori*. The correspondence principle allows the purely elastic equations of motion to be transformed into analogous viscoelastic equations via Laplace or Fourier transform [86, 41, 18]. As such, invoking the correspondence principle allows the real elastic moduli to be replaced with the corresponding complex viscoelastic moduli without requiring a specific rheological model.

The equations of dynamic equilibrium for an unbounded, isotropic, homogeneous, linear elastic solid are,

$$\mu u_{i,jj} + (\lambda + \mu) u_{j,ij} = \rho \ddot{u}_i, \quad (i, j = 1, 2, 3), \quad (4.2)$$

where λ and μ are the elastic (Lamé) parameters of the material; ρ is the material density (typically assumed to be 1000 kg/m³ for tissue) and u , and \ddot{u} are tissue displacement and acceleration, respectively.

In many soft tissues, the dilatational component of motion may be neglected without dramatically affecting estimates of distortional parameters [90]. The velocity of a pressure wave-front in a *nearly* incompressible material (e.g., biological tissue) is approximately 1500 m/s; at frequencies up to 2000 Hz (feasible for MRE) the wavelength is greater than 0.75 m, which greatly exceeds the field of view of most MRE experiments. The displacement amplitude of the pressure wave is often sufficiently small that its contribution is within the measurement noise floor. This is especially true if the primary mode of tissue excitation is shear [151], as is the case with our experiments. If the dilatational components of the displacement field in Equation 4.2 are neglected, the following simpler equations are obtained governing *shear wave* propagation in an elastic material [80]:

$$\mu u_{i,jj} = \rho \ddot{u}_i, \quad (i, j = 1, 2, 3). \quad (4.3)$$

If the imposed mechanical excitation is harmonic and steady-state, the material response at each location in the sample is,

$$u_k(x, y, z, t) = (U'_k + iU''_k) e^{i\omega t} + (U'_k - iU''_k) e^{-i\omega t}, \quad (k = 1, 2, 3), \quad (4.4)$$

where $U'_k = U'_k(x, y, z, \omega)$ and $U''_k = U''_k(x, y, z, \omega)$ are the real and imaginary coefficients of the complex exponential. Employing the correspondence principle, the real elastic parameter μ in Equation 4.3 is replaced by the complex shear modulus, $G^*(i\omega)$:

$$\mu \rightarrow G^*(i\omega) = G'(\omega) + iG''(\omega), \quad (4.5)$$

where G' is the storage modulus and G'' is the loss modulus. In general both components of the complex modulus depend on frequency. Substituting Equations 4.4-4.5 in to Equation 4.3, and separating the real and imaginary terms, leads to a coupled

set of real equations, recast in terms of the harmonic coefficients:

$$G'U'_{i,jj} - G''U''_{i,jj} = -\rho\omega^2U'_i \quad (4.6a)$$

$$G'U''_{i,jj} + G''U'_{i,jj} = -\rho\omega^2U''_i. \quad (4.6b)$$

In these equations displacements in orthogonal directions are uncoupled. For this reason, material property estimates can be made from acquisition of any single displacement component. In practice, the displacement component with the largest amplitude, and thus highest contrast-to-noise ratio, is used.

We illustrate the correspondence principle for the specific case of a Voigt material. Wave propagation in an unbounded homogeneous Voigt solid take the following Cartesian form [80]:

$$\mu u_{i,jj} + (\lambda + \mu)u_{j,ij} + \eta \dot{u}_{i,jj} + (\xi + \eta)\dot{u}_{j,ij} = \rho \ddot{u}_i. \quad (4.7)$$

Here ξ and η correspond to viscous “Lamé constants”, analogous to λ and μ , respectively. Substitution of the expressions for harmonic displacement (Equation 4.4) into Equation 4.7 leads to the relationships:

$$\mu U'_{i,jj} + (\lambda + \mu)U'_{j,ij} - \eta\omega U''_{i,jj} - (\xi + \eta)\omega U''_{j,ij} = -\rho\omega^2U'_i \quad (4.8a)$$

$$\mu U''_{i,jj} + (\lambda + \mu)U''_{j,ij} - \eta\omega U'_{i,jj} + (\xi + \eta)\omega U'_{j,ij} = -\rho\omega^2U''_i. \quad (4.8b)$$

If the dilatational contribution to the displacement field is neglected, Equation 4.8 are equivalent to Equation 4.6 above with storage modulus $G' = \mu$ and loss modulus $G'' = \eta\omega$.

In some extremely soft, porous tissues in which internal fluid flow occurs readily, the volumetric material distortion may not be negligible. In such cases, algorithms such as numerical Helmholtz decomposition may be employed to remove the contributions of longitudinal waves from experimental displacement fields [136, 151, 6]. Full Helmholtz decomposition is computationally expensive and may introduce additional artifacts [52]. Alternatively, when data are suspected of containing significant dilatational contributions, the curl of the 3D displacement field can be computed and fitted

to the corresponding equations of motion [151, 152]

$$\Gamma_i = \epsilon_{ijk} U_{j,k} , \quad (4.9)$$

where ϵ_{ijk} is the Levi-Civita permutation operator. Γ_i is then substituted into Equations 4.6. Note *the divergence of the curl of any vector field is always zero*, thus $\Gamma_{i,i} = 0$ by definition. Therefore,

$$G' \Gamma'_{i,jj} - G'' \Gamma''_{i,jj} = -\rho \omega^2 \Gamma'_i \quad (4.10a)$$

$$G' \Gamma''_{i,jj} + G'' \Gamma'_{i,jj} = -\rho \omega^2 \Gamma''_i. \quad (4.10b)$$

Equations 4.10 are free of dilatational terms and isolate the transverse components of the full equations of motion.

4.3.3 Data Acquisition

In total, 14 female mice (BALB/cAnNHsd, Harlan), aged 9 to 10 weeks-old, were studied. Mice were anesthetized with 1.5% isoflurane supplied by nose cone at 1.0 L/min oxygen for the duration of all experiments. Body temperature was maintained via a heating pad formed using re-circulating water bath. All procedures were approved by the institutional Animal Studies Committee in accordance with the NIH Guide on the Care and Use of Animals.

Elastography data were obtained in mouse brain at 4.7 T using an Agilent/Varian DirectDrive™ small-animal MR scanner. The scanner consists of an Oxford horizontal-bore magnet, Agilent/Magnex self-shielded gradient coils, and high-performance, gradient power amplifiers (International Electric Company) providing 60 G/cm peak magnetic-field gradient amplitude within 0.27 msec. NMR data were collected using an actively-decoupled transmit/receive coil pair [42]. A modified spin-echo NMR imaging pulse sequence was used to record spatiotemporal tissue motion as a shift in NMR signal phase (Figure 4.1). There are two noteworthy features of our pulse sequence: (i) sinusoidal motion-encoding magnetic-field gradients are used instead of trapezoidal-shaped gradients, and (ii) harmonic actuator motion is constant throughout the entire experiment to ensure true steady-state tissue response. Instead of

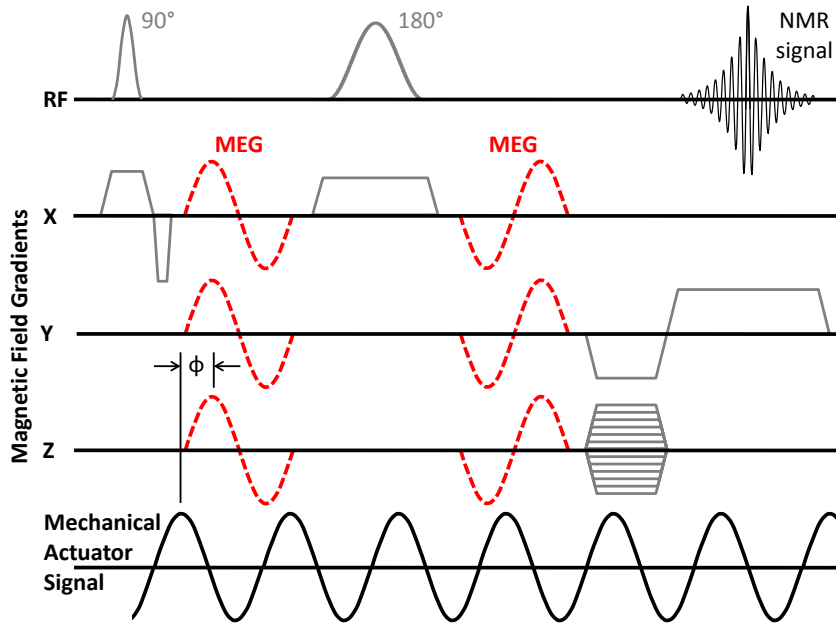


Figure 4.1: The modified spin echo magnetic resonance pulse sequence used for elastography data acquisition. In addition to RF and magnetic-field gradient events required to create a spin echo MRI, sinusoidal, motion-encoding gradients (MEG) are placed on each side of the 180° RF pulse. MEG events and the mechanical actuation signal may be temporally shifted by the parameter Φ . By varying the delay Φ temporal variations in the wave field are recorded. In this example, a 1-cycle MEG (dashed) is shown on each gradient channel. As a result, motion-encoded phase images are acquired with contrast proportional to displacements perpendicular to an oblique plane in the imaged body. Reproduced from Reference [29].

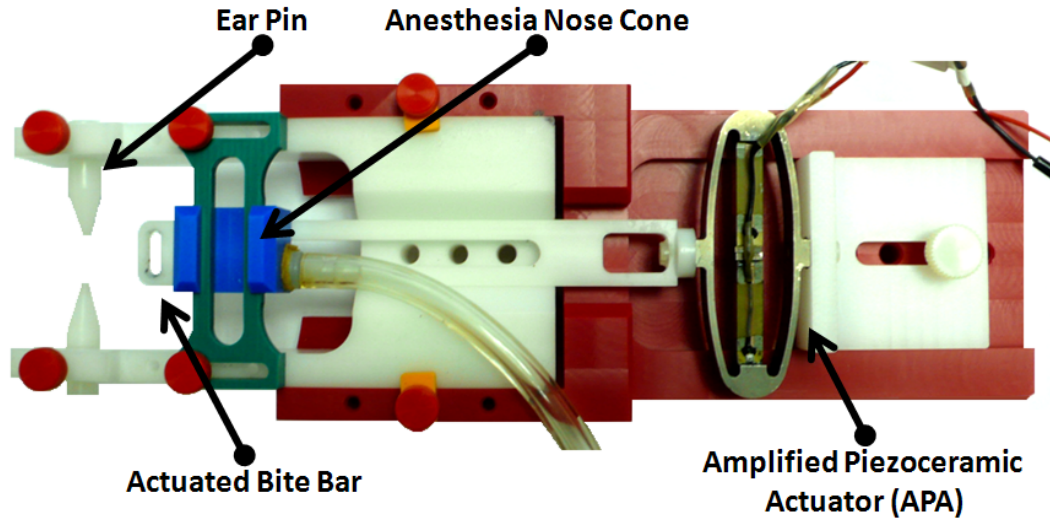


Figure 4.2: The custom-built stereotaxic mouse head holder used for elastography studies. The head of each mouse was secured between the ear bars and incisor bar. Light tension on the incisor bar ensures contact throughout the actuator stroke. An MR-compatible, amplified piezoceramic actuator drives the incisor bar harmonically, inducing mechanical vibration of the mouse skull along the rostral-caudal axis. Reproduced from Reference [29].

toggling the actuator on and off in synchronization with the scanner, the scanner is triggered by the actuator signal.

Propagating shear waves were induced in the brain with the custom-built head holder shown in Figure 4.2. Mechanical vibrations were generated by amplified-piezoceramic-actuator (APA150M-NM, Cedrat Technologies) and transmitted to the mouse via an incisor bar. The actuator was powered by a low-current, high-voltage amplifier (LA75C, Cedrat Technologies). A sinusoidal voltage waveform was supplied to the amplifier by a transistor-transistor logic (TTL) equipped function generator (FG-7002C, Ez Digital Co., Ltd.). The MR elastography imaging sequence was set to acquire one line of k -space with each TTL pulse, thereby synchronizing applied mechanical motion with MR motion-encoding gradients. Efficient data acquisition was facilitated by our novel head holder; with only three contact points, animal setup was simple and brief.

The entire mouse brain was imaged with 29 contiguous trans-axial slices in an interleaved manner. Experimental parameters were: resolution, $250 \times 250 \times 250 \mu\text{m}^3$;

TR/TE: 1000/27.5 msec; two excitations averaged for each line of k-space. Phase contrast was doubled by acquiring two sets of motion-encoded data, one each with positive and negative polarity motion-encoding gradients, which were subtracted from one another. Actuation frequencies ranged 600–1800 Hz at 200 Hz intervals. The temporal resolution of 600, 800, 1200, and 1800 Hz data was 8 points per actuation cycle. The temporal resolution of 1000, 1400, and 1600 Hz data was 4 points per actuation cycle.

Elastography data were acquired for six animals at each mechanical actuation frequency studied. For one animal, at each frequency, all three displacement components were acquired at temporal resolution of 4 points per actuation cycle. For all other data, only the through-image-plane component of motion $u_3(x, y, z, t)$ was recorded. A magnetic-field gradient amplitude of 15 G/cm was used throughout for motion encoding. TR/TE was held constant for all data; hence, the number of MR motion-encoding gradient cycles varied with the actuation frequency from 3 to 10. Acquiring a complete phase contrast image (i.e., positive and negative polarity images) required approximately 5.5 minutes per displacement component per time-point for each experiment conducted. Time under anesthesia varied according to test plan and ranged from 23–160 minutes (mean 108 min.). All mice survived imaging.

4.3.4 Data processing

Data post-processing was performed with programs written within the MATLAB (2009b, The MathWorks) computing environment. Motion-sensitized, phase-contrast images were obtained by complex division of positive- and negative-polarity phase images. Parasitic phase wrapping, if present, was removed via commercial software (Phase Vision Ltd.). Phase-contrast data were converted into displacements using the phase-displacement sensitivity relation previously discussed; taking into account the factor of two introduced through complex division of positive- and negative-polarity phase images. The fundamental harmonic coefficient $U'_k + iU''_k$ was extracted by Fourier transform along the time dimension. All data were smoothed with a circular, 4th-order Butterworth bandpass filter (in: 1.52 mm, out: 6.25 mm). A central difference scheme was used to approximate the Laplacian.

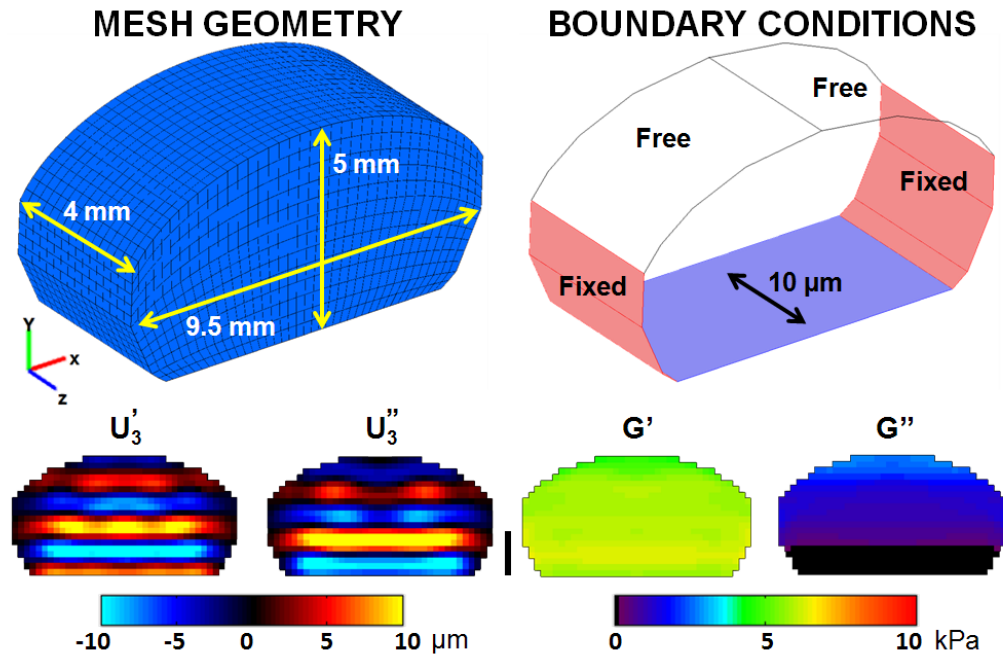


Figure 4.3: (Top) Finite element model geometry and imposed boundary conditions used for validation of the inversion techniques. (Bottom, left) Real and imaginary parts of the fundamental harmonic displacement component u_3 . (Bottom, right) Estimates of the viscoelastic parameters shown as functions of location in the central plane. (2 mm vertical scale bar shown.) Reproduced from Reference [29].

Inversion of Equations 4.6 and 4.10 was performed via regional least-squares fit. For each voxel, the complex modulus was found that minimized the squared error between the equilibrium equations and data in a kernel surrounding that voxel. The residual error of each fit, normalized by the variance in that kernel, was calculated to assess the “goodness-of-fit” of the linear isotropic homogeneous material model at that location. A normalized residual error (NRE) of zero indicates a perfect local fit; a residual of 1.0, a poor fit.

4.3.5 Inversion validation

The efficacy of our 1D and 3D inversion schemes were assessed with simulated data generated via finite element analysis (FEA). A numerical model (COMSOL Multiphysics 3.5a, Comsol Inc.) with similar geometry and material dynamics (i.e., attenuation and phase velocity) to those observed experimentally was developed

(Figure 4.3). A model discretized by 7,904 quadratic hexahedral elements (205,821 degrees-of-freedom) with a nominal side length $250 \mu\text{m}$ was used to simulate the response of a viscoelastic material to harmonic loading. Harmonic frequency analysis was performed at 600, 1200, and 1800 Hz by imposing a harmonic boundary displacement of $10 \mu\text{m}$ to the bottom surface of the brain model. The steady-state response was calculated and data were exported at $250 \times 250 \times 250 \mu\text{m}^3$ resolution, maintaining equivalence between FEA and experimental data.

4.4 Results

4.4.1 Inversion validation

Stability and accuracy of our inversion method was assessed using FEA displacement data. A parametric study was conducted to determine the optimal inversion kernel size $[N_x, N_y, N_z]$ and normalized residual error threshold (NRE). For 1D data inversion, the size of the fitting region was defined by $N_x = N_y = 3$; fits with high residual error ($\text{NRE} > 0.8$) were rejected. For 3D data inversion, the fitting region was defined by $N_x = N_y = 3$; estimates obtained from poor fits ($\text{NRE} > 0.8$) were rejected. Multiple slice planes were incorporated so that through-plane derivatives could be approximated for a single, central plane of data; hence $N_z = 1$ for all analysis. These same parameter values were used for processing of experimental data.

Results from the inversion of simulated data are shown in Table 4.1. The results in this table indicate that over the ranges of material parameters, frequencies, and wavelengths observed, errors of less than 1 kPa were typical. At all frequencies, 3D-curl inversion provided storage modulus estimates with greater spatial variation than other methods as evinced by its higher standard deviation. The storage modulus was consistently under-estimated, regardless of the actuation frequency or analysis scheme. All analysis schemes performed adequately.

Table 4.1: Validation of inversion methods. Estimates of viscoelastic parameters were obtained from simulated (FE) data for each of three inversion methods. (Poisson’s ratio of 0.49.)

Frequency (Hz)	Model	G' (kPa)			G'' (kPa)		
		Mean	Std	Error	Mean	Std	Error
600	FE Model Parameters	2.81	–	–	0.56	–	–
	1D Inversion	2.11	0.29	-0.70	0.47	0.16	-0.10
	3D Inversion	2.04	0.30	-0.78	0.42	0.12	-0.14
	3D-curl Inversion	2.18	0.42	-0.64	0.44	0.16	-0.13
1200	FE Model Parameters	6.04	–	–	1.21	–	–
	1D Inversion	5.88	0.36	-0.16	1.23	0.65	0.02
	3D Inversion	5.72	0.43	-0.32	1.09	0.49	-0.12
	3D-curl Inversion	5.89	0.83	-0.15	1.16	0.61	-0.04
1800	FE Model Parameters	14.09	–	–	2.82	–	–
	1D Inversion	13.49	0.84	-0.60	2.90	1.46	0.08
	3D Inversion	13.15	0.99	-0.95	2.52	1.14	-0.30
	3D-curl Inversion	13.55	1.90	-0.54	2.78	1.40	-0.03

4.4.2 Mouse brain elastography

Experimental data from the largest transaxial plane of mouse brain were processed using the previously discussed methodology. For 1D and 3D inversion, material estimates were made using three contiguous slice planes of data to accommodate numerical calculation of through-plane derivatives required for the Laplacian calculation. Only the through-plane motion component u_3 , was considered for 1D inversion. All three motion components were considered for 3D inversion. For 3D-curl inversion, five contiguous data slices were selected to accommodate numerical calculation of additional through-plane derivatives required for the curl operation. Data were parsed into three overlapping slice groups, each consisting of three image slices, and the curl was calculated for each group. The central slice from each group was retained such that three contiguous dilatation-free slice planes remained; these data were then run through the existing 3D inversion routine. Representative anatomical images, displacement fields, and estimates of material parameters are shown, for each frequency, in Figure 4.4.

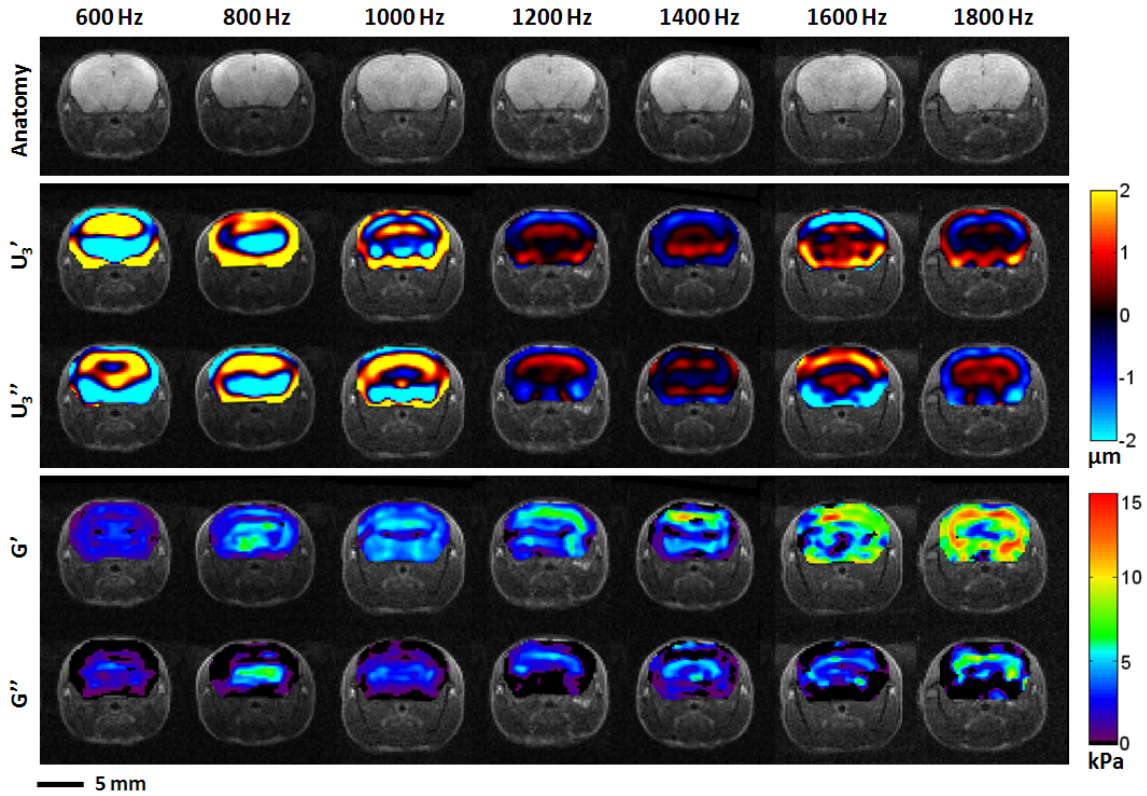


Figure 4.4: Example anatomical images, displacement fields and estimates of viscoelastic parameters for each excitation frequency. (Row 1): Magnitude images of a central (A/P) region of the brain; four contiguous slices $250 \mu\text{m}$ thick were averaged (1 mm total thickness). (Rows 2 & 3): External mechanical motion induces propagating waves within mouse brain tissue. The real, U'_3 , and imaginary, U''_3 , component of the fundamental harmonic of the through-plane displacement is shown for slice two of three contiguous slices used for inversion. (Rows 4 & 5): Elastograms (images of storage modulus, G' , and loss modulus, G'') calculated from the displacement fields of Rows 2 & 3. Reproduced from Reference [29].

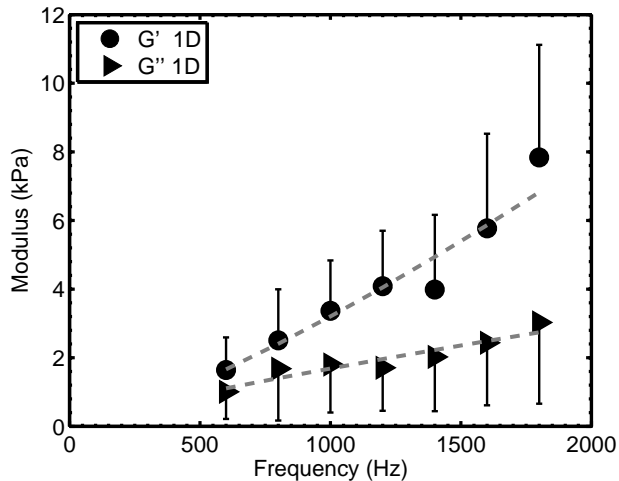


Figure 4.5: The frequency dependence of the average viscoelastic mechanical parameters estimated for the central region of the mouse brain ($n = 6$). Estimates were obtained by fitting a single motion component of the complex displacement harmonic to Equations 4.6. A power-law fit of the form $G(\omega) = \kappa\omega^\alpha$ is shown as a dashed line. (G' : $\kappa = 0.04 \times 10^{-3}$, $\alpha = 1.29$; G'' : $\kappa = 1.24 \times 10^{-3}$, $\alpha = 0.83$) Reproduced from Reference [29].

Root-mean-square displacement amplitudes of 1.0–2.5 μm are typical in these experiments; amplitudes are smaller at the highest experimental frequencies. The decrease in amplitude with frequency likely reflects the intrinsic frequency response characteristics of the actuator itself, as well as reduction in skull transmissibility and increased energy dissipation in brain tissue at these frequencies.

The 1D storage and loss moduli averaged over the entire image plane are reported for each frequency in Figure 4.5. Power-law models of the frequency dependence of storage and loss moduli, fitted independently to each material parameter, are also shown. At each frequency, all three components of the displacement field were acquired for one animal ($n = 1$), thereby permitting use of 3D inversion schemes. Analogous estimates of 3D storage and loss moduli averaged over the entire image plane are presented in Figure 4.6.

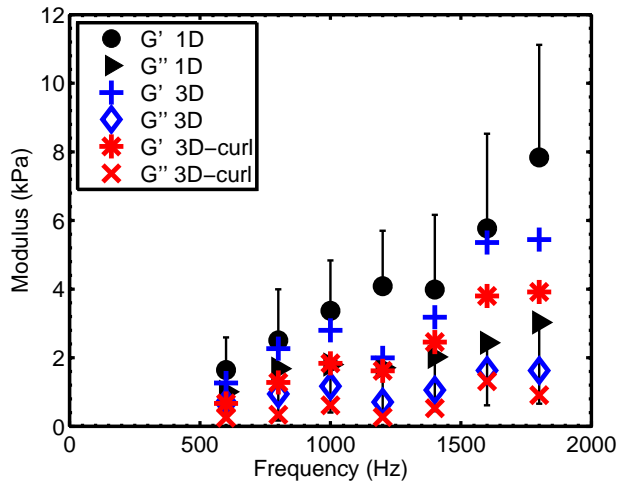


Figure 4.6: Comparison of the apparent dispersive properties of mouse brain tissue as obtained by three different inversion methods: “1D” - Equations 4.6, $i = 3$; “3D” - Equations 4.6, $i = 1, 2, 3$; “3D-curl” - Equations 4.10. Mechanical property estimates obtained from fitting 3D displacement fields to the viscoelastic equations of motion are within a standard deviation of estimates obtained by fitting only a single displacement component. (1D: $n = 6$; 3D: $n = 1$). Reproduced from Reference [29].

4.5 Discussion

MRE of the mouse brain was performed over a range of frequencies to illuminate the mechanical response of brain tissue. A novel, non-invasive, and versatile actuation system was developed and employed for data collection in vivo. The actuator maintained steady harmonic motion and the MR scanner was triggered by the actuation system, which allowed measurement of true steady-state parameter values. The viscoelastic properties of brain were determined over a broad range of driving frequencies, from 600–1800 Hz. The averaged material properties of central (A/P) mouse brain matter exhibit pronounced dispersive properties. Both the storage and loss moduli of brain tissue depend strongly on the frequency of excitation, which has important ramifications for numerical modeling of TBI.

Previous studies conducted in mouse brain have probed tissue properties at a single driving frequency, within the range of 1000–1500 Hz [33, 110, 6, 146], cf. Table 4.2. In the work by Atay et al. [6] and Murphy et al. [110], tissue was assumed to be purely elastic and only the apparent elastic shear modulus was estimated. In comparison,

Table 4.2: Material property estimates of *in vivo* mouse brain tissue measured by MRE.

Study	Frequency (Hz)	G'		G''		Study details		
		Mean (kPa)	Std (kPa)	Mean (kPa)	Std (kPa)	Strain	Age (wks)	Region
[6]	1200	13.8	1.49	–	–	C57BL/6	12–15	Central cortical gray matter
[33]	1000	7.36	0.50	3.33	0.80	C57BL/6	9–11	Central corpus callosum
[146]	1000	≈ 5.40	–	≈ 1.50	–	C57BL/6	–	Corpus callosum
[110]	1500	26.0	–	–	–	WT	70 \pm 2	Central cerebrum
		22.0	–	–	–	APP-PSI	82 \pm 2	Central cerebrum

viscoelastic material properties obtained in this study with those from other studies reveals variation within an order of magnitude. Differences in the material model assumed for inversion (elastic vs. viscoelastic) are clearly responsible for some discrepancies. Other discrepancies may reflect true differences in material properties due to age or analysis region. We do not advocate a specific material model to describe brain tissue viscoelasticity (i.e., a Voigt, Maxwell, springpot, or other analog); rather our results are presented simply as frequency-dependent complex moduli.

Causality of the estimated complex shear modulus was qualitatively assessed by the local Kramers-Kronig (K-K) approximation [129, 89]. The exact K-K relations are integral equations that relate the storage and loss moduli over an infinite range of frequencies. Local approximations to the K-K relations [129, 89, 118] have been used to demonstrate that a material obeys the principle of causality. The method described by Madsen et al. [89] was used to characterize the dispersion relationships observed in the current study. Estimates of loss modulus were fit to a polynomial function of $\log(\omega)$, which was then integrated to predict the dispersion of storage modulus. The increases in G' and G'' are consistent with the K-K requirements, but they are not

particularly well modeled by the local (approximate) K-K relationship. Nor are both moduli well described by a springpot (single complex power-law) model, as in the studies by Sack et al. [142] and Wuerfel et al. [177]. However, this is not surprising. The theoretical investigation by Pritz [129] explains the conditions under which the local K-K approximation is accurate. According to Pritz, if the moduli increase rapidly with frequency (as those of mouse brain tissue appear to) then qualitative, but not quantitative agreement with the local K-K relations is expected.

MR elastography has limitations. Material property estimates are subject to the constraints of imaging resolution, shear-wave wavelength, and the size of the anatomic feature of interest. It is desirable to have multiple waves in the anatomic region of interest to ensure the accuracy of numerical derivatives. The smaller the anatomic region of interest, the shorter the shear-wave wavelength required to maintain inversion accuracy. If the material properties are constant, increasing the excitation frequency would lead to a shorter wavelength. However, because of the dispersive properties of biologic tissue (the stiffening of material as actuation frequency increases) an increase in excitation frequency does not proportionally decrease wavelength.

MR imaging resolution determines the spatial-frequency fidelity of elastography data. The Nyquist criterion dictates the shortest wavelength (highest spatial-frequency) detectable in acquired wave-field images. The theoretical minimum wavelength is twice the voxel dimension. In other words, the maximum spatial frequency that can be resolved is half the spatial sampling frequency. In practice, approaching the Nyquist frequency can cause difficulty - oversampling of at least 10 times the Nyquist frequency is common in other engineering applications. Unfortunately, as the MR image resolution is increased (voxel size is decreased) the NMR signal amplitude is decreased. Imaging resolution was parametrically evaluated at the start of this study; we concluded that $(250 \times 250 \times 250 \mu\text{m}^3)$ cubic voxels represented the best compromise between imaging resolution, signal-to-noise ratio, and acquisition time at 4.7 T. This is, in fact, the smallest isotropic voxel size used to date in MRE of the mouse brain. Even at this resolution, the finite voxel size does introduce discretization error in the numerical calculations of the Laplacian of the displacement field, which remains a potential source of variation in our estimates of shear modulus.

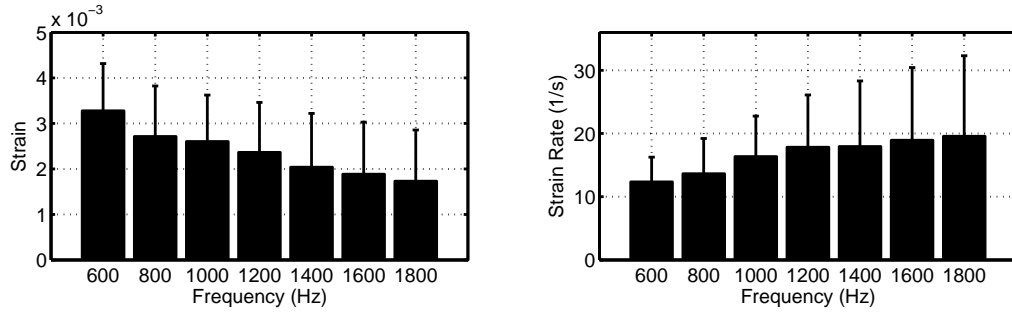


Figure 4.7: Average, root-mean-square (RMS) shear-strain $\frac{\partial u_3}{\partial y}$ amplitudes (left); and average, RMS shear-strain rates $\frac{\partial^2 u_3}{\partial t \partial y}$ observed in 1D experimental data (right); $n = 6$, standard deviations shown. Reproduced from Reference [29].

The majority of the parameter estimates in this study were obtained with a basic 1D inversion technique (analysis of a single component of displacement, obtained throughout the 3D image volume). Because only a single component is acquired, the analysis cannot include a direct Helmholtz decomposition to eliminate displacements due to longitudinal waves. However, estimates from the 1D inversion are very close to estimates obtained in a subset of the animals by a 3D inversion technique in which the curl of the displacement field is used to remove the contributions of longitudinal waves. Both of these estimates are also close to the estimates obtained by a 3D algorithm without the curl operation. While the 3D method using the curl is theoretically the most accurate, it is likely that the estimation of numerical derivatives introduces another source of error [151] (also, cf. analysis of FE data in Table 4.1). These results suggest that careful spatial filtering of the raw data to remove the low spatial-frequency (long wavelength) response, combined with the use of our novel actuator setup, which primarily induces shear waves in the brain, effectively mitigate the effects of longitudinal waves. The ability to use a 1D method is important, it reduces the acquisition time by a factor of three and obviates the need to estimate third-order derivatives (required for the curl-based algorithm) or perform computationally intensive Helmholtz decomposition routines [152].

In reality, brain tissue is not only viscoelastic - it is nonlinear, heterogeneous, and anisotropic. In this study, displacement-gradients, i.e. strains, were observed to be small, $\frac{\partial u_3}{\partial z} < \frac{\partial u_3}{\partial x} < \frac{\partial u_3}{\partial y} \ll 1$, so kinematic nonlinearity was negligible (Figure 4.7). In contrast, the frequency-dependent trend of calculated mechanical properties presented in Figures 4.5-4.6 indicates the importance of viscoelasticity. Mathematically, without

reference to the physics of a particular rheological model, the dispersive properties of mouse brain tissue over the frequencies investigated here are well characterized by a power-law relation of the form: $G(\omega) = \kappa\omega^\alpha$. Strain rates increased slightly with increasing actuation frequency (Figure 4.7), which may contribute to the apparent frequency dependence of G'' . It is important to note that mechanical properties reported here are the average values over the entire brain cross-section. The material properties of the brain are not homogeneous, but variations in properties at these length scales are not likely to be captured accurately. As such, anisotropy, which might be expected in the relatively small regions of white matter in the mouse brain, was not investigated. Direct mechanical tests on excised tissue [128] indicate that directional dependence is weak, even in white matter. Heterogeneity and anisotropy are logical targets for future studies.

4.6 Conclusions

The average dispersive properties of mouse brain tissue in a central region were estimated in vivo using MR elastography. Storage and loss moduli were estimated (i) in all animals by fitting the data to a single component of the equation of motion (1D analysis) and (ii) in a subset of animals by simultaneously fitting all three components of displacement data to the full 3D equation of motion. Results in all cases were similar, and reflected a strong dependence of complex shear modulus (both storage and loss components) on excitation frequency. MRE studies in small animals require motion at high frequencies to propagate shear waves with wavelengths short enough to resolve small features. However, tissue viscoelasticity limits both wavelength and wave penetration depth. Despite these limitations, MRE may provide valuable insight into studies of disease in murine models, and allow pre-clinical evaluations of therapies. Measurements of the viscoelastic parameters of brain tissue at high frequencies are also valuable for modeling and simulation of traumatic brain injury, since TBI results from short-duration events, e.g., blast and impact. The comparison of results from both simulation and experiment provides valuable insight into the quantitative accuracy of MRE.

Chapter 5

Transmission, Attenuation, and Reflection of Shear Waves in the Human Brain

5.1 Overview

Traumatic brain injuries (TBI) are caused by acceleration of the skull or exposure to explosive blast, but the processes by which mechanical loads lead to neurological injury remain poorly understood. We adapted motion-sensitive magnetic resonance imaging methods to measure the motion of the human brain *in vivo* as the skull was exposed to harmonic pressure excitation (45, 60, 80 Hz). We analyzed displacement fields to quantify the transmission, attenuation, and reflection of distortional (shear) waves as well as viscoelastic material properties. The results suggest that the internal membranes such as the falx cerebri and the tentorium cerebelli play a key role in reflecting and focusing shear waves within the brain. The skull acts as a low-pass filter over the range of frequencies studied, with transmissibility of pressure waves through the skull decreasing and shear wave attenuation increasing with increasing frequency. The skull and brain function mechanically as an integral structure that insulates internal anatomic features; these results are valuable for building and validating mathematical models of this complex and important structural system.

The material presented in this chapter is currently in review (Clayton, Genin, Bayly, 2012)⁴.

5.2 Introduction

Traumatic brain injury (TBI) can result from blunt force trauma, rapid inertial loading, or extracranial pressure (i.e., explosive blast). Much of the pathway between mechanical insult and neurological injury remains unclear, in part because data on the mechanical response of the brain are difficult to acquire *in vivo*. Diffuse axonal injury, in which neural axons stressed beyond limit initiate a biochemical cascade culminating in axon destruction, is believed to be a direct consequence of this mechanical response [161, 162, 154]. Recent developments in magnetic resonance imaging (MRI) have uncovered a critical mechanical role of brain-skull attachment in determining the locations of high strains when the skull is accelerated [15, 140, 39, 1].

The ability to simulate TBI computationally is quite advanced [75, 61, 165, 117] but has historically outpaced the data available for validation. The range of data available begins with a study by Holbourn [63], who investigated strains in gel-filled molds of the human cranium subjected to angular accelerations. Holbourn postulated that injury locations correlate with regions where high shear strain was observed in his gelatin brain models. Others [93, 101] have studied more complex gel-filled head models. Hardy et al. [57, 58] advanced this type of analysis to the heads of human cadavers, where internal brain motion was measured by tracking implanted neutral-buoyancy markers using high-speed bi-planar X-ray imaging. These studies represented significant progress in the study of brain injury biomechanics. However, gels and cadaver heads differ substantially from the human brain *in vivo*, and the spatial resolution of implanted markers falls far short of capabilities of imaging methods such as MRI.

The use of MRI to characterize wave propagation, especially as related to TBI, is an emerging application [99, 98]. In the current study, we implement a motion-sensitive MRI scheme to map the structural response of the brain-skull system to

⁴E.H.C. designed and performed experiments, analyzed data, developed the inversion algorithm, and wrote the manuscript. All authors discussed the findings and commented on the manuscript at all stages. P.V.B. and G.M.G. conceived the study.

measured extracranial pressure oscillations. We present here MRI data that suggest that brain-skull attachments as well as the internal meninges (falx and tentorium) strongly affect patterns of wave propagation in the brain. We also introduce a novel viscoelastic material property reconstruction scheme and apply it to these data. The transmissibility of the skull to oscillatory pressure loading, and the attenuation of inwardly propagating shear waves are quantified. The findings presented here will be very useful for the validation of numerical models intended to simulate head trauma.

5.3 Materials and Methods

5.3.1 Motion-sensitive magnetic resonance imaging

Images of tissue motion can be recorded using a standard clinical MRI scanner equipped with a motion-sensitive imaging pulse sequence and an MR-compatible actuator to produce tissue motion [112]. The NMR signal used for clinical imaging is produced by precession of ^1H proton spin packets in a strong magnetic-field (commonly 1.5–3 T). Spin precession (Larmor) frequency is determined by the magnetic-field amplitude. In the presence of a spatially varying magnetic-field gradient, a spin packet displaced to a location with higher magnetic-field strength will precess faster. Over time the displaced spin will acquire additional phase relative to a spin in the original configuration. Applying harmonically oscillating magnetic-field gradients into an imaging sequence allows harmonic spin displacement to be recorded as a phase shift in the NMR signal. With this technique, motion sensitivity to displacements as small as 100 nm have been reported [112]. This type of motion-sensitive MRI, known as MR elastography, has been employed to image propagating shear waves, and from the shear wave propagation speed, to infer the mechanical properties of tissue *in vivo* [112, 82, 149, 21, 90].

The physical framework describing the measurement of spatiotemporal displacement fields with motion-sensitive MRI is described in detail by Muthupillai and colleagues [113]. Here we briefly review the mathematics. Consider a single ^1H proton spin packet originally at position $\bar{\mathbf{r}}_0 = x_0\bar{\mathbf{e}}_1 + y_0\bar{\mathbf{e}}_2 + z_0\bar{\mathbf{e}}_3$, undergoing harmonic motion. Its vector

displacement $\bar{\mathbf{u}}(\bar{\mathbf{r}}_0, t)$ can be expressed in complex exponential form as:

$$\bar{\mathbf{u}}(\bar{\mathbf{r}}_0, t) = \bar{\mathbf{U}}(\bar{\mathbf{r}}_0)e^{i(\omega t + \psi(\bar{\mathbf{r}}_0) + \Phi)} + \text{complex conjugate.} \quad (5.1)$$

The displacement coefficient vector $\bar{\mathbf{U}}(\bar{\mathbf{r}}_0)$ can also be expressed in terms of its Cartesian components: $\bar{\mathbf{U}}(\bar{\mathbf{r}}_0) = U_k(\bar{\mathbf{r}}_0) \cdot \bar{\mathbf{e}}_k$. To measure this motion, a time varying motion-encoding gradient $\bar{\mathbf{G}}(t) = G_k(t) \cdot \bar{\mathbf{e}}_k$ is imposed. Accrual of NMR signal phase θ is governed in general by

$$\bar{\theta} = \gamma \int_0^T \bar{\mathbf{G}}(t) \cdot \bar{\mathbf{u}}(\bar{\mathbf{r}}_0, t) dt, \quad (5.2)$$

where γ is the gyromagnetic ratio of ^1H nucleus. The duration of the applied gradient is $T = 2\pi n/\omega$, which is dependent on the actuator frequency ω (rad/sec) and the number of motion encoding cycles n chosen. In practice, one component of the gradient field is imposed at a time, yielding a corresponding phase image:

$$\theta_k(\bar{\mathbf{r}}_0, \Phi) = \gamma U_k(\bar{\mathbf{r}}_0) e^{i(\psi(\bar{\mathbf{r}}_0) + \Phi)} \int_0^T G_k(t) e^{i\omega t} dt + \text{complex conjugate.} \quad (5.3)$$

The amplitude and phase, $U_k(\bar{\mathbf{r}}_0) \exp[i(\psi(\bar{\mathbf{r}}_0) + \Phi)]$, of each voxel imaged can be determined directly from spin phase θ_k accrued, since $G_k(t)$ is prescribed. The synchronization delay Φ is a temporal phase shift between the applied motion and the motion-encoding gradient. If multiple images are acquired, each with a different synchronization delay (corresponding to a fraction of the actuation period), a time history of spin phase is measured, cf. Figure 5.1.

In our experiments the components of $G_k(t)$ took the following form:

$$G_k(t) = \begin{cases} -|G|, & \text{for } \frac{2\pi(n-1)}{\omega} \leq t \leq \frac{\pi(4n-3)}{2\omega} \\ +|G|, & \text{for } \frac{\pi(4n-3)}{2\omega} \leq t \leq \frac{\pi(4n-1)}{2\omega} \\ -|G|, & \text{for } \frac{\pi(4n-1)}{2\omega} \leq t \leq \frac{2\pi n}{\omega}. \end{cases} \quad (5.4)$$

Full displacement vector fields may be acquired by repeating the experiment with the motion-encoding magnetic-field gradients aligned to each axis of an orthogonal coordinate system.

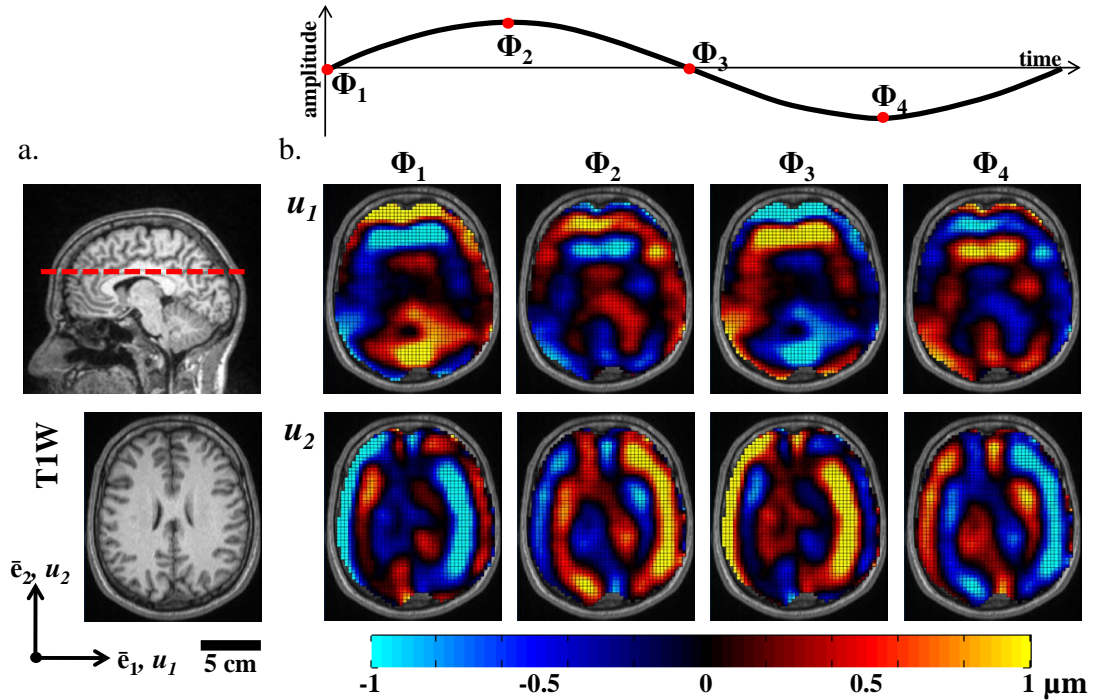


Figure 5.1: (a) High resolution anatomic images of the brain slice in which displacement data were recorded highlight anatomic structures and boundaries (e.g., gray and white matter, lateral ventricles, etc.). Displacement data were acquired on approximately transverse slice planes through the superior corpus callosum. (b) In-plane spatiotemporal displacement Fields were used to calculate the through-plane component of distortion Γ . Transmission, attenuation, and reflection of distortion within the living human cranium were analyzed in this study. (S014, 45Hz)

5.3.2 Measurement procedure and equipment

A motion-sensitized gradient-recalled echo (GRE) MRI pulse sequence (Figure 5.2) was used to acquire data in six healthy male subjects, aged 19-42 years-old (mean: 28.7 yr), at actuation frequencies of 45, 60, and 80 Hz. In each subject data were acquired on single transverse-oblique slice through the top of the corpus callosum (Figure 5.1). Imaging parameters were: repetition time (TR): 111.1-137.5 ms, echo time (TE): 27.5 ms, flip angle: 25° , resolution: $3 \times 3 \times 3 \text{ mm}^3$. The imaging procedure was repeated three times with different motion-encoding gradient orientations to record 3D displacement vector fields relative to the oblique imaging plane. The Human Research Protection Office Internal Review Board of Washington University approved the experimental protocol.

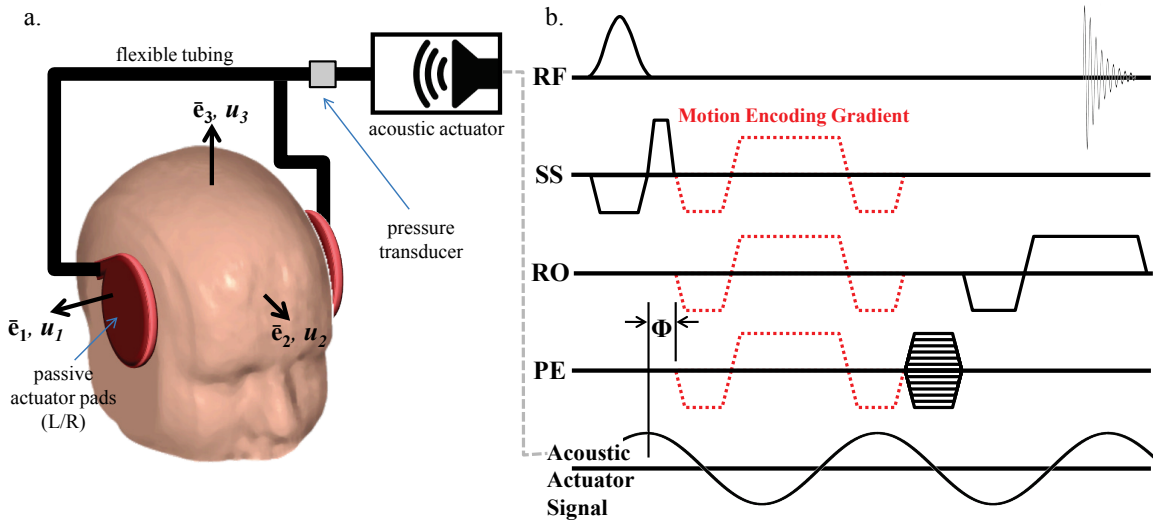


Figure 5.2: (a) Schematic diagram of the experimental apparatus for inducing shear waves in the brain by extracranial pressure loading. (b) The specialized gradient-recalled echo (GRE) magnetic resonance imaging pulse sequence used for data acquisition. In addition to the standard radio frequency (RF) pulses and orthogonal magnetic-field gradient orientations (SS: slice select, RO: readout, PE: phase encode) required to create the GRE MR image, a trapezoidal motion-encoding gradient is included.

The absolute peak motion-encoding gradient amplitude $|G|$ was nominally 25 mT/m for all test frequencies, and spin phase was accrued over a single gradient cycle n (Equation 5.4). The actuation system was configured to transmit a 4, 6, and 8 cycle acoustic pressure-wave train at 45, 60 and 80 Hz, respectively. Actuation was initiated by a TTL pulse generated by the scanner and synchronized with each NMR excitation. MRI motion-encoding gradients were configured to run at the same frequency as the actuator for each experiment. All data was acquired with a temporal resolution of four points per actuation cycle to satisfy the Nyquist-Shannon sampling criterion. Phase-to-displacement conversion factors of 5.63 $\mu\text{m}/\text{rad}$ (45 Hz), 7.66 $\mu\text{m}/\text{rad}$ (60 Hz), and 10.6 $\mu\text{m}/\text{rad}$ (80 Hz) were calculated by numerical integration of Equations 5.3 and 5.4, taking into consideration actual gradient performance specifications. The total scan time to acquire 2D displacement field data in each subject was approximately fourteen minutes per actuation frequency.

Volunteers were imaged in a 1.5 T MAGNETOM Avanto (Siemens) whole-body clinical scanner equipped with a phased-array head coil. Harmonic motion was induced

in the brain via extracranial pressure generated by an acoustic actuation system (ResoundantTM, Resoundant Inc., Rochester, MN). The system was modified with two equal lengths of flexible vinyl tubing and a T-fitting so that a single active driver could power two passive drivers with equal amplitude and phase. Each passive actuator pad was positioned on the side of the head near the left and right pterion bone and affixed with an elastic bandage, cf. Figure 5.2. The head of each subject was snugly secured within the imaging coil using foam inserts to prevent subject movement during scans. Imposed acoustic pressure loads were measured with a PCB Piezotronics (103B01) dynamic pressure sensor connected to a variable gain voltage amplifier PCB Piezotronics (494A). The pressure signal, in the form of analog voltage, was digitized and stored on a laptop PC using a National Instruments shielded connector block (SCB-68) and 12-bit A/D converter (DAQCard-6062E).

Raw MRI data (k-space) were analyzed in MATLAB (The MathWorks, Inc.). Motion encoded MR data were obtained using a switched-polarity acquisition scheme to remove systematic phase errors and enhance displacement contrast [90]. After applying the 2D inverse Fourier transform to the raw (k-space) data, phase-contrast images were obtained by complex division of positive and negative polarity images and displacement fields with sensitivity factors described above.

Displacement data were spatiotemporally filtered to remove higher-order harmonics and noise. First, the fundamental complex time harmonic of the displacement field was extracted by Fourier transform along the time dimension. Then, the fundamental harmonic was spatially filtered with a Gaussian spatial filter (kernel: 11 x 11, std: 0.80). Finally, filtered displacement fields were reconstituted in the time domain via inverse Fourier transform, using only the fundamental time harmonic.

5.3.3 Analysis of the distortional component of motion

Harmonic oscillation of the skull leads to propagation of waves of distortion and dilatation through brain parenchyma [82, 90, 56, 49]. Analysis of raw displacement data is challenging because both types of wave motion are intrinsically coupled through loading and boundary conditions [176], but the waves speeds differ by several orders of magnitude.

The equations governing wave motion in an extended linear elastic, isotropic, homogeneous material are

$$\rho \frac{\partial^2 u_k}{\partial t^2} = \mu \nabla^2 u_k + (\lambda + \mu) \frac{\partial}{\partial x_k} (\nabla \cdot \bar{\mathbf{u}}), \quad (5.5)$$

where λ and μ are the Lamé constants and ρ is the material density [80]. The dilatational (irrotational) and distortional (equivoluminal, or shear) deformation modes can be decoupled by applying the divergence and curl to Equation 5.5

$$\frac{\partial^2}{\partial t^2} (\nabla \cdot \bar{\mathbf{u}}) = \frac{\lambda + 2\mu}{\rho} \nabla^2 (\nabla \cdot \bar{\mathbf{u}}), \quad (5.6a)$$

$$\frac{\partial^2}{\partial t^2} (\nabla \times \bar{\mathbf{u}}) = \frac{\mu}{\rho} \nabla^2 (\nabla \times \bar{\mathbf{u}}), \quad (5.6b)$$

respectively [80, 7, 176]. Use of the decoupled equations of motion provides a way to isolate the dilatational wave phase velocity $c_1 = \sqrt{(\lambda + 2\mu)/\rho}$ from the shear wave phase velocity $c_2 = \sqrt{\mu/\rho}$.

We define

$$\Gamma = \frac{1}{2} \left(\frac{\partial u_2}{\partial x_1} - \frac{\partial u_1}{\partial x_2} \right) \quad (5.7)$$

as the distortional wave component normal to the image plane, which is calculated from the in-plane displacements. The root-mean-squared (RMS) value of the distortion Γ was computed and normalized by the RMS applied pressure load according to the following expression:

$$\frac{\Gamma}{P} = \sqrt{\frac{1}{T} \int_0^T [\Gamma(t)]^2 dt} / \sqrt{\frac{1}{T} \int_0^T [P(t)]^2 dt}. \quad (5.8)$$

These data - distortion normalized by applied pressure - were analyzed to quantify the frequency-dependent transmissibility, attenuation, and reflection of shear waves in the living human brain.

Transmission of acoustic pressure through the skull and into the brain was assessed by the pressure-normalized distortion averaged over a 1.5 cm wide region immediately interior to the skull.

Attenuation of shear waves in the brain was quantified by the decay in amplitude as a function of distance from the skull. Regions of interest were obtained by applying a series of concentric elliptical masks to the shear wave field. These masks were created by iteratively eroding the outer boundary of the field inward. Two consecutive masks were subtracted to produce an annular elliptical mask with a thickness of approximately 1 voxel (i.e., 3 mm). The distortion was averaged for each region of interest, and these average values plotted as a function of distance from the brain-skull boundary. Exponential attenuation of shear waves was observed in the brain and is consistent with expected viscoelastic behavior.

Wave Normal Extraction and Qualitative Energy Analysis

Reflection of shear waves in the brain was assessed from vector fields of amplitude-weighted average propagation direction. In principle, a scalar field $\Gamma(\bar{\mathbf{r}}_0, t)$ that is harmonic in time and periodic in space may be represented as a double Fourier series

$$\Gamma(\bar{\mathbf{r}}_0, t) = e^{i\omega t} \sum_{m=-\infty}^{\infty} \sum_{n=-\infty}^{\infty} a_{mn} e^{i(k_m \cdot x_0 + k_n \cdot y_0)} + \text{complex conjugate.} \quad (5.9)$$

The 2D wavenumber $\bar{\mathbf{k}}_{mn} = k_m \bar{\mathbf{e}}_1 + k_n \bar{\mathbf{e}}_2$ describes the wave length and propagation direction. Here the angle of propagation θ_{mn} of each plane wave component is defined as the four-quadrant inverse tangent of k_n/k_m .

Contributions of plane shear waves along a particular direction θ_p may be obtained by applying a directional spatial filter to the distortional wave field as follows,

$$\Gamma_p(\bar{\mathbf{r}}_0, t) = e^{i\omega t} \sum_{m=-\infty}^{\infty} \sum_{n=-\infty}^{\infty} a_{mn} \cdot f_p(\theta_{mn}) e^{i(k_m \cdot x_0 + k_n \cdot y_0)} + \text{complex conjugate.} \quad (5.10)$$

In this work, we apply a spatial directional filter is defined by,

$$f_p(\theta_{mn}) = \begin{cases} \cos^2(\theta_{mn} - \theta_p), & \|\theta_{mn} - \theta_p\| \leq \pi/8 \\ 0, & \|\theta_{mn} - \theta_p\| > \pi/8 \end{cases} \quad (5.11)$$

to plane wave components propagating along sixteen directions; $\theta_p = p\pi/8$, for ($p = 1, 2, \dots, 16$).

The amplitude-weighted average propagation direction vector at the location $\bar{\mathbf{r}}_0$ was calculated as,

$$\bar{\mathbf{v}}(\bar{\mathbf{r}}_0) = \sum_{p=1}^{16} |\Gamma_p(\bar{\mathbf{r}}_0)| \cdot (\cos \theta_p \bar{\mathbf{e}}_1 + \sin \theta_p \bar{\mathbf{e}}_2). \quad (5.12)$$

These vector fields allow quantitative characterization of shear wave propagation as well as qualitative features. The divergence of these vector fields was used to qualitatively assess wave energy in the brain. In particular, anatomic boundaries, at which reflection occurs, appear as energy sources and sinks in these fields. This approach is illustrated in Figure 5.3, which shows shear wave propagation in a cylindrical gel sample excited by a central stinger⁵.

Material Property Estimation

Local frequency estimation (LFE) [76] has been used to locally extract the wavenumber $k = |\bar{\mathbf{k}}|$ from *displacement* wave fields in order to estimate the *elastic* shear modulus [21, 90]. LFE-based inversion is attractive because it allows material parameters to be estimated without explicitly invoking the coupled or uncoupled equations of motion (Equations 5.5–5.6b), thus obviating the need to numerically compute second or third-order spatial derivatives. LFE applied to displacement fields is challenging in practice since the effects of dilatational waves, rigid body motion, boundary reflections, and standing wave patterns can corrupt wavelength estimates. Investigators have attempted, not always successfully, to circumvent these effects by aggressively filtering displacement data [90] or by taking the curl of the equation of motion [152], which requires third-order spatial derivatives.

In this study, *viscoelastic* properties of brain tissue at multiple frequencies were obtained by local frequency estimation (LFE) applied to *distortion* fields. According to Equation 5.6b, all components of the distortional wave field ($\nabla \times \bar{\mathbf{u}}$) depend only on the shear modulus and density of the media. Therefore, in mechanically isotropic and locally homogeneous media as we assume here, the shear modulus can be extracted from any one component of the distortion field so long as that component is activated. Application of LFE to the distortion component identified in this study

⁵cf. Okamoto et al. [119] for gel experiment details.

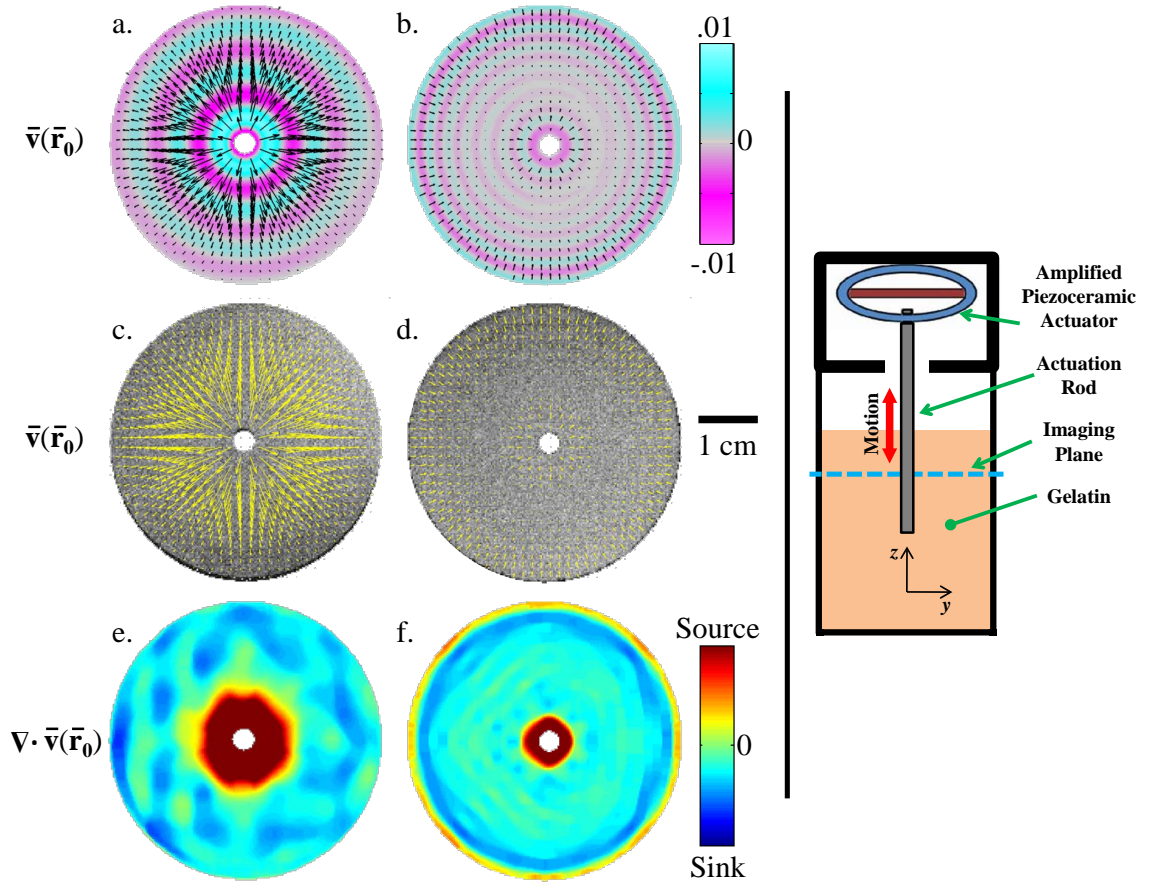


Figure 5.3: (a-f) Vector fields of amplitude-weighted average propagation direction in a homogeneous cylinder of gelatin in which both the container and a central rod are coupled to a piezoelectric actuator. Vector fields are superimposed on (a,b) estimated distortion fields Γ and (c,d) high resolution “anatomical” images. (e,f) Divergence of the propagation direction field highlights energy production (source) and dissipation (sink). (a,c,e) At 150 Hz shear waves propagate predominantly outward. (b,d,f) At 400 Hz shear waves propagate both inward and outward, and interfere destructively at intermediate radial locations. Standing waves due to constructive interference are also possible. Standing waves in this system would be indicated by distortion fields with significant amplitude but near-zero average propagation velocity.

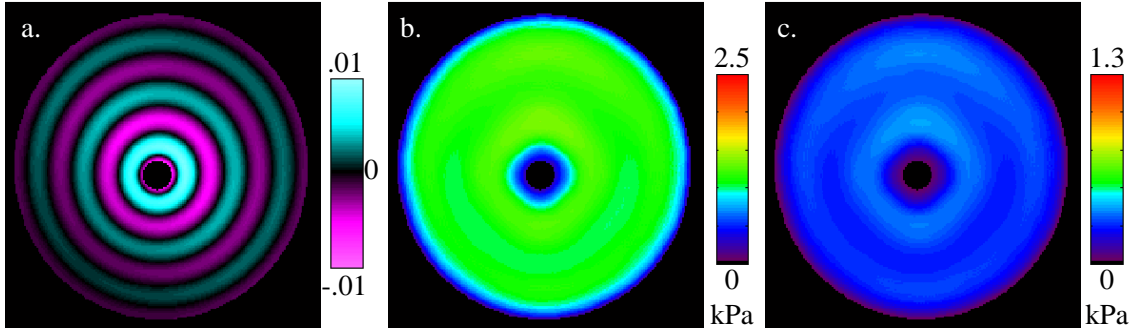


Figure 5.4: The presented viscoelastic inversion scheme was tested on MRE data obtained in gelatin [119]. (a) Distortion wave field (Γ). Viscoelastic moduli (b) G' and (c) G'' . (150Hz)

(Γ) avoids inversion artifacts attributed to dilatational waves and rigid body motion in displacement data.

Implicit in existing LFE-based inversion formulations [21, 90, 51] is the wave phase velocity relation $c = \omega/k$, which permits *elastic* material property reconstruction. Nevertheless, the equation describing planar shear wave propagation in an isotropic lossy medium,

$$\begin{bmatrix} k^2 - \alpha^2 & 2\alpha k \\ -2\alpha k & k^2 - \alpha^2 \end{bmatrix} \begin{Bmatrix} G' \\ G'' \end{Bmatrix} = \begin{Bmatrix} \rho\omega^2 \\ 0 \end{Bmatrix}, \quad (5.13)$$

could be employed to extract *viscoelastic* shear moduli [80, 7]. We used the LFE implementation provided by Grimm et al. [51] to locally obtain the wavenumber k , then applied Equation 5.13 with our global estimates of attenuation constant α to extract viscoelastic shear moduli regionally. An exponential form of α was assumed because it is a simple and intuitive model of dissipation, and approximates the observed behavior. This approach is illustrated in MRE data obtained in cylindrical gel sample actuated at 150 Hz. Estimates of viscoelastic moduli G' and G'' are presented in Figure 5.4. These estimates (mean $G' = 1111$ Pa; mean $G'' = 260$ Pa) are consistent with those reported in Okamoto et al. [119] (mean $G' = 1106$ Pa; mean $G'' = 151$ Pa).

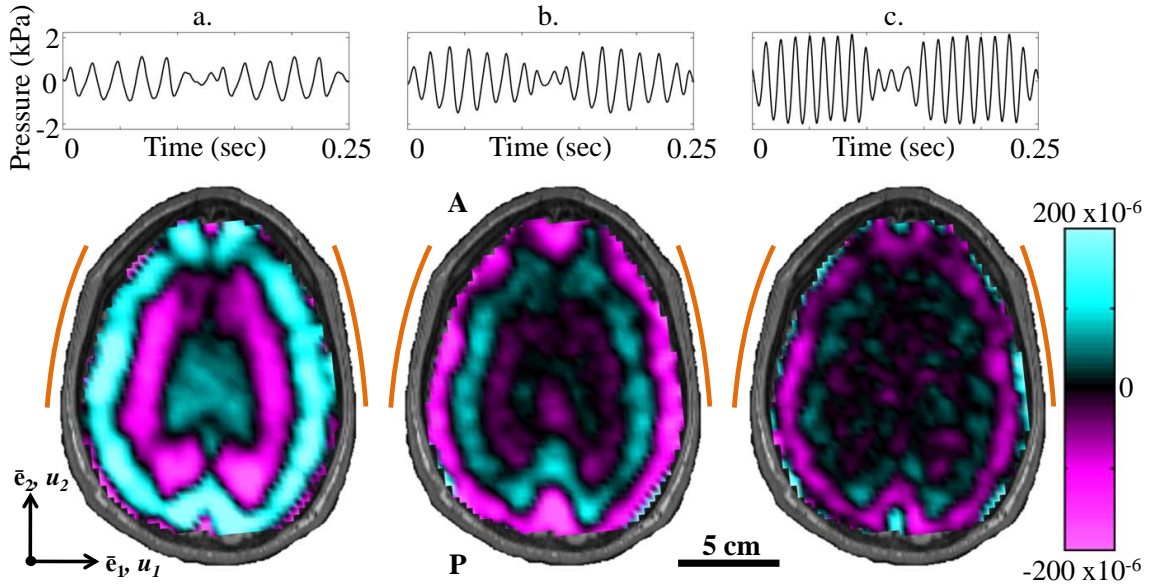


Figure 5.5: (Top) Waveforms of the pressure applied to the skull in one subject: (a) 45 Hz; (b) 60 Hz; (c) 80 Hz. (Bottom) Distortion wave fields (Γ , dimensionless) observed in the human brain in response to the applied pressure fields above. Arcs on the left and right denote the locations of passive actuator pads. (S008)

5.4 Results

5.4.1 Extracranial pressure and brain deformation

Acoustic pressure applied to the head near the left and right pterion produces distortional (shear) waves in the brain (Figure 5.5). Spatiotemporal patterns of distortion reflected propagation of shear waves which was generally, but not exclusively, from the skull inward. One might expect anatomical differences in the skull and brain of individual subjects to cause differences in the responses of the brain. Averaged over the entire brain slice, the pressure-normalized distortion (Γ/P) showed consistent magnitude (Figure 5.6a). Some subject-to-subject variation was observed; however, among subjects who experienced all three frequencies of excitation, the decrease in response with frequency is consistent.

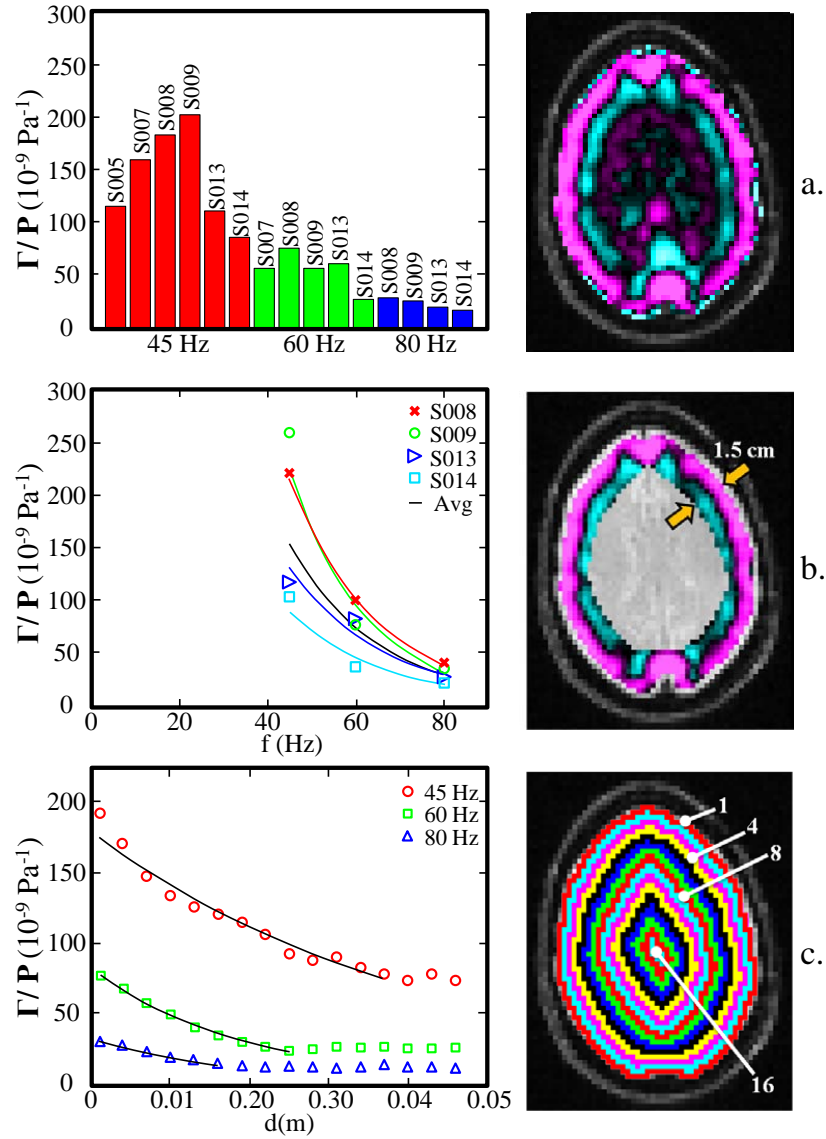


Figure 5.6: Pressure-normalized distortion Γ/P (Equation 5.8) was used to evaluate transmission and attenuation. (a) The amplitude of Γ/P was spatially averaged over the entire brain (shown right) and plotted for each subject. Subject-to-subject variability exists; however when data were acquired at all three frequencies in the same subject, the amplitude consistently decreased with increasing acoustic frequency. (b) The amplitude of Γ/P was spatially averaged in a 1.5 cm-wide annular region of brain tissue immediately interior of the skull/dura mater (shown right) and plotted as a function of acoustic frequency. Transmission coefficients were extracted by exponential curve fit: $\Gamma/P = A_f \exp(-\beta_f f)$; min $\beta_f = 0.046 \text{ Hz}^{-1}$ (S014), max $\beta_f = 0.058 \text{ Hz}^{-1}$ (S009), mean $\beta_f = 0.050 \text{ Hz}^{-1}$. (c) The amplitude of Γ/P was regionally averaged in concentric annular elliptical rings (shown right) and plotted as a function of depth from the brain skull boundary. Attenuation coefficients were extracted by exponential curve fit: $\Gamma/P = A_d \exp(-\alpha d)$; 45 Hz: $\alpha = 23.7 \text{ m}^{-1}$; 60 Hz: $\alpha = 51.1 \text{ m}^{-1}$; 80 Hz: $\alpha = 54.3 \text{ m}^{-1}$.

5.4.2 Quantitative analysis of shear wave energy transmission into the brain

The transmission of mechanical loads through the skin, skull, and meninges was evaluated via pressure-normalized distortion (Γ/P) in the annular region of interest in the brain adjacent to the skull (Figure 5.6b). This regionally-averaged quantity was calculated for each subject, plotted as a function of frequency, and fit to an exponential model. A clear decrease in transmissibility with frequency is evident over this range.

5.4.3 Quantitative analysis of shear wave energy attenuation within the brain

The attenuation of pressure-normalized distortion (Γ/P) was averaged within annular regions of interest and plotted as a function of depth from the brain-skull boundary (Figure 5.6c). Data from all subjects were averaged together for a given frequency. The shear wave attenuation parameter α , which characterizes the dissipative behavior of brain matter, was extracted for each frequency by performing a least-squares fit with a model of exponentially decaying amplitude.

5.4.4 Reflection of shear waves at anatomical interfaces

Vector fields of amplitude-weighted average propagation direction of shear waves in the human brain were calculated and presented in Figure 5.7. These vectors highlight that propagation is generally inward from the skull toward the interior of the brain, but anomalies are apparent at the anterior and posterior extremes of the midline of the brain. This is more pronounced, and occurs over a larger region, in the posterior midline region. The locations of these anomalies correspond to the intersections of the tough, relatively stiff membranous insertion of the dura mater, the falx cerebri, with the brain in the images. The falx extends from the roof of the skull down between the hemispheres of the brain. Wave propagation near the posterior midline may be affected by the tentorium, which lies below the image plane. The tentorium

Table 5.1: Viscoelastic properties of brain tissue (mean ± 1 standard deviation).

Frequency (Hz)	k ($\times 10^2$ rad/m)		α (rad/m)		G' (kPa)		G'' (kPa)	
	Gray	White	Gray	White	Gray	White	Gray	White
45 (n=6)	1.68 \pm 0.142	1.46 \pm 0.161	23.7	23.7	2.8 \pm 0.5	3.7 \pm 0.8	0.80 \pm 0.2	1.3 \pm 0.4
60 (n=5)	1.99 \pm 0.126	1.89 \pm 0.305	51.1	51.1	3.1 \pm 0.3	3.3 \pm 0.1	1.7 \pm 0.3	2.0 \pm 0.1
80 (n=4)	2.26 \pm 0.104	2.17 \pm 0.131	54.3	54.3	4.4 \pm 0.3	4.7 \pm 0.6	2.3 \pm 0.2	2.4 \pm 0.5

is a tent-like structure that supports the occipital lobe of the cerebrum and separates the cerebrum from the cerebellum. Propagation vector and divergence fields for all subjects at 45 Hz are presented in Figures 5.9 and 5.10.

5.4.5 Estimates of viscoelastic parameters from shear wave fields

The viscoelastic shear moduli G' and G'' of the brain parenchyma were calculated for all subjects using local frequency analysis of the distortion field Γ . In Figure 5.8 viscoelastic estimates are presented spatially in one subject at 45 Hz. In Table 5.1 ensemble average moduli for all subjects were calculated in white and gray matter regions of interest. Magnitude images were used to manually segment gray and white matter regions of interest in each subject. The attenuation coefficient α was assumed to be approximately constant over the brain, which provides an estimate of loss modulus G'' .

Moduli averaged over regions of interest in gray matter and white matter for all subjects are given in Table 5.1. Spatial heterogeneity in G' is consistent with expected differences in stiffness of interior white matter [64, 172], which is composed of myelinated axonal fibers, and cortical gray matter.

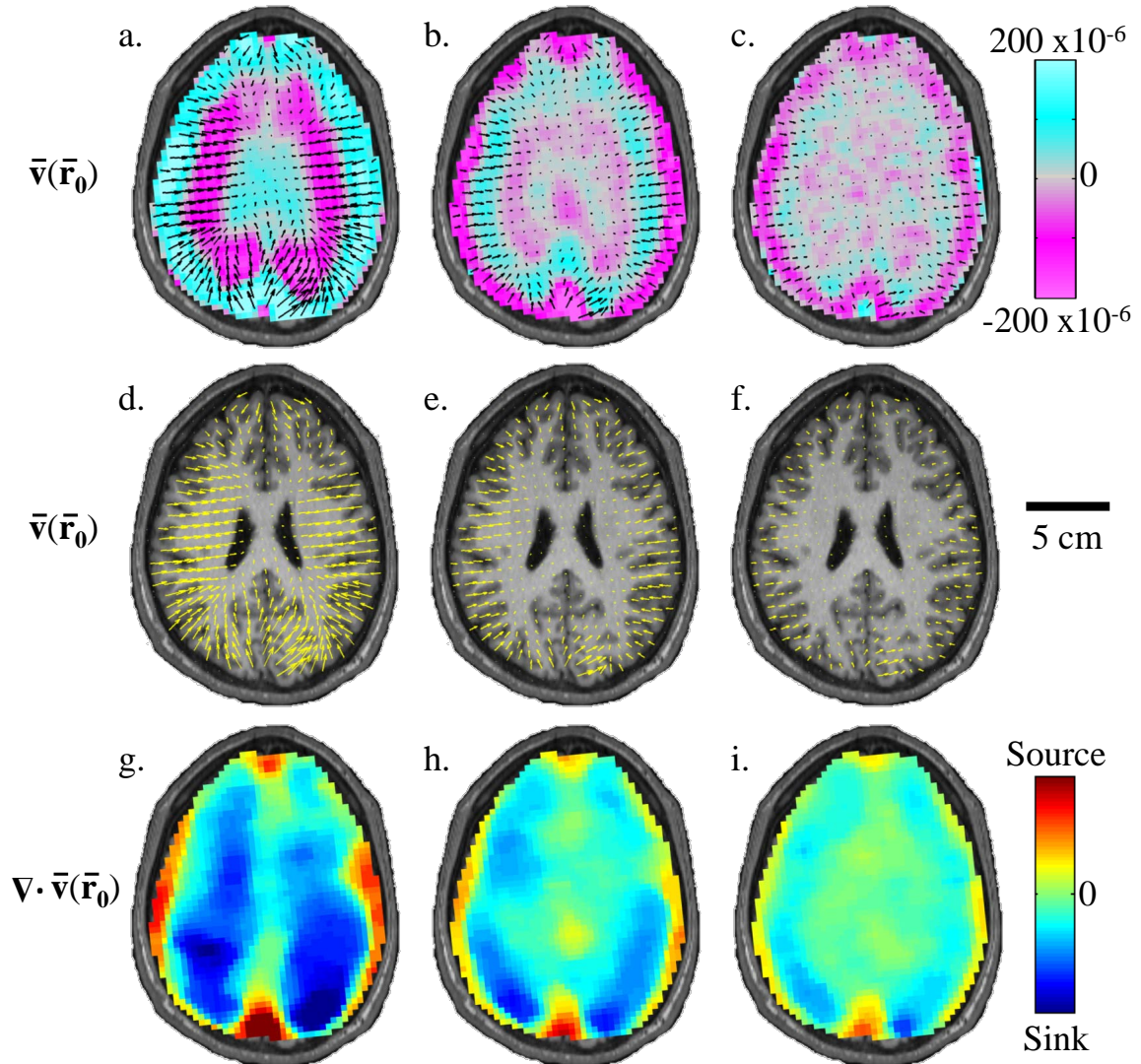


Figure 5.7: Vector fields of amplitude-weighted average propagation direction superimposed on (a-c) estimated distortion fields and (d-f) high resolution anatomical images in one human subject at three frequencies. Shear waves in the brain appear to propagate inward from the brain-skull boundary toward the ventricles. (g-i) Divergence of the propagation direction field at the anterior/posterior falx and above the tentorium indicates that these membranous structures may act like sources of shear wave excitation. (a,d,g) 45 Hz; (b,e,h) 60 Hz; (c,f,i) 80 Hz. (S008)

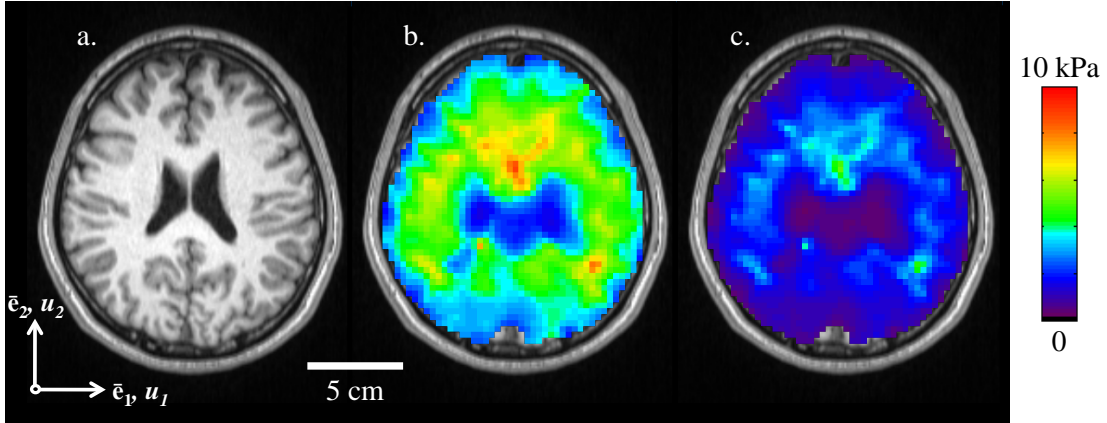


Figure 5.8: Spatial maps of the viscoelastic material properties of intact, living human brain were calculated using a distortion-based LFE approach (Equation 5.13). (a) T1-weighted anatomical image of the analysis slice. Viscoelastic moduli (b) G' and (c) G'' . (S005, 45Hz)

5.5 Discussion

In this study, the living human head was subjected to harmonic, laterally symmetric, extracranial pressure loading at 45, 60, and 80 Hz. The applied loading produced propagating distortional (shear) waves in the brain parenchyma. Distortion Γ was normalized by the applied RMS pressure load and analyzed to characterize the structural dynamic properties of the head. Transmission of harmonic extracranial acoustic pressure load through the skull decreases as the acoustic frequency increases (Figure 5.6b). On average, outer regions of the brain experience pressure-normalized distortion Γ/P at amplitudes of approximately $150 \times 10^{-9} \text{Pa}^{-1}$ at 45 Hz, but less than $30 \times 10^{-9} \text{Pa}^{-1}$ at 80 Hz. Attenuation of propagating shear (distortional) waves within the brain increases as the extracranial acoustic frequency increases (Figure 5.6c) as expected for a viscoelastic system [80], such as the brain.

Reflection of shear waves in the brain was assessed from amplitude-weighted average propagation vector fields (Figure 5.7). Amplitude-weighted average propagation vector fields permit qualitative and quantitative characterization of shear wave propagation. Propagation was generally inward from the skull toward the interior of the brain, with important anomalies apparent at the anterior and posterior extremes of the brain midline. This was more pronounced, and occurred over a larger region, in the posterior midline region. The locations of these anomalies correspond to the

intersections of the brain with the tough, relatively stiff membranous insertion of the dura mater: the falx cerebri. The falx extends from the roof of the skull down between the hemispheres of the brain, serving as a transmission barrier. The posterior wave field may also be affected by reflections from the tentorium cerebelli, even though the tentorium lies below, and does not intersect, the image plane. The tentorium is a tent-like structure that supports the occipital lobe of the cerebrum and separates the cerebellum from mechanical waves in the cerebrum. Divergence of the propagation vector fields indicate anatomical boundaries are regions of energy production (source) and dissipation (sink). This technique was illustrated by characterization of shear waves in a simple cylindrical gel sample (Figure 5.3).

Viscoelastic shear moduli were estimated from approximations of the local wavenumber k and global attenuation parameter α as evident from distortional wave fields Γ . Estimates of brain viscoelasticity provided here are within the wide range of values reported in a comprehensive review [24] of the mechanical properties of human brain tissue estimated by various methods. Scan duration limited our multifrequency study to data collection on a single slice. The assumption that variations in the through-plane direction are small (inherent in the use of single-slice in-plane displacement data rather than multislice 3D displacement data) leads to wavelength estimates that may be longer than the true wavelength. Accordingly, estimates of G' presented here may be higher than the values that would be estimated from multi-slice 3D displacement data. Spatial heterogeneity in G' is consistent with expected differences in stiffness of interior white matter [64, 172], which is composed of myelinated axonal fibers, relative to cortical gray matter. This technique was illustrated by characterization of shear waves in a cylindrical gel sample (Figure 5.4).

MRE displacement data consist of the volume-averaged NMR signal within discrete volume elements (voxels). Consequently, NMR signal decreases with decreasing voxel volume. The voxel size in this study ($3 \times 3 \times 3 \text{ mm}^3$) provides adequate signal-to-noise ratio without requiring multiple NMR excitations, which would lengthen scan duration. Spatial resolution in this study is comparable to other MRE studies in the human brain at 1.5 T [177, 55, 159, 160]. In some cases [177, 159, 160], the investigators have decreased the in-plane voxel dimension ($1.5 \times 1.5 \text{ mm}^2$) while increasing the through-plane dimension (slice thickness), to 6 mm, for example. The smallest isotropic voxels used to date for human brain MRE are $2 \times 2 \times 2 \text{ mm}^3$, as reported

by Romano et al. [137]. The current voxel dimension is considerably smaller than the shear wave wavelength at 45 Hz (Figure 5.5a, Figure 5.7a). This resolution is also sufficient to resolve major anatomical features and regions of the brain (Figure 5.8), although at boundaries and thin structures some “volume-averaging” occurs within each voxel. Errors due to numerical approximations of derivatives are a primary concern when working with discrete samples of continuous data. An advantage of the viscoelastic inversion scheme introduced in this study is that longitudinal wave and rigid body contributions can be minimized at the expense of only one spatial derivative.

5.6 Conclusions

Data were limited to low pressure levels and strain levels far below any suspected for TBI, but offer important quantitative data for validation of mathematical models, and insight into the structural response of the brain and skull.

1. Frequency-dependent transmission of energy into the brain. Over the range of conditions tested, the skin, skull, and meninges (e.g., the dura, pia, and arachnoid matters) behave as a low-pass filter. Transmission of mechanical energy into the brain decreases with increasing acoustic frequency. The measured values of transmissibility are important parameters to replicate in mathematical models of brain biomechanics.
2. Frequency-dependent dissipation of energy within the brain. The approximately exponential decay in wave amplitude with depth into the brain confirms and quantifies the expected viscoelastic response of brain tissue. The measured values of attenuation, and the increase in attenuation with frequency, are also important to replicate in simulations.
3. Membranous structures within the skull affect wave propagation patterns. The propagation direction of waves was predominantly radially inward, from the brain-skull boundary toward the ventricles, but outward propagation from membranous structures including the falx cerebri is also observed. Reflections from such structures outside the image plane (tentorium cerebelli) may also affect

the wave field. The effects of these membranous structures on wave propagation direction are likely to be very important in determining the response of brain to impact and blast.

These data illuminate fundamental mechanical properties of the skull, brain, and associated intracranial anatomy. The quantitative details of the response of the intact living head to extracranial acoustic pressure load could be used to asymptotically validate computer simulations of blast-induced TBI by illuminating the expected behavior at lower amplitude levels that are governed by linear system theory. These data also highlight an emerging role of MRI as a tool for not only material characterization, but also for the structural function characterization of organ systems.

5.7 Supplementary Material

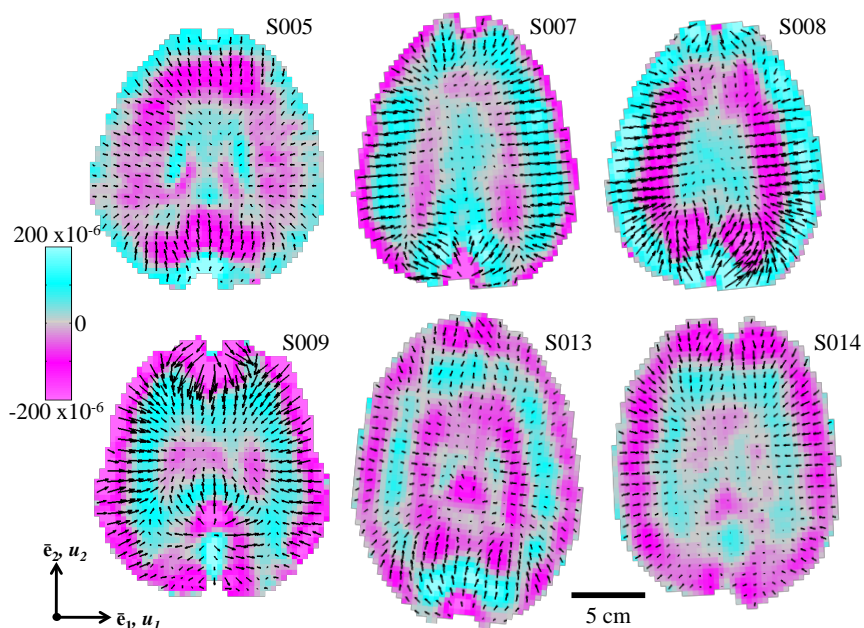


Figure 5.9: Vector fields of amplitude-weighted average propagation direction superimposed on the distortion field Γ in each subject at 45 Hz.

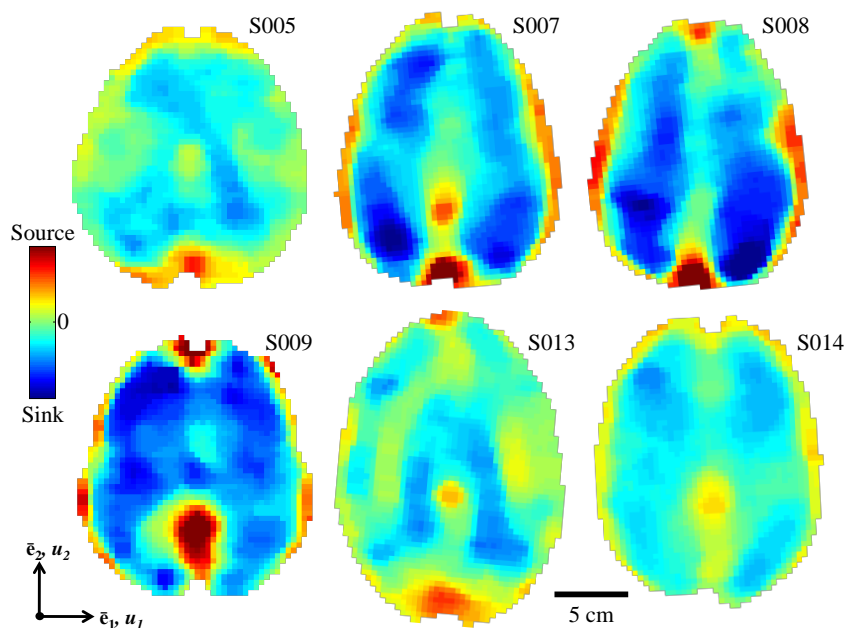


Figure 5.10: Divergence of propagation direction vector fields in each subject at 45 Hz.

Chapter 6

Preliminary Work: 3D MRE and DTI in Human Subjects

6.1 Overview

In this chapter, two preliminary studies are presented as the initial stages of a more comprehensive work for future publication. The first study is an investigation of the displacement, strain, and distortion of brain when harmonic extracranial pressure loads are applied. This study differs from that presented in Chapter 5 in two ways: vector field displacement data were acquired over a 3D image volume and pressure loading was applied asymmetrically (right pterion only). Volumetric vector field displacements provide empirical evidence of brain tissue near-incompressibility. Asymmetric loading of the skull produced wave fields in the brain with characteristics surprisingly similar to those acquired with symmetric loads (right and left pterion together). The second study applies the anisotropic inversion scheme developed in Chapter 2 to simulated data. A parametric study was conducted to provide practical insight for the eventual application of this technique to data from human brains. Inversion was performed on waves traveling through homogeneous and heterogeneous anisotropic media. The inversion method performs well; however, there are limitations. Future studies will focus on fully understanding inversion limitations and extracting anisotropic mechanical properties from MRE and DTI data acquired in the human brain.

6.2 3D Strain Dilation and Distortion Estimated in the Living Human Brain from MR Images of Propagating Shear Waves.

6.2.1 Introduction

Traumatic brain injury (TBI) can result from blunt force trauma, rapid inertial loading, or extracranial pressure (i.e., explosive blast). Much of the pathway between mechanical insult and neurological injury remains unclear, in part because data on the mechanical response of the brain are difficult to acquire *in vivo*. The physics of measuring harmonically-varying displacement fields with motion-sensitive magnetic resonance imaging (MRI) is well understood [112], yet to date data in the human brain have not been investigated in terms of strain and local rotation. Here these kinematic quantities are examined and new light is shed on biomechanics of the living intact human brain as it is subjected to harmonic acoustic pressure load.

6.2.2 Methods

The brains of three healthy subjects (2M/1F) aged 25-46 years old (mean: 34.3 yr) were imaged. Five transverse-oblique slices of motion encoded data were acquired for each subject through the central (Inferior/Superior) cerebrum. The total scan time per subject was approximately 15 minutes. Experimental protocols were approved by the institutional Human Research Protection Office Internal Review Board to ensure that the rights and welfare of each research participant were protected.

Displacement vector field $u_i(x, y, z)$ data were acquired with a specialized gradient-recalled echo (GRE) NMR imaging pulse sequence equipped with specialized motion-encoding magnetic-field gradients. Data were collected using a 1.5 T MAGNETOM Avanto (Siemens) series whole-body clinical scanner equipped with a phased-array head coil (TR/TE: 133/28.2 ms, flip angle: 25°, NEX: 1, resolution: 3x3x3 mm³). The absolute peak motion-encoding magnetic-field gradient amplitude was 19.3 mT/m,

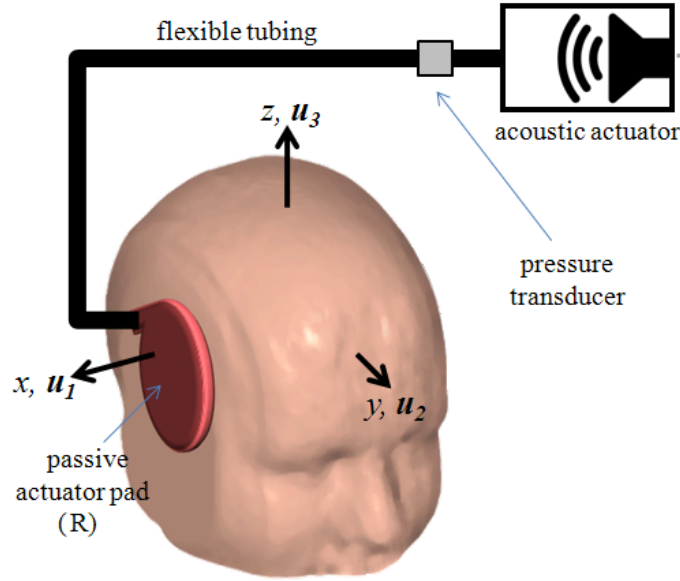


Figure 6.1: Oscillatory pressure was generated by an acoustic actuator and transmitted to a passive actuator pad positioned near the right pterion bone via flexible tubing.

nominally. Data were acquired with a temporal resolution of four points per actuation cycle.

Motion was induced in the brain using an acoustic actuation system (ResoundantTM, Resoundant Inc., Rochester, MN) affixed to each subject's skull at the right pterion (Figure 6.1). The actuation system was configured to transmit a 1 kPa pressure-wave train at 45 Hz in synchronization with the imaging sequence. MRI data were sensitized to motion with a single-cycle magnetic-field gradient. A switched-polarity encoding scheme was employed to remove systematic phase errors and enhance displacement contrast. Phase-contrast images were obtained by complex division of positive and negative polarity phase images and converted to displacements with a sensitivity factor of $7.24 \mu\text{m}/\text{rad}$. Displacement data were Gaussian filtered (kernel: $5 \times 5 \times 5$ voxel, std: 1 voxel).

Displacement gradients and shear angles were observed to be small for all data. As such, the 3D infinitesimal strain tensor

$$\epsilon_{ij} = (u_{i,j} + u_{j,i}) / 2 \quad (6.1)$$

was calculated, where subscript (i, j) denotes $\partial u_i / \partial x_j$ for $i, j, k \in \{1, 2, 3\}$. The curl of the displacement field

$$\Gamma_i = e_{ijk} u_{j,k} \quad (6.2)$$

describes local rotation about the i axis, where e_{ijk} is the Levi-Civita permutation operator.

Normal and shear components of the octahedral strain were calculated to assess the dilatational and distortional deformation components [100]. Octahedral normal strain

$$\epsilon_n = (\epsilon_{11} + \epsilon_{22} + \epsilon_{33}) / 3 \quad (6.3)$$

describes dilatation. Octahedral shear strain

$$\begin{aligned} \epsilon_s = 2/3 [& (\epsilon_{11} - \epsilon_{22})^2 + (\epsilon_{11} - \epsilon_{33})^2 + (\epsilon_{22} - \epsilon_{33})^2 \\ & + 6 (\epsilon_{12}^2 + \epsilon_{13}^2 + \epsilon_{23}^2)]^{1/2} \end{aligned} \quad (6.4)$$

describes distortion.

6.2.3 Results & Discussion

Measured displacement fields are shown for one subject in Figure 6.2. Estimates of strain and local rotation (Equations 6.1 and 6.2) are presented in Figures 6.3 and 6.4. Low octahedral normal strain furnishes evidence that tissue compressibility is low *in vivo*. Relatively high octahedral shear strain and local rotation indicate distortion is the prominent deformation mode.

6.2.4 Conclusions

The ability to measure 3D displacement fields in a 3D brain volume due to harmonic excitation of the skull was demonstrated in this section. Full 3D strain fields were obtained. MRI-based displacement measurements provide new insight into brain biomechanics. Extracranial acoustic pressure excitation produces distortional brain deformation. Observations of tissue dilatation and distortion may illuminate injury

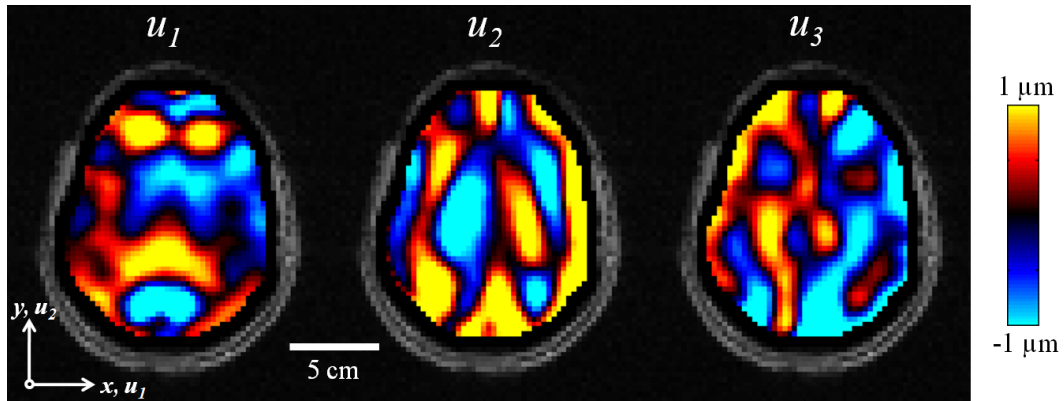


Figure 6.2: Measured displacement fields shown above were used to calculate strain and local rotation fields (S002, Slice 3 of 5).

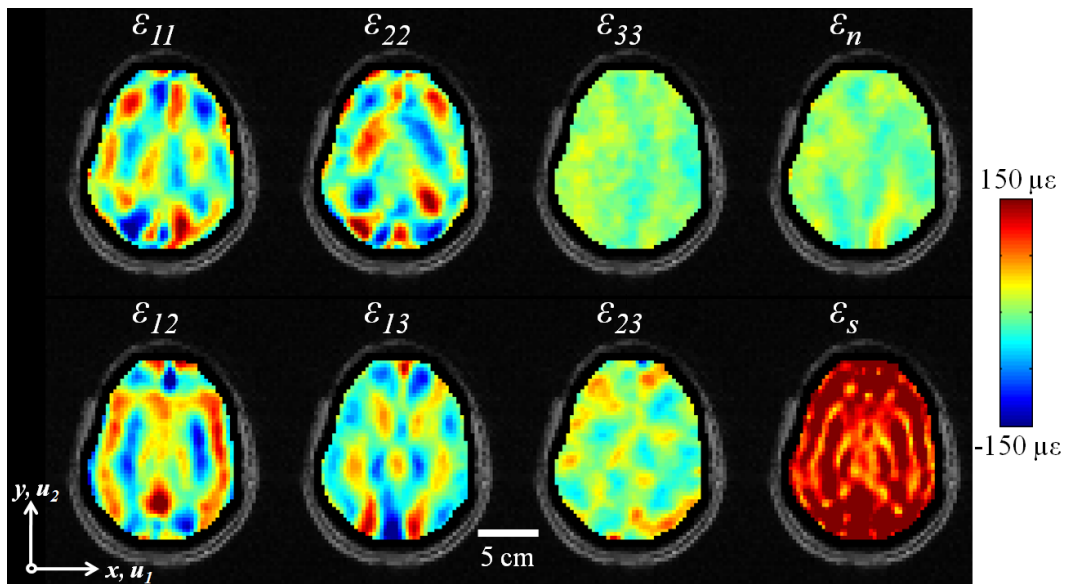


Figure 6.3: Calculated strain fields in the living intact human brain resulting from extracranial acoustic pressure load (S002).

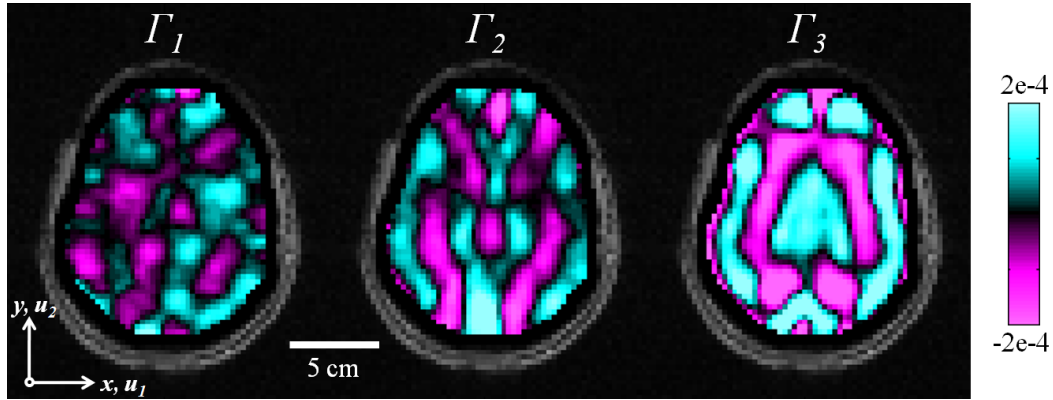


Figure 6.4: Calculated local rotation fields indicate significant distortional wave motion (S002).

mechanisms. The kinematic quantities calculated here should be used to validate computer models of the brain. Future work will investigate brain response to alternative loading locations.

6.3 Estimating Transversely Isotropic Material Parameters with Magnetic Resonance Elastography and Diffusion Tensor Imaging

6.3.1 Introduction

Throughout this work magnetic resonance elastography data have been used to estimate isotropic mechanical properties of various media. In reality, many tissues (viz. white matter) possess structural anisotropy and in turn may exhibit some degree of mechanical anisotropy. Measurements of mechanical anisotropy could enhance numerical models of brain biomechanics, and may also have utility as a marker of tissue health. With the exception of Sinkus et al. [151] and Romano et al. [137], exploration of anisotropic mechanical properties with MRE has not been addressed. In this section, a proof-of-concept study is conducted with numerical wave field data to demonstrate the inversion routine described in Chapter 2. As in Chapter 2, we restrict the analysis to planar wave propagation in transversely isotropic (TI) media.

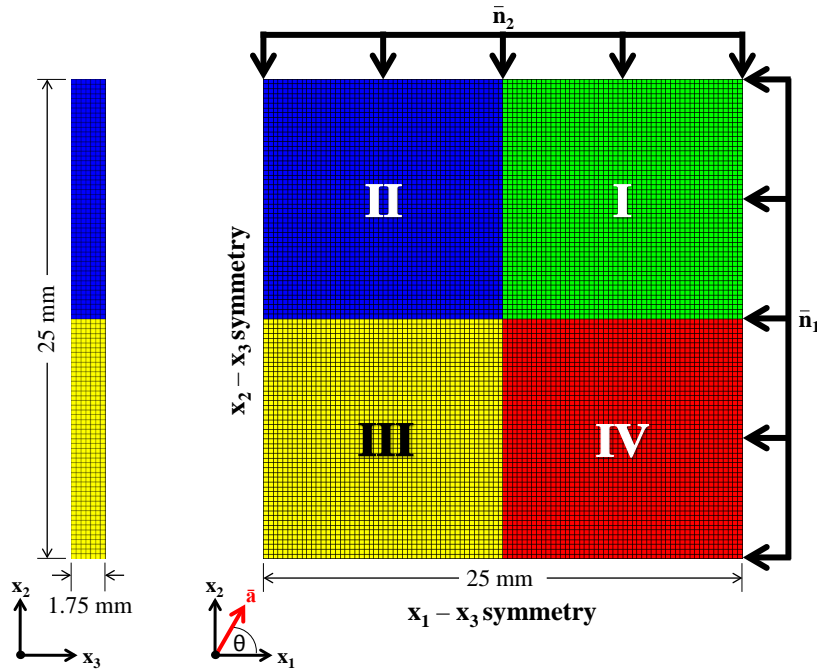


Figure 6.5: A thin slab finite element model used for inversion validation. Subdomains are color coded and labeled I-IV. All subdomains are connected so that displacement continuity exists. The four quadrants create one monolithic structure; however, the material properties within each subdomain may be uniquely specified. Harmonic steady-state motion, polarized in the x_3 -direction, was applied to the sides of domains I, II and IV, simultaneously. The wave normals associated with this motion are denoted as $\bar{\mathbf{n}}_1$ and $\bar{\mathbf{n}}_2$. Orientation of the material symmetry axis $\bar{\mathbf{a}}$ is specified as $\cos \theta = \bar{\mathbf{a}} \cdot [1, 0]$. Plane symmetry boundary conditions were applied as shown.

6.3.2 Methods

The TI inversion theory was developed in Chapter 2. Practical implementation is the focus of this section. Consider a plane wave propagating in the direction of the unit vector n_i . If the x_1 - x_2 plane is defined as the plane that contains both the fiber direction and the propagation direction, the displacement field due to this single plane wave can be expressed as

$$(u_1, u_2, u_3) = (p_1, p_2, p_3) \exp[ik(n_1 \cdot x_1 + n_2 \cdot x_2 - \omega t)]. \quad (6.5)$$

Table 6.1: Properties of simulated TI medium. Engineering constants E_T , E_L , μ_T , and μ_L (Pa). Poisson ratios ν_{LT} , ν_{TL} , and ν_T (dimensionless).

E_T	E_L	μ_T	μ_L	ν_{LT}	ν_{TL}	ν_T
2748	8250	750	1500	0.4997	0.1665	0.8322

Table 6.2: Properties of simulated TI medium in Spencer’s [156] notation (Pa).

α	β	λ	μ_T	μ_L
200	3000	1x10 ⁶	750	1500

As previously described, one of the two shear wave velocities in incompressible TI media has the form

$$\frac{\omega^2}{k^2}\rho = \mu_L \cos^2 \theta + \mu_T \sin^2 \theta. \quad (6.6)$$

This equation governs waves in which the polarization direction is perpendicular to both the fiber direction and the propagation direction.

If directional filters along x_1 - and x_2 -axes are applied to the wave field individually, local frequency estimation can be used to recover the directional wavenumbers $k_1 = kn_1$ and $k_2 = kn_2$. Use of Equation 6.6 with each directional wavenumber provides a system of two equations,

$$\rho\omega^2 \begin{Bmatrix} 1/k_1^2 \\ 1/k_2^2 \end{Bmatrix} = \begin{bmatrix} \cos^2 \theta & \sin^2 \theta \\ \cos^2 \theta & \sin^2 \theta \end{bmatrix} \begin{Bmatrix} \mu_L \\ \mu_T \end{Bmatrix}. \quad (6.7)$$

Both shear moduli can be determined for each point in the medium.

A finite element model was used to simulate wave propagation in TI media as a function of the material symmetry axis orientation $\bar{\mathbf{a}}$. Our anisotropic inversion routine was applied to the simulated data to estimate the TI shear moduli μ_T and μ_L . Figure 6.5 shows the thin square slab geometry modeled and the applied boundary and loading conditions (nodes: 81,608; hexahedral elements: 70,000; degrees-of-freedom: 244,824). The lower left, through-plane edge of III was clamped to fully constrain the model. Anisotropic mechanical properties of the TI material simulated in this study are presented in Tables 6.1 and 6.2. Numerical simulations include energy dissipation. A “loss factor” of 0.05 was used.

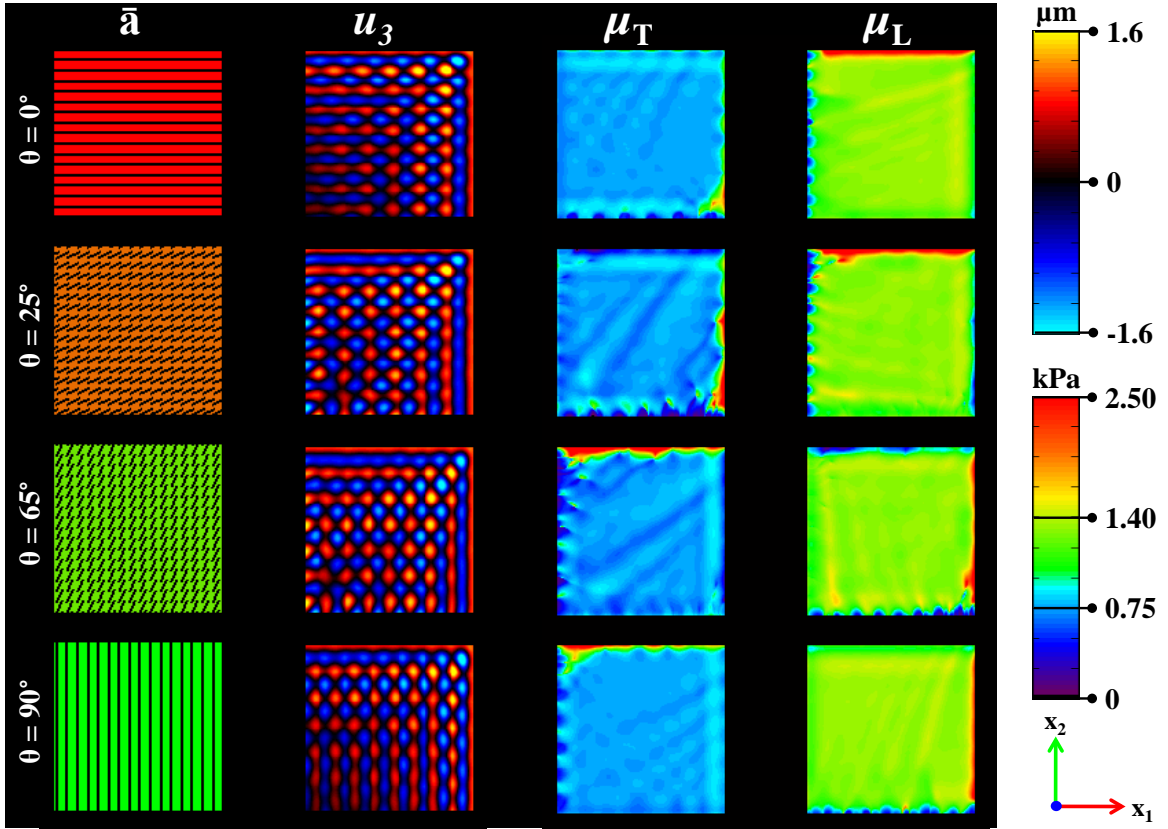


Figure 6.6: Validation of the TI inversion algorithm on a homogeneous anisotropic medium in various orientations. The material symmetry axis orientation $\bar{\mathbf{a}}$ and u_3 -displacement field are simulated inputs to the inversion algorithm. Elastograms of shear moduli μ_T and μ_L are algorithm outputs. (True μ_T and μ_L are 750 Pa and 1500 Pa, respectively.)

6.3.3 Results & Discussion

Both homogeneous and heterogeneous anisotropic media were simulated in this validation study. Simulations in homogeneous TI media were performed to assess the sensitivity of the algorithm to variations in the fiber (symmetry) axis orientation. Estimates of the TI shear moduli μ_T and μ_L at four different orientations are presented spatially in Figure 6.6. Averaged estimates of the shear moduli have been tabulated with respect to the fiber orientation simulated (Table 6.3).

Simulations in heterogeneous TI media more accurately reflect conditions encountered in practice. A heterogeneous medium was created by assigning a different material fiber orientation to each subdomain. In living species, isotropic structures (i.e., gray

Table 6.3: Inversion performance in a homogeneous TI medium as the axis of material symmetry $\bar{\mathbf{a}}$ is varied. ($\cos \theta = \bar{\mathbf{a}} \cdot [1, 0]$)

θ (deg)	μ_T (Pa)		μ_L (Pa)	
	mean	stdv	mean	stdv
0	759	22	1421	48
15	758	37	1428	29
25	744	63	1397	39
35	763	111	1403	100
45	–	–	–	–
55	760	111	1408	99
65	745	66	1395	50
75	760	35	1430	32
85	759	28	1409	33
90	758	21	1415	36

Table 6.4: Inversion performance in heterogeneous anisotropic media. In domain I-IV a unique axis of material symmetry $\bar{\mathbf{a}}$ is specified. ($\cos \theta = \bar{\mathbf{a}} \cdot [1, 0]$) Domain III is mechanically isotropic, so theoretically $\mu_T = \mu_L$. (True μ_T and μ_L are 750 Pa and 1500 Pa, respectively. True μ_{iso} is 1500 Pa.)

Domain quadrant	θ (deg)	μ_T (Pa)		μ_L (Pa)	
		mean	stdv	mean	stdv
I	0	772	64	1375	130
II	35	728	388	1453	432
III	–	1429	95	1432	73
IV	90	787	61	1378	223

matter) are commonly juxtaposed to those exhibiting anisotropy (i.e., white matter). As such, our heterogeneous simulation also included a subdomain of isotropic material (i.e., $\mu_T = \mu_L$ theoretically). Results of this study are presented as Figure 6.7. Quantitative statistics are presented as Table 6.4.

Table 6.3 suggests TI inversion uncertainty increases as the angle between material symmetry axis and the x_1 -axis approaches 45° . Equation 6.7 is singular at $\theta = 45^\circ$. This is a limitation of the inversion implementation presented in this section.

Table 6.4 indicates uncertainty in anisotropy estimates increases when the medium is heterogeneous. This finding is consistent with our observations in heterogeneous

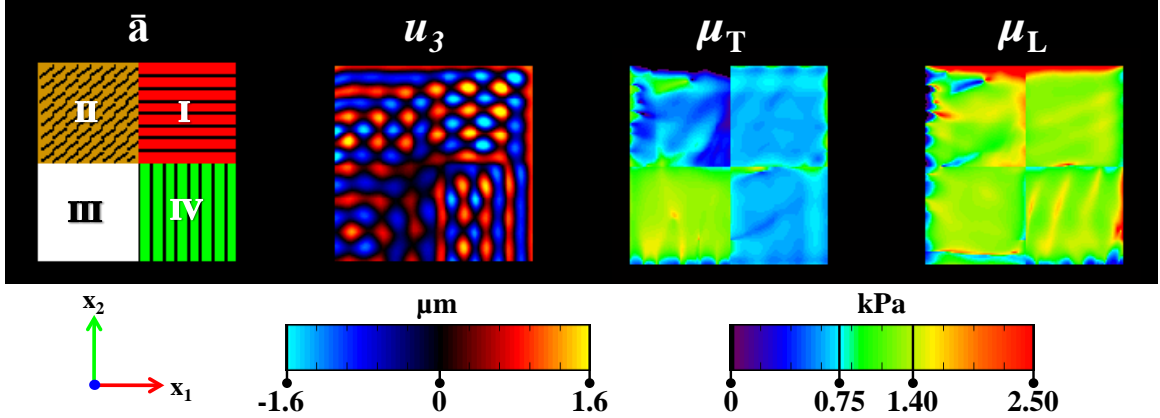


Figure 6.7: Validation of the TI inversion algorithm on a heterogeneous medium. The material symmetry axis orientation $\bar{\mathbf{a}}$ and u_3 -displacement field are simulated inputs to the inversion algorithm. Elastograms of shear moduli μ_T and μ_L are algorithm outputs. Note subdomain III is an isotropic material. (True μ_T and μ_L are 750 Pa and 1500 Pa, respectively. True μ_{iso} is 1500 Pa.)

isotropic media. Heterogeneity increases wave interference and refraction induced by boundaries and diminishes certainty in wavelength estimates.

6.3.4 Conclusions

In several subjects to date, data specifying the local fiber direction were acquired by DTI in the same image planes as MRE data. The combined data sets may be sufficient to estimate local material parameters of a transversely isotropic elastic material model.

To understand potential pitfalls and limitations of the developed inversion algorithm, finite element simulations of wave propagation in viscoelastic TI media were performed. FE models described simultaneous propagation of two shear wave polarizations (along two different directions). This creates two plane waves each with polarization in the x_3 -direction (u_3). One propagates in the negative x_2 -direction, the other in the negative x_1 -direction. Both shear moduli are activated by these waves at every point in the slab. A heterogeneous simulation model, one with subdomains of TI media at different orientations, was used to illustrate the performance of the inversion routine in heterogeneous media. It is important to note that another

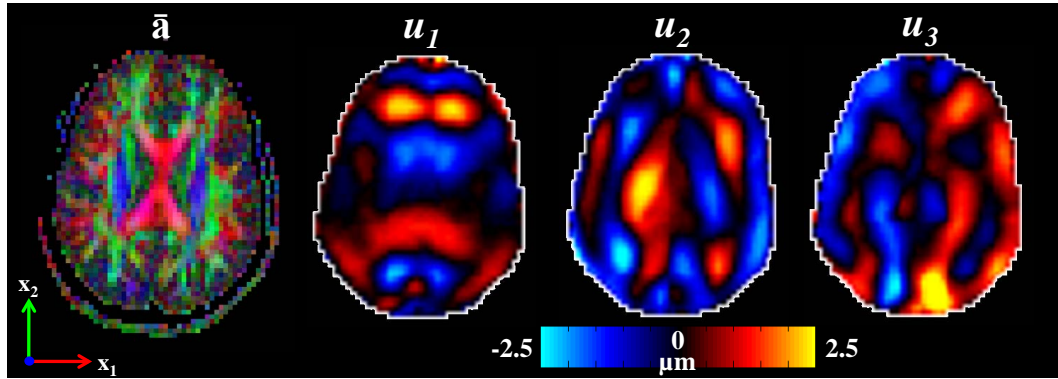


Figure 6.8: DTI and MRE data have been acquired in human brains. The principal diffusion direction $\lambda_1(\bar{v}_1)$ is used to orient the axis of material symmetry \bar{a} . In each voxel, \bar{a} and displacement components u_1, u_2, u_3 are specified. It may be possible to estimate mechanical anisotropy locally with these measurements. This will be the target of future studies.

shear wave polarization exists, and must be considered in general. Considering this additional polarization may be the key to numerically stabilizing Equation 6.7 at $\theta = 45^\circ$.

The work in this section must be considered preliminary, but represents important progress toward the ultimate objective of characterizing brain tissue adequately for accurate simulation of TBI. Future work will include application of the developed anisotropic inversion scheme to data acquired in human brains (Figure 6.8).

Chapter 7

Summary, Conclusions, and Future Directions

This work sought to use MRE to increase our understanding of the biomechanical behavior of the brain. New experimental methods were combined with improved data analysis techniques to gain insight into the structural-material mechanics of living brains when subjected to dynamic harmonic loads.

7.1 Summary of Work

The specific aims of this dissertation have been fulfilled as follows:

Aim 1: Develop and validate an isotropic viscoelastic inversion algorithm for MR elastography data.

A locally homogeneous, linear viscoelastic isotropic inversion algorithm was developed; its background and application to the mouse brain are described in Chapter 4. Chapter 3 describes how this algorithm was improved and validated through a comprehensive imaging study conducted on a calibrated gelatin phantom. This study was the first of its kind in this field. Mechanical bench-top tests and elastography measurements were performed in an overlapping frequency range.

Aim 2: Develop capabilities to perform high-throughput longitudinal MR elastography screening at high actuation frequencies in the living mouse brain.

As an additional feature of this work, the dispersive properties of the mouse brain were quantified for the first time. Chapter 4 describes a novel stereotaxic head-holding rig developed to induce shear waves in the mouse brain via an actuated bite bar. This rig was implemented in an imaging study in which a cohort of mice were each scanned at multiple actuation frequencies. High driving frequencies decrease propagating shear wave wavelength, increasing elastography resolution, so potential pre-clinical use of MRE as a biomarker of disease and/or injury in the mouse model is a possibility with the test rig and methods developed.

Aim 3: Develop experimental capabilities to perform MR elastography in the living human brain and novel algorithms extract biomechanical information from these data.

Chapter 5 describes the modification and development of experimental procedures to conduct MRE in the human brain. Several data processing schemes were developed to assess the transmission of energy into the brain as well as the attenuation and reflection of shear waves inside the skull. A new viscoelastic inversion scheme was developed and used to extract tissue mechanical properties, using local frequency estimation of distortional wave fields. With a single spatial derivative, this method decouples contributions from longitudinal waves and rigid body motion using kinematics. The framework for anisotropic mechanical property estimation using DTI and MRE data was established in Chapter 2. Much of the data required to implement this routine in the human brain has been acquired (Chapter 6).

7.2 Limitations

While magnetic resonance elastography may provide unprecedented access to living intact tissues, its utility and accuracy are limited by important physical and computational constraints. A few of the difficulties encountered in completing this work are discussed here.

7.2.1 Imaging resolution and signal

MR imaging resolution determines the ability to resolve spatial wavelengths in elastography data, and thus limits bandwidth and accuracy. The Nyquist-Shannon sampling theorem applied to MRE data dictates that the shortest detectable wavelength is twice the largest voxel dimension. It is therefore advantageous to reduce the imaging voxel dimensions to increase spatial-frequency resolution. However, as voxel size is decreased, the NMR signal is also decreased. Signal loss can be compensated for by acquiring multiple averages (NMR excitations), at the expense of increasing scan duration. Elastography scans are already considered lengthy in comparison to other MR imaging modalities. At the limit, decreasing imaging voxel size is a losing battle due to the rapidly decreasing signal and gradient hardware limitations with present technology.

7.2.2 Wave propagation in viscoelastic media

In addition to the constraints of imaging resolution, material property estimates are limited by shear wave wavelength relative to the size of the anatomic feature of interest. It is desirable to have multiple shear waves in the region of interest to ensure wavelength estimates are accurate. As regions of interest become smaller, shear wave wavelengths must be shorter to maintain inversion accuracy. If biological media were purely elastic, an increase in driving frequency would result in a proportionally shorter wavelength. Nonetheless, tissue is viscoelastic. An increase in actuation frequency will increase the contribution of rate-dependent (viscous) stresses developed in the media, which creates two practical limitations. First, materials will appear to stiffen as the actuation frequency is increased, the wavelength will not proportionally decrease. Second, energy attenuation is increased so wave penetration depth is reduced. Both effects were encountered in these studies.

7.2.3 Isotropic viscoelastic inversion

Two different viscoelastic inversion methodologies were utilized in this work. Application of the correspondence principle permits local estimates of viscoelasticity without specifying particular a rheologic model, but direct inversion of the equations of motion requires two or more spatial derivatives. Numerical differentiation leads to increased uncertainty in modulus estimates, care must be taken when interpreting these results. This work follows the advice of Atay et al. [6] and utilizes a quantitative error metric to accept or reject local shear modulus estimates. Sometimes fewer estimates are reported, but those that are reported are more reliable.

Estimation based on local frequency estimation (LFE) circumvents issues attributable to numerical differentiation, but can be corrupted by rigid body and dilatational waves in displacement data. This type of error is remedied by applying LFE to the curl of the displacement field, which requires only a single spatial derivative in each direction. In extending this method to viscoelastic media, a particular rheologic model must be specified in advance. A Kelvin-Voigt material seems appropriate for studies conducted in the human brain, but this may not be the case for other tissues. The shear wave wavelength can be estimated locally; however, extraction of the attenuation parameter is challenging, if not impossible, in compact anatomical regions. Directionally filtering wave fields helps to isolate particular traveling wave components, but sensitivity in the extraction method increases uncertainty in shear modulus estimates. We recommend estimating local material properties from local wavelength estimates and a global attenuation constant. Finally, in this project a 2D LFE algorithm was used, and thus the assumption of wave propagation in a specific plane was required.

7.2.4 Wave interference and shadowing

Destructive wave interference and shadows in the wave field, created by inclusions or anatomic boundaries, are essentially a signal-to-noise issue, but one of a different nature. NMR signal intensity is not compromised, but wave motion can be nulled in regions by the way waves propagating in different directions interact with one another. Directional filters can be used to isolate wave propagation directions and mitigate

the wave cancellation effect, but phase artifacts induced by directional filters may overwhelm the true phase relationships in the response due to viscoelastic behavior. Such phase artifacts would thus compromise viscoelastic inversion based on the correspondence principle. Elastic inversion is still possible, but to estimate viscoelastic parameters, methods insensitive to local phase relationships must be explored (such as the LFE inversion scheme described above). In the future, use of non-simultaneous multi-source actuation schemes may reduce artifact caused by wave interference and shadowing.

7.2.5 Anisotropic inversion

Moving forward, perhaps the most challenging feat is anisotropic mechanical property reconstruction. Utilizing diffusion tensor images to identify structural properties of tissue reduces the uncertainty associated with aligning the material axis of symmetry in a transversely isotropic model. Nonetheless, activation of both shear moduli at every point in the medium is difficult in practice. Tissue displacements must occur in many directions and with sufficient amplitude to recover anisotropic material properties. Achieving this has so far proven difficult, and is likely to continue to be a challenge in estimating mechanical properties *in vivo*.

7.3 Future Directions

Despite its limitations and challenges, the future use of MRE as both a scientific measurement instrument and clinical diagnostic tool appear promising. A few of the many future directions for this work are identified here.

Elastography imaging protocols and analysis routines have been developed and applied in studies in isotropic phantoms and healthy mice and humans. Phantom validation studies should be extended to include those of anisotropic media. Future studies in mice and other small animals should focus on investigating tissue viscoelasticity as a marker of disease or injury. This could lead to new diagnostic tools with utility in therapeutic pharmaceutical drug development.

The mechanical properties of healthy living tissue remain incompletely characterized. Estimates of anisotropic material parameters remain an important goal. As actuation and imaging technologies become more sophisticated, the feasibility and efficiency of elastography measurements will increase, allowing better characterization of tissue viscoelasticity in smaller regions of interest with greater directional specificity.

7.4 Conclusion

Quantitative non-invasive measures of *in vivo* brain biomechanics are essential for understanding the basic science of traumatic brain injury. The data and methods described in this dissertation provide increased understanding of the structural-dynamic properties of the living brain. This work represents an important step toward understanding the mechanics of brain injury. The results increase our confidence in the ability of MRE to estimate viscoelastic material parameters, provide new insight into the constitutive behavior of brain tissue, and extend our understanding of how mechanical waves propagate into and throughout the human brain.

Appendix A

Local Least-squares Inversion

According to Equation 3.2, the components of the complex shear modulus can be determined from the displacement field and the corresponding Laplacian field, computed from finite difference approximations of the second spatial derivatives of the displacement field. In practice, noise in the displacement and Laplacian fields leads to errors in local estimates of the complex shear modulus. In ordinary least squares (OLS), it is assumed that there is no error in the measurement of the independent variable, i.e. the variance of the independent variable measurement error ϵ_η is zero. The variance in the error of measurements of the dependent variable ϵ_β is inferred from a “goodness-of-fit” metric. If there are measurement errors in both the independent and dependent variables, then the total least squares (TLS) method may provide a closer approximation to the values of G' and G'' than OLS. We implemented a TLS routine using singular value decomposition [45]. The variables were centered and scaled prior to fitting:

$$\hat{x} = \frac{(x - \bar{x})}{\sigma_x}; \quad \hat{y} = \frac{(y - \bar{y})}{\sigma_y}, \quad (\text{A.1})$$

where \bar{x} and \bar{y} are the mean values, σ_x and σ_y are the variances. \hat{x} and \hat{y} are the centered and scaled values of the independent and dependent variables x and y . The correlation coefficient r [103] can be computed directly from \hat{x} and \hat{y} , as

$$r = \frac{\text{cov}(\hat{x}, \hat{y})}{\sqrt{\hat{\sigma}_x \hat{\sigma}_y}}. \quad (\text{A.2})$$

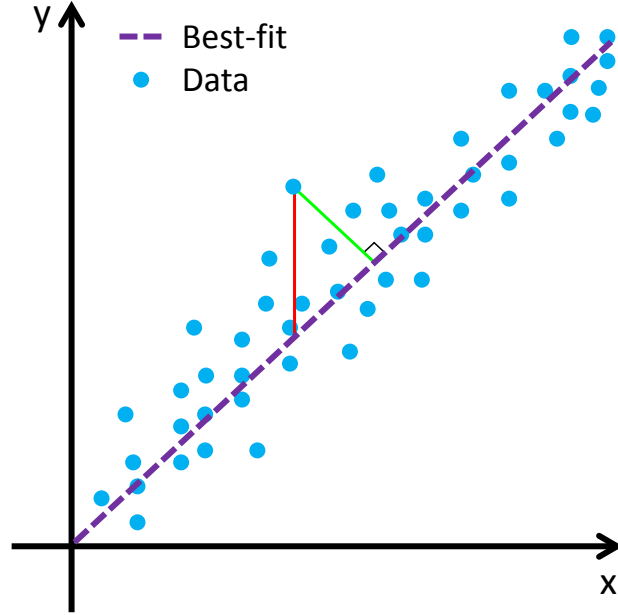


Figure A.1: The concept of total least squares versus ordinary least squares best-fit. Notice that error in both x and y are considered in a total least squares fit (green), $\lambda = 1$ in the case presented. Only error in y is considered in an ordinary least squares fit (red).

The variances $\hat{\sigma}_x$ and $\hat{\sigma}_y$ of the centered and scaled variables are unity, by definition. Hence, $r^2 = \text{cov}(\hat{x}, \hat{y})^2$. The normalized residual error (NRE) is defined as

$$NRE = \sqrt{1 - r^2}. \quad (\text{A.3})$$

The TLS procedure then calculates the maximum likelihood slope \hat{a}_1 by minimizing the perpendicular distances from the centered and scaled data points to line with intercept $\hat{a}_0 = 0$. The actual slope a_1 and intercept a_0 are found by transforming the scaled variables back to x and y . The variances in the un-scaled and scaled measurement errors are given by

$$\epsilon_\beta = \sum_{i=1}^N \frac{(x_i^* - x_i)^2}{N} = \sigma_\beta^2; \quad \epsilon_\eta = \sum_{i=1}^N \frac{(y_i^* - y_i)^2}{N} = \sigma_\eta^2 \quad (\text{A.4a})$$

$$\hat{\epsilon}_\beta = \frac{\sigma_\beta^2}{\sigma_x^2} = \sum_{i=1}^N \frac{(\hat{x}_i^* - \hat{x}_i)^2}{N}; \quad \hat{\epsilon}_\eta = \frac{\sigma_\eta^2}{\sigma_y^2} = \sum_{i=1}^N \frac{(\hat{y}_i^* - \hat{y}_i)^2}{N} = \sigma_\eta^2. \quad (\text{A.4b})$$

The TLS procedure minimizes the distances from \hat{x} and \hat{y} to the line $\hat{y}^* = \hat{a}_1 \hat{x}^*$ by satisfying

$$\frac{-1}{\hat{a}_1} = \frac{(\hat{y}_i^* - \hat{y}_i)}{(\hat{x}_i^* - \hat{x}_i)}. \quad (\text{A.5})$$

Re-arranging, then squaring and summing both sides shows the relation between $\hat{\epsilon}_\beta$ and $\hat{\epsilon}_\eta$ and the slope that is implicit in this TLS procedure

$$\frac{1}{(\hat{a}_1)^2} = \frac{\sum_{i=1}^N (\hat{y}_i^* - \hat{y}_i)^2}{\sum_{i=1}^N (\hat{x}_i^* - \hat{x}_i)^2} \quad (\text{A.6a})$$

$$\frac{1}{(\hat{a}_1)^2} = \frac{\hat{\epsilon}_\eta}{\hat{\epsilon}_\beta} \quad (\text{A.6b})$$

$$(\hat{a}_1)^2 = \frac{\hat{\epsilon}_\beta}{\hat{\epsilon}_\eta}. \quad (\text{A.6c})$$

Because both variables are centered and scaled, the magnitude of \hat{a}_1 will be unity, implying that $\hat{\epsilon}_\beta \hat{\epsilon}_\eta = 1$. This constrain can be removed by specifying an additional parameter λ [45]. If, after centering and scaling the data, \hat{y} is multiplied by λ , then Equations A.4b and A.5 become

$$\frac{-1}{\hat{a}_1} = \frac{\lambda(y_i^* - \hat{y}_i)}{(x_i^* - \hat{x}_i)} \quad \text{and} \quad \frac{\hat{\epsilon}_\beta}{\hat{\epsilon}_\eta} = \lambda(\hat{a}_1)^2 = \lambda. \quad (\text{A.7})$$

In our study, the Laplacian is the independent variable and is calculated by second-order numerical differentiation of the displacement fields. Hence, the Laplacian is relatively noisier than the displacement fields, so we expect $\lambda > 1$. This was verified by simulating outwardly propagating shear waves in a circular cylinder using our closed form solution (Equation 3.5). The simulated field was sampled at the same resolution as the MRE experiment and duplicated 11 times to represent 11 data slices (192 x 192 x 11). Gaussian noise was added to the data and λ was computed. The appropriate magnitude of λ depended on both the simulated noise level and the size of the Gaussian smoothing kernel. For noise amplitudes ranging from 0.05 to 0.25 times the prescribed displacement (u_{r_i} in the closed form solution) and smoothing kernel size from [5 x 5 x 3] to [13 x 13 x 7], the range of λ extended from 1.0 (low noise, large smoothing kernel) to 70 (higher noise, small smoothing kernel). Based on these simulations, we set $\lambda = 10$ when fitting experimental MRE data.

Appendix B

A Method to Temperature-correct Shear Moduli

When analyzing the viscoelastic shear modulus obtained from our MRE studies in gelatin, we observed that the modulus values were larger when a given frequency was tested early in a particular experiment. In addition, the measured moduli at 400 Hz were consistently higher than those at other frequencies. Since we had always tested the 400 Hz frequency first, this led us to suspect that the properties of the gelatin phantoms were changing during the experiment. Such changes were likely due to warming of the sample, partly due to heat transfer from the environment, and partly to “RF heating” from the MR pulse sequence. To verify our observations, we ran two additional MRE experiments where we held the actuation frequency constant at 400 Hz or 150 Hz and repeatedly acquired MRE data for up to six hours. The data was analyzed using the 3D direct inversion and 2D closed form methods using the same filter and fitting kernels as for the previous experiments. The values of G' and G'' decreased rapidly, then approached an equilibrium value after four to five hours. We fit the relative decrease in G' and G'' with time to decaying exponential functions:

$$a_0 \exp(-t/\tau_0) = G'/G'_{eq} - 1 \quad (\text{B.1a})$$

$$a_1 \exp(-t/\tau_1) = G''/G''_{eq} - 1. \quad (\text{B.1b})$$

Data were combined for both frequencies and fit to the exponential relation, obtaining constants of $a_0 = 1.00$ and $\tau_0 = 89$ minutes. G'' approached an equilibrium value faster than G' and decreased proportionately less ($a_1 = 0.71$ and $\tau_1 = 67$ minutes).

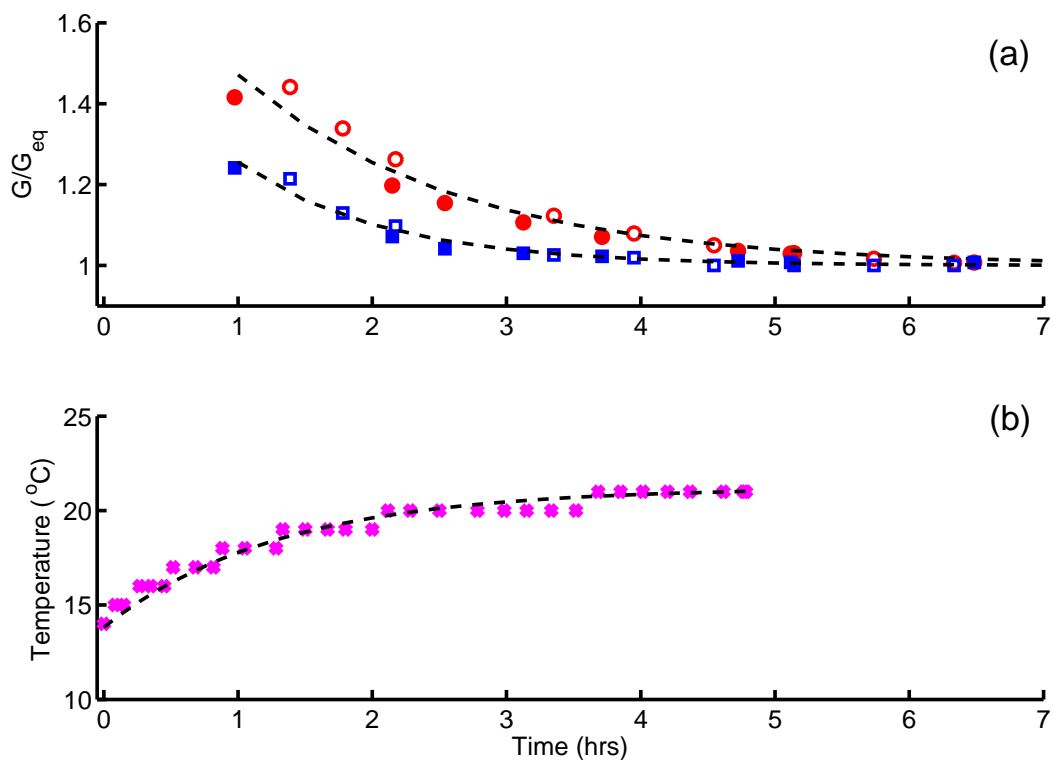


Figure B.1: (a) Normalized components of the viscoelastic shear moduli estimated from MRE displacement data at 150 Hz and 400 Hz taken over a period of 7 hours. Measurements of G'/G'_{eq} (circles) and G''/G''_{eq} (squares) are shown with open symbols (150 Hz) or filled symbols (400 Hz). Solid and dashed lines show decaying exponential function for G'/G'_{eq} and G''/G''_{eq} respectively, with parameters given in text. (b) Temperature measured using probe at center of another gel phantom. The gel reached an equilibrium temperature of 21 $^{\circ}\text{C}$ after 4 hours. Dashed line shows exponential fit to temperature with time constant of 1.3 hours. Adapted from [119].

In another experiment, a small temperature probe was inserted into the gelatin-glycerol mixture when cast and left in place during overnight refrigeration at 4°C. The phantom was then subjected to the typical MRE imaging protocol. (Imaging artifacts due to the temperature probe rendered these images useless for elastogram reconstruction.) The ambient temperature in the scanner room was $T_{\text{amb}} = 19^\circ\text{C}$. The gel temperature, T_{gel} , reached T_{amb} in two hours and reached an equilibrium temperature of 21°C after 4 hours. We also prepared another gel phantom under the same conditions and measured its temperature on the laboratory bench ($T_{\text{gel}} = 22^\circ\text{C}$). In this case, the gel temperature reached ambient temperature equilibrium in approximately 2 hours. From these data, we concluded that increase in gel temperature could explain the decrease in the shear moduli, and that the primary cause of the temperature increase was the ambient temperature with a smaller, secondary effect due possibly to RF heating. While the addition of glycerol to gelatin increases its melting temperature, there is a gradual decrease in G' and G'' below the melting temperature [69] which is consistent with our observations.

Appendix C

Design of an Actively-decoupled Transmit Volume Coil for Small Animal MRI

In the process of performing studies in the mouse, it became evident that the existing transmit coil could be improved. Figures [C.1-C.3](#) describe the design of a new coil built and subsequently donated to the Biomedical Magnetic Resonance Imaging Laboratory (BMRL). The structural and electrical components are described in [Table C.1](#).

For the existing coil, an open unsupported coil-form architecture and heavy use meant it suffered from reliability issues at times. This motivated a design improvement and was the purpose for building a new shielded transmit coil. The primary design goals: (i) reinforce the coil using rigid acrylic pipe as a coil-form; and (ii) reduce interference with the small animal MRE actuation rig. By increasing the transmit coil inner diameter, the coil could be placed outside of the acrylic tray holding the mouse. With the previous setup, the coil was placed inside of the tray holding the mouse. This was a bit cramped.

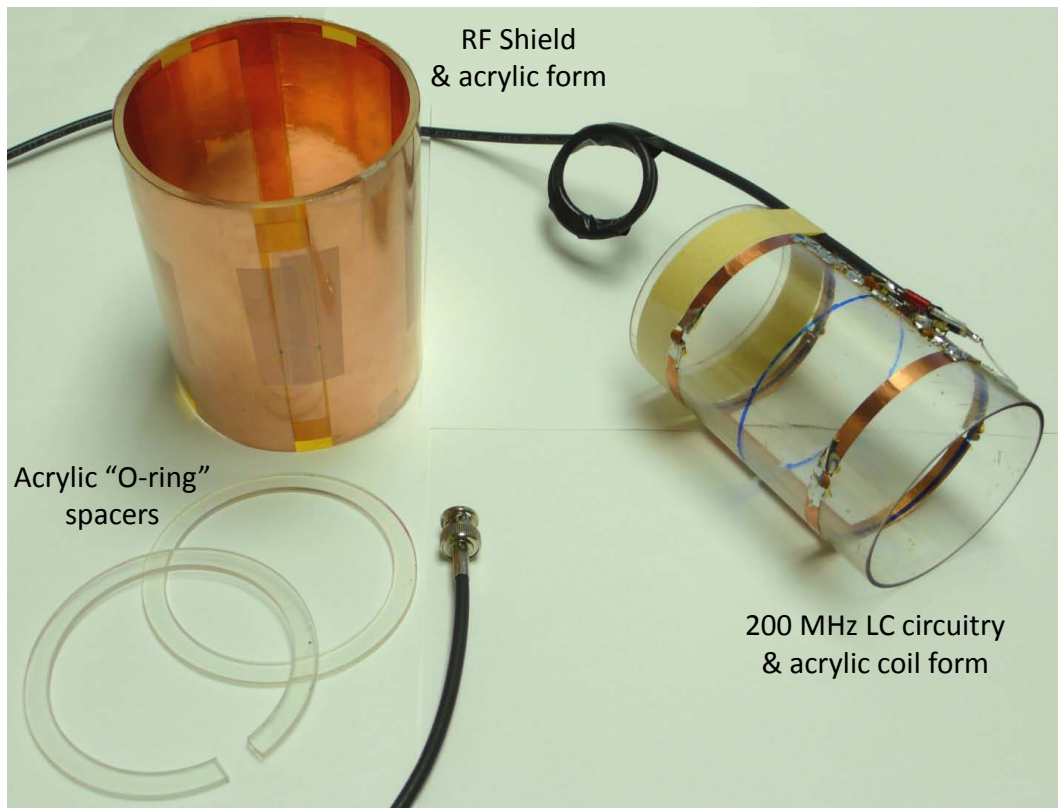


Figure C.1: Coil form components.

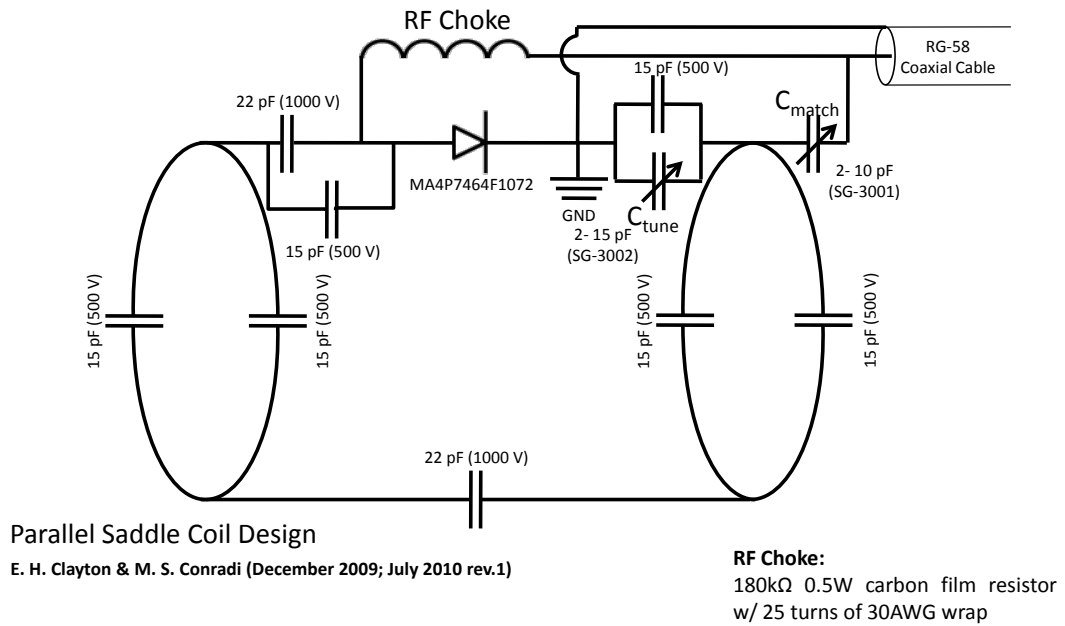


Figure C.2: Circuit diagram.

Table C.1: Bill of materials.

Item	Description
Acrylic tube (RF shield)	Clear cast, 4" O.D. x 3-3/4" I.D. x 1" L
Acrylic tube (RF coil)	Clear cast, 3-1/8" O.D. x 3" I.D. x 1" L
Copper foil tape (main bus)	1/2" x 18 yds
Copper foil tape (minor bus)	1/4" x 18 yds
Pin diode	MA4P7464F-1072T
Ceramic disc capacitor	22 pF, 1000V, non-magnetic
Ceramic disc capacitor	15 pF, 500V, non-magnetic
Variable capacitor (tune)	2-15 pF, 200V, $Q \geq 1000$ at 1MHz, 8 mm
Variable capacitor (match)	2-10 pF, 200V, $Q \geq 1000$ at 1MHz, 8 mm,



Figure C.3: The completed coil.

References

- [1] T. M. Abney, Y. Feng, R. Pless, R. J. Okamoto, G. M. Genin, and P. V. Bayly. Principal component analysis of dynamic relative displacement fields estimated from MR images. *PLoS One*, 6(7):e22063, 2011.
- [2] D. L. Anderson. Elastic wave propagation in layered anisotropic media. *J. Geophys. Res.*, 66(9):2953–2963, 1961.
- [3] K. B. Arbogast and S. S. Margulies. Material characterization of the brainstem from oscillatory shear tests. *J. Biomech.*, 31(9):801–807, 1998.
- [4] K. B. Arbogast, K. L. Thibault, B. S. Pinheiro, K. I. Winey, and S. S. Margulies. A high-frequency device for testing soft biological tissues. *J. Biomech.*, 30:757–759, 1997.
- [5] P. Asbach, D. Klatt, U. Hamhaber, J. Braun, R. Somasundaram, B. Hamm, and I. Sack. Assessment of liver viscoelasticity using multifrequency MR elastography. *Magn. Reson. Med.*, 60(2):373–379, 2008.
- [6] S. M. Atay, C. D. Kroenke, A. Sabet, and P. V. Bayly. Measurement of the dynamic shear modulus of mouse brain tissue in vivo by magnetic resonance elastography. *J. Biomech. Eng.*, 130(2):021013, 2008.
- [7] B. A. Auld. *Acoustic Fields and Waves in Solids*. R.E. Krieger, 1990.
- [8] A. C. Bain and D. F. Meaney. Tissue-level thresholds for axonal damage in an experimental model of central nervous system white matter injury. *J. Biomech. Eng.*, 122:615–622, 2000.
- [9] P. J. Basser and D. K. Jones. Diffusion-tensor MRI: theory, experimental design and data analysis - a technical review. *NMR Biomed.*, 15:456–467, 2002.
- [10] P. J. Basser, James Mattiello, and Denis LeBihan. Estimation of the effective self-diffusion tensor from the NMR spin echo. *J. Magnetic Resonance, Series B*, 103:247–254, 1994.
- [11] P. J. Basser, James Mattiello, and Denis LeBihan. MR diffusion tensor spectroscopy and imaging. *Biophysical Journal*, 66:259–267, 1994.
- [12] P. J. Basser and C. Pierpaoli. Microstructural and physiological features of tissues elucidated by quantitative-diffusion-tensor MRI. *J. Magn. Reson. B*, 111(3):209–219, 1996.

- [13] T. Baumberger, C. Caroli, and D. Martina. Solvent control of crack dynamics in a reversible hydrogel. *Nat. Mater.*, 5:552–555, 2006.
- [14] P. V. Bayly, E. E. Black, R. C. Pedersen, E. P. Leister, and G. M. Genin. In vivo imaging of rapid deformation and strain in an animal model of traumatic brain injury. *J. Biomech.*, 39(6):1086–1095, 2006.
- [15] P. V. Bayly, T. S. Cohen, E. P. Leister, D. Ajo, E. C. Leuthardt, and G. M. Genin. Deformation of the human brain induced by mild acceleration. *J. Neurotrauma*, 22(8):845–856, 2005.
- [16] P. V. Bayly, K. T. Dikranian, E. E. Black, C. Young, Y.-Q. Qin, J. Labruyere, and J. W. Olney. Spatiotemporal evolution of apoptotic neurodegeneration following traumatic injury to the developing rat brain. *Brain Research*, 1107(1):70–81, 2006.
- [17] P. V. Bayly, P. G. Massouros, E. Christoforou, A. Sabet, and G. M. Genin. Magnetic resonance measurement of transient shear wave propagation in a viscoelastic gel cylinder. *J. Mech. Phys. Solids*, 56(5):2036–2049, 2008.
- [18] A. I. Beltzer. *Acoustics of Solids*. Springer-Verlag, 1988.
- [19] D. S. Berry. Stress propagation in visco-elastic bodies. *J. Mech. Phys. Solids*, 6:177–185, 1958.
- [20] A. F. Bower. *Applied Mechanics of Solids*. CRC Press, 2009.
- [21] J. Braun, G. Buntkowsky, J. Bernarding, T. Tolxdorff, and I. Sack. Simulation and analysis of magnetic resonance elastography wave images using coupled harmonic oscillators and gaussian local frequency estimation. *Magn. Reson. Imaging*, 19(5):703–713, 2001.
- [22] P. Chadwick. Wave propagation in transversely isotropic elastic media. I. Homogeneous plane waves. *Proc. R. Soc. Lond. A*, 422:23–66, 1989.
- [23] Q. C. Chan, G. Li, R. L. Ehman, R. C. Grimm, R. Li, and E. S. Yang. Needle shear wave driver for magnetic resonance elastography. *Magn. Reson. Med.*, 55(5):1175–1179, 2006.
- [24] S. Chatelin, A. Constantinesco, and R. Willinger. Fifty years of brain tissue mechanical testing: from in vitro to in vivo investigations. *Biorheology*, 47(5-6):255–276, 2010.
- [25] Q. Chen, S. I. Ringleb, A. Manduca, R. L. Ehman, and K. N. An. A finite element model for analyzing shear wave propagation observed in magnetic resonance elastography. *J. Biomech.*, 38(11):2198–2203, 2005.

- [26] R. Chopra, A. Arani, Y. Huang, M. Musquera, J. Wachsmuth, M. Bronskill, and D. Plewes. In vivo MR elastography of the prostate gland using a transurethral actuator. *Magn. Reson. Med.*, 62(3):665–671, 2009.
- [27] E. H. Clayton and P. V. Bayly. Brain response to extracranial acoustic loads: Shear wave propagation characterized by vector fields. In *ASME International Mechanical Engineering Congress and Exposition*, 2011.
- [28] E. H. Clayton, J. R. Garbow, and P. V. Bayly. Frequency dependence of mouse brain tissue stiffness measured in vivo with MR elastography. In *International Society for Magnetic Resonance in Medicine Annual Conference*, 2010.
- [29] E. H. Clayton, J. R. Garbow, and P. V. Bayly. Frequency-dependent viscoelastic parameters of mouse brain tissue estimated by MR elastography. *Phys. Med. Biol.*, 56(8):2391–2406, 2011.
- [30] E. H. Clayton, G. M. Genin, and P. V. Bayly. Transmission, attenuation, and reflection of shear waves in the human brain. *J. R. Soc. Interface*, Under Review:xx, 2012.
- [31] E. H. Clayton, Q. Wang, and S. K. Song P. V. Bayly. Non-invasive measurement of vitreous humor stiffness in the mouse using MR elastography. In *International Society for Magnetic Resonance in Medicine Annual Conference*, 2010.
- [32] J. Crank. *The Mathematics of Diffusion*. Oxford University Press, 1956.
- [33] E. Diguët, E. van Houten, M. Green, and R. Sinkus. High resolution MR-elastography mouse brain study: towards a mechanical atlas. In *International Society for Magnetic Resonance in Medicine*, 2009.
- [34] M. M. Doyley, Q. Feng, J. B. Weaver, and K. D. Paulsen. Performance analysis of steady-state harmonic elastography. *Phys. Med. Biol.*, 52:2657–2674, 2007.
- [35] M. M. Doyley, I. Perreard, A. J. Patterson, J. B. Weaver, and K. M. Paulsen. The performance of steady-state harmonic magnetic resonance elastography when applied to viscoelastic materials. *Med. Phys.*, 37(8):3970–3979, 2010.
- [36] M. M. Doyley, J. B. Weaver, E. E. Van Houten, F. E. Kennedy, and K. D. Paulsen. Thresholds for detecting and characterizing focal lesions using steady-state MR elastography. *Med. Phys.*, 30(4):495–504, 2003.
- [37] T. Elgeti, J. Rump, U. Hamhaber, S. Papazoglou, B. Hamm, J. Braun, and I. Sack. Cardiac magnetic resonance elastography - initial results. *Investigative Radiology*, 43(11):762–772, 2008.

- [38] M. Faul, L. Xu, M. Wald, and V. Coronado. Traumatic brain injury in the united states: Emergency department visits and hospitalizations and deaths 2002-2006. Technical report, US Centers for Disease Control and Prevention, 2010.
- [39] Y. Feng, T. M. Abney, R. J. Okamoto, R. B. Pless, G. M. Genin, and P. V. Bayly. Relative brain displacement and deformation during constrained mild frontal head impact. *J. R. Soc. Interface*, 7(53):1677–1688, 2010.
- [40] J. D. Ferry. *Viscoelastic Properties of Polymers*. Wiley, 1980.
- [41] W. Flügge. *Viscoelasticity*. Springer-Verlag, 1975.
- [42] J. R. Garbow, C. McIntosh, and M. S. Conradi. Actively decoupled transmit-receive coil-pair for mouse brain MRI. *Concepts Magn. Reson.*, 33B(4):252–259, 2008.
- [43] D. M. Geddes, R. S. Cargill, and M. C. LaPlaca. Mechanical stretch to neurons results in a strain rate and magnitude-dependent increase in plasma membrane permeability. *J. Neurotrauma*, 20:1039–1049, 2003.
- [44] A. Gefen and S. S. Margulies. Are in vivo and in situ brain tissues mechanically similar? *J. Biomech.*, 37:1339–1352, 2004.
- [45] G. H. Golub and C. F. Van Loan. An analysis of the total least-squares problem. *SIAM J. Numer. Anal.*, 17:883–893, 1980.
- [46] D. I. Graham, J. H. Adams, J. A. Nicoll, W. L. Maxwell, and T. A. Gennarelli. The nature, distribution and causes of traumatic brain injury. *Brain Pathol.*, 5(4):397–406, 1995.
- [47] M. Grediac, E. Toussaint, and F. Pierron. Special virtual fields for the direct determination of material parameters with the virtual fields method. 1–Principle and definition. *Int. J. Solids Struct.*, 39:2691–2705, 2002.
- [48] M. Grediac, E. Toussaint, and F. Pierron. Special virtual fields for the direct determination of material parameters with the virtual fields method. 2–Application to in-plane properties. *Int. J. Solids Struct.*, 39:2707–2730, 2002.
- [49] M. A. Green, L. E. Bilston, and R. Sinkus. In vivo brain viscoelastic properties measured by magnetic resonance elastography. *NMR in Biomed*, 21(7):755–764, 2008.
- [50] J. L. Griffith, J. S. Shimony JS, S. A. Cousins, S. E. Rees, D. C. McCurnin, T. E. Inder, and J. J. Neil. MR imaging correlates of white-matter pathology in a preterm baboon model. *Pediatr. Res.*, 71(2):185–191, 2012.

- [51] R. C. Grimm, D. S. Lake, A. Manduca, and R. L. Ehman. MRE / Wave. Computer Program, 2006.
- [52] W. Hackbusch. *Multi-grid Methods and Applications*. Springer-Verlag, 1985.
- [53] T.J. Hall, M. Bilgen, M.F. Insana, and T.A. Krouskop. Phantom materials for elastography. *IEEE Trans. Ultrason., Ferroelectr., Freq. Control*, 44:1355–1365, 1997.
- [54] U. Hamhaber, F. A. Grieshaber, J. H. Nagel, and U. Klose. Comparison of quantitative shear wave MR-elastography with mechanical compression tests. *Magn. Reson. Med.*, 49(1):71–77, 2003.
- [55] U. Hamhaber, D. Klatt, S. Papazoglou, M. Hollmann, J. Stadler, I. Sack, J. Bernarding, and J. Braun. In vivo magnetic resonance elastography of human brain at 7 T and 1.5 T. *J. Magn. Reson. Imaging*, 32(3):577–83, 2010.
- [56] U. Hamhaber, I. Sack, S. Papazoglou, J. Rump, D. Klatt, and J. Braun. Three-dimensional analysis of shear wave propagation observed by in vivo magnetic resonance elastography of the brain. *Act Biomater*, 3(1):127–137, 2007.
- [57] W. N. Hardy, C. D. Foster, M. J. Mason, K. H. Yang, A. I. King, and S. Tashman. Investigation of head injury mechanisms using neutral density technology and high-speed biplanar X-ray. *Stapp Car Crash J.*, 45:337–368, 2001.
- [58] W. N. Hardy, M. J. Mason, C. D. Foster, C. S. Shah, J. M. Kopacz, K. H. Yang, A. I. King, J. Bishop, M. Bey, W. Anderst, and S. Tashman. A study of the response of the human cadaver head to impact. *Stapp Car Crash J.*, 51:17–80, 2007.
- [59] D. Head, R. L. Buckner, J. S. Shimony, L. E. Williams, E. Akbudak, T. E. Conturo, M. McAvoy, J. C. Morris, and A. Z. Snyder. Differential vulnerability of anterior white matter in nondemented aging with minimal acceleration in dementia of the Alzheimer type: evidence from diffusion tensor imaging. *Cereb. Cortex*, 14(4):410–423, 2004.
- [60] A. H. Henni, C. Schmitt, and G. Cloutier. Shear wave induced resonance elastography of soft heterogeneous media. *J. Biomech.*, 43:1488–1493, 2010.
- [61] J. Ho and S. Kleiven. Dynamic response of the brain with vasculature: a three-dimensional computational study. *J. Biomech.*, 40(13):3006–12, 2007.
- [62] C. W. Hoge, D. McGurk, J. L. Thomas, A. L. Cox, C. C. Engel, and C. A. Castro. Mild traumatic brain injury in U.S. soldiers returning from Iraq. *N. Engl. J. Med.*, 358(5):453–463, 2008.

- [63] A. H. S. Holbourn. Mechanics of head injuries. *Lancet*, 242(6267):438–441, 1943.
- [64] M. Hrapko, J. A. van Dommelen, G. W. Peters, and J. S. Wismans. The influence of test conditions on characterization of the mechanical properties of brain tissue. *J. Biomech. Eng.*, 130(3):031003, 2008.
- [65] N. G. Ibrahim, R. Natesh, S. E. Szczesny, K. Ryall, S. A. Eucker, B. Coats, and S. S. Margulies. In situ deformations in the immature brain during rapid rotations. *J. Biomech. Eng.*, 132(4):044501, 2010.
- [66] B. Morrison III, B. S. Elkin, J.-P. Dollé, and M. L. Yarmush. In vitro models of traumatic brain injury. *Ann. Rev. Biomed. Eng.*, 13:91–126, 2011.
- [67] B. Morrison III, D. F. Meaney, S. S. Margulies, and T. K. McIntosh. Dynamic mechanical stretch of organotypic brain slice cultures induces differential genomic expression: relationship to mechanical parameters. *J. Biomech. Eng.*, 122:224–230, 2000.
- [68] S. Ji, Z. Wu, A. Hartov, D. W. Roberts, and K. D. Paulsen. Mutual-information-based image to patient re-registration using intraoperative ultrasound in image-guided neurosurgery. *Med. Phys.*, 35(10):4612–24, 2008.
- [69] C. C. Joly-Duhamel. All gelatin networks: 2. The master curve for elasticity. *Langmuir*, 18:7158–7166, 2002.
- [70] J. Kemper, R. Sinkus, J. Lorenzen, C. Nolte-Ernsting, A. Stork, and G. Adam. MR elastography of the prostate: initial in-vivo application. *RöFo - Fortschritte auf dem Gebiet der Röntgenstrahlen und der bildgebenden Verfahren*, 176(08):1094–1099, 2004.
- [71] D. Klatt, C. Friedrich, Y. Korth, R. Vogt, J. Braun, and I. Sack. Viscoelastic properties of liver measured by oscillatory rheometry and multifrequency magnetic resonance elastography. *Biorheology*, 47:133–141, 2010.
- [72] D. Klatt, U. Hamhaber, P. Asbach, J. Braun, and I. Sack. Noninvasive assessment of the rheological behavior of human organs using multifrequency MR elastography: a study of brain and liver viscoelasticity. *Phys. Med. Biol.*, 52(24):7281–7294, 2007.
- [73] D. Klatt, S. Papazoglou, J. Braun, and I. Sack. Viscoelasticity-based MR elastography of skeletal muscle. *Phys. Med. Biol.*, 55:6445–6459, 2010.
- [74] E. C. Klawiter, J. Xu, R. T. Naismith, T. L. Benzinger, J. S. Shimony, S. Lancia, A. Z. Snyder, K. Trinkaus, S.K. Song, and A. H. Cross. Increased radial diffusivity in spinal cord lesions in neuromyelitis optica compared to multiple sclerosis. *Mult. Scler.*, page epub ahead of print, 2012.

- [75] S. Kleiven and W. N. Hardy. Correlation of an FE model of the human head with local brain motion - consequences for injury prediction. *Stapp Car Crash J.*, 46:123–144, 2002.
- [76] H. Knutsson, C. F. Westin, and G. H. Granlund. Local multiscale frequency and bandwidth estimation. In *Proceedings of the IEEE International Conference on Image Processing*, pages 36–40, 1994.
- [77] R. C. Koeller. Applications of fractional calculus to the theory of viscoelasticity. *J. Appl. Mech.-T ASME*, 51:299, 1984.
- [78] M. Kohandel, S. Sivaloganathan, G. Tenti, and K. Darvish. Frequency dependence of complex moduli of brain tissue using a fractional zener model. *Phys. Med. Biol.*, 50:2799–2805, 2005.
- [79] A. Kolipaka, P. A. Araoz, K. P. McGee, A. Manduca, and R. L. Ehman. Magnetic resonance elastography as a method for the assessment of effective myocardial stiffness throughout the cardiac cycle. *Magn. Reson. Med.*, 64(3):862–870, 2010.
- [80] H. Kolsky. *Stress Waves in Solids*. Dover Publications, 1963.
- [81] S. A. Kruse, G. H. Rose, K. J. Glaser, A. Manduca, J. P. Felmlee, C. R. Jack, Jr., and R. L. Ehman. Magnetic resonance elastography of the brain. *NeuroImage*, 39(1):231–237, 2008.
- [82] S. A. Kruse, J. A. Smith, A. J. Lawrence, M. A. Dresner, A. Manduca, J. F. Greenleaf, and R. L. Ehman. Tissue characterization using magnetic resonance elastography: preliminary results. *Phys. Med. Biol.*, 45(6):1579–1590, 2000.
- [83] L. D. Landau, E. M. Lifshitz, A. M. Kosevich, and L. P. Pitaevskii. *Theory of Elasticity*. Pergamon Press, 1986.
- [84] C. Lauret, M. Hrapko, J. A. W. van Dommelen, G. W. M. Peters, and J. S. H. M. Wismans. Optical characterization of acceleration-induced strain fields in inhomogeneous brain slices. *Med. Eng. Phys.*, 31:392–399, 2009.
- [85] D. V. Litwiller, S. J. Lee, A. Kolipaka, Y. K. Mariappan, K. J. Glaser, J. S. Pulido, and R. L. Ehman. MR elastography of the ex vivo bovine globe. *J. Magn. Reson. Imaging*, 32(1):44–51, 2010.
- [86] F. J. Lockett. *Nonlinear Viscoelastic Solids*. Academic Press, 1972.
- [87] A. E. H. Love. *A Treatise on the Mathematical Theory of Elasticity*. Dover, 4th edition, 1944.

- [88] C. L. Mac Donald, A. M. Johnson, D. Cooper, E. C. Nelson, N. J. Werner, J. S. Shimony, A. Z. Snyder, M. E. Raichle, J. R. Witherow, R. Fang, S. F. Flaherty, and D. L. Brody. Detection of blast-related traumatic brain injury in u.s. military personnel. *N. Engl. J. Med.*, 364(22):2091–2100, 2011.
- [89] E. L. Madsen, G. R. Frank, M. A. Hobson, S. Lin Gibson, T. J. Hall, J. Jiang, and T. A. Stiles. Instrument for determining the complex shear modulus of soft-tissue-like materials from 10 to 300 Hz. *Phys. Med. Biol.*, 53(19):5313–5342, 2008.
- [90] A. Manduca, T. E. Oliphant, M. A. Dresner, J. L. Mahowald, S. A. Kruse, E. Amromin, J. P. Felmlee, J. F. Greenleaf, and R. L. Ehman. Magnetic resonance elastography: non-invasive mapping of tissue elasticity. *Med. Image Anal.*, 5(4):237–254, 2001.
- [91] S. S. Margulies and D. F. Meaney. *Handbook of Biomaterials Properties*. London: Chapman & Hall, 1998.
- [92] S. S. Margulies and L. E. Thibault. A proposed tolerance criterion for diffuse axonal injury in man. *J. Biomech.*, 25:917–923, 1992.
- [93] S. S. Margulies, L. E. Thibault, and T. A. Gennarelli. Physical model simulations of brain injury in the primate. *J. Biomech.*, 23(8):823–836, 1990.
- [94] P. G. Massouros and G. M. Genin. The steady-state response of a maxwell viscoelastic cylinder to sinusoidal oscillation of its boundary. *Proc. R. Soc. Lond. Ser. A*, 464:207–221, 2008.
- [95] J. Mattiello, P. J. Basser, and D. LeBihan. Analytical expressions for the b matrix in NMR diffusion imaging and spectroscopy. *J. Magn. Reson. A*, 109:131–141, 1994.
- [96] R. Mayeux, R. Ottman, M. X. Tang, L. Noboa-Bauza, K. Marder, B. Gurland, and Y. Stern. Genetic susceptibility and head injury as risk factors for alzheimer’s disease among community-dwelling elderly persons and their first-degree relatives. *Ann. Neurol.*, 33(5):494–501, 1993.
- [97] P. J. McCracken, A. Manduca, J. Felmlee, and R. L. Ehman. Mechanical transient-based magnetic resonance elastography. *Magn. Reson. Med.*, 53(3):628–639, 2005.
- [98] P. J. McCracken, A. Manduca, J. P. Felmlee, and R. L. Ehman. Transient-based MR elastography of the brain. In *International Society for Magnetic Resonance Imaging in Medicine*, page 799, 2004.

- [99] P. J. McCracken, A. Manduca, J. P. Felmlee, and R. L. Ehman. Transient MR elastography: modeling traumatic brain injury. In *International Conference on Medical Image Computing and Computer Assisted Intervention (MICCAI)*, pages 1081–1082, 2004.
- [100] M. D. McGarry, E. E. Van Houten, P. R. Perrinez, A. J. Pattison, J. B. Weaver, and K. D. Paulsen. An octahedral shear strain-based measure of SNR for 3D MR elastography. *Phys. Med. Biol.*, 56(13):N153–164, 2011.
- [101] D. F. Meaney, D. H. Smith, D. I. Shreiber, A. C. Bain, R. T. Miller, D. T. Ross, and T. A. Gennarelli. Biomechanical analysis of experimental diffuse axonal injury. *J. Neurotrauma*, 12(4):689–694, 1995.
- [102] D.F. Meaney, D. H. Smith, D. I. Shreiber, A. C. Bain, R. T. Miller RT, and et al. Biomechanical analysis of experimental diffuse axonal injury. *J. Neurotrauma*, 12:689–694, 1995.
- [103] W. Mendenhall. *Introduction to Probability and Statistics*. Duxbury Press, 1983.
- [104] M. I. Miga, K. D. Paulsen, J. M. Lemery, S. D. Eisner, A. Hartov, F. E. Kennedy, and D. W. Roberts. Model-updated image guidance: initial clinical experiences with gravity-induced brain deformation. *IEEE Trans. Med. Imaging*, 18(10):866–874, 1999.
- [105] M. I. Miga, T. K. Sinha, D. M. Cash, R. L. Galloway, and R. J. Weil. Cortical surface registration for image-guided neurosurgery using laser-range scanning. *IEEE Trans. Med. Imaging*, 22(8):973–985, 2003.
- [106] K. Miller. Constitutive model of brain tissue suitable for finite element analysis of surgical procedures. *J. Biomech.*, 32(5):531–537, 1999.
- [107] K. Miller and K. Chinzei. Mechanical properties of brain tissue in tension. *J. Biomech.*, 35:483–490, 2002.
- [108] K. Miller, K. Chinzei, G. Orsengo, and P. Bednarz. Mechanical properties of brain tissue in-vivo: experiment and computer simulation. *J. Biomech.*, 33(11):1369–1376, 2000.
- [109] J. A. Mortimer, C. M. van Duijn, V. Chandra, L. Fratiglioni, A. B. Graves, A. Heyman, A. F. Jorm, E. Kokmen, K. Kondo, W. A. Rocca, and et al. Head trauma as a risk factor for Alzheimer’s disease: a collaborative re-analysis of case-control studies. EURODEM Risk Factors Research Group. *Int. J. Epidemiol.*, 20 Suppl. 2:S28–35, 1991.

- [110] M. C. Murphy, G. L. Curran, K. J. Glaser, P. J. Rossman, J. Huston, J. F. Poduslo, C. R. Jack, J. P. Felmlee, and R. L. Ehman. MR elastography of the brain in a mouse model of Alzheimer’s disease. In *International Society for Magnetic Resonance in Medicine*, 2010.
- [111] R. Muthupillai and R. L. Ehman. Magnetic resonance elastography. *Nat. Med.*, 2(5):601–603, 1996.
- [112] R. Muthupillai, D. J. Lomas, P. J. Rossman, J. F. Greenleaf, A. Manduca, and R. L. Ehman. Magnetic resonance elastography by direct visualization of propagating acoustic strain waves. *Science*, 269(5232):1854–1857, 1995.
- [113] R. Muthupillai, P. J. Rossman, D. J. Lomas, J. F. Greenleaf, S. J. Riederer, and R. L. Ehman. Magnetic resonance imaging of transverse acoustic strain waves. *Magn. Reson. Med.*, 36(2):266–274, 1996.
- [114] A. Nahum, R. Smith, and C. Ward. Intracranial pressure dynamics during head impact. In *Proc. 21st Stapp Car Crash Conference*, 1977.
- [115] M. Neeman, J. P. Freyer, and L. O. Sillerud. A simple method for obtaining cross-term-free images for diffusion anisotropy studies in NMR microimaging. *J. Geophys. Res.*, 21(1):138–143, 1991.
- [116] J. R. Nixon, P. P. Georgakopoulos, and J. E. Carless. The rigidity of gelatin-glycerin gels. *J. Pharm. Pharmacol.*, 18:283–288, 1966.
- [117] M. K. Nyein, A. M. Jason, L. Yu, C. M. Pita, J. D. Joannopoulos, D. F. Moore, and R. A. Radovitzky. In silico investigation of intracranial blast mitigation with relevance to military traumatic brain injury. *Proc. Natl. Acad. Sci. USA*, 107(48):20703–20708, 2010.
- [118] M. O’Donell, E. T. Jaynes, and J. G. Miller. Kramers–Kronig relationship between ultrasonic attenuation and wave velocity. *J. Acoust. Soc. Am.*, 69:696–701, 1981.
- [119] R. J. Okamoto, E. H. Clayton, and P. V. Bayly. Viscoelastic properties of soft gels: comparison of magnetic resonance elastography and dynamic shear testing in the shear wave regime. *Phys. Med. Biol.*, 56(19):6379–6400, 2011.
- [120] A. V. Oppenheim and R. W. Schaffer. *Digital Signal Processing*. Englewood Cliffs, NJ: Prentice Hall, 1975.
- [121] J. Oudry, J. Chen, K. J. Glaser, V. Miette, L. Sandrin, and R. L. Ehman. Cross-validation of magnetic resonance elastography and ultrasound-based transient elastography: a preliminary phantom study. *J. Magn. Reson. Imaging*, 30(5):1145–1150, 2009.

- [122] S. Papazoglou, U. Hamhaber, J. Braun, and I. Sack. Algebraic helmholtz inversion in planar magnetic resonance elastography. *Phys. Med. Biol.*, 53(12):3147–3158, 2008.
- [123] A. J. Pattison, S. S. Lollis, P. R. Perriñez, I. M. Perreard, M. D. McGarry, J. B. Weaver, and K. D. Paulsen. Time-harmonic magnetic resonance elastography of the normal feline brain. *J. Biomech.*, 43(14):2747–2752, 2010.
- [124] E.J. Pellman, D.C. Viano, A.M. Tucker, I.R. Casson, and J.F. Waeckerle. Concussion in professional football: reconstruction of game impacts and injuries. *Neurosurgery*, 53:799–812, 2003.
- [125] I. M. Perreard, A. J. Pattison, M. Doyley, M. D. McGarry, Z. Barani, E. E. Van Houten, J. B. Weaver, and K. D. Paulsen. Effects of frequency- and direction-dependent elastic materials on linearly elastic MRE image reconstructions. *Phys. Med. Biol.*, 55(22):6801–6815, 2010.
- [126] D. Plewes, J. Bishop, A. Samani, and J. Sciarretta. Visualization and quantification of breast cancer biomechanical properties with magnetic resonance elastography. *Phys. Med. Biol.*, 45(6):1591–1610, 2000.
- [127] B. P. Poncelet, V. J. Wedeen, R. M. Weisskoff, and M. S. Cohen. Brain parenchyma motion: measurement with cine echo-planar MR imaging. *Radiology*, 185(3):645–651, 1992.
- [128] M. T. Prange and S. S. Margulies. Regional and directional and age-dependent properties of the brain undergoing large deformation. *J. Biomech. Eng.*, 124(2):244–252, 2002.
- [129] T. Pritz. Verification of local Kramers-Kronig relations for complex modulus by means of fractional derivative model. *J. Sound Vibrat.*, 228(5):1145–1165, 1999.
- [130] R. H. Pudenz and C. H. Shelden. The lucite calvarium—a method for direct observation of the brain. II. Cranial trauma and brain movement. *J. Neurosurg.*, 3:487–505, 1946.
- [131] W. T. Read. *Stress Analysis for Compressible Viscoelastic Materials*. AIP, 1950.
- [132] T. G. Reese, D. A. Feinberg, J. Dou, and V. J. Wedeen. Phase contrast MRI of myocardial 3D strain by encoding contiguous slices in a single shot. *Magn. Reson. Med.*, 47:665–676, 1992.
- [133] K. Riek, D. Klatt, H. Nuzha, S. Mueller, U. Neumann, I. Sack, and J. Braun. Wide-range dynamic magnetic resonance elastography. *J. Biomech.*, 44(7):1380–1386, 2011.

- [134] S. I. Ringleb, Q. Chen, D. S. Lake, A. Manduca, R. L. Ehman, and K.-N. An. Quantitative shear wave magnetic resonance elastography: comparison to a dynamic shear material test. *Magn. Reson. Med.*, 53(5):1197–1201, 2005.
- [135] B. Robert, R. Sinkus, J.-L. Gennisson, and M. Fink. Application of DENSE-MR-elastography to the human heart. *Magn. Reson. Med.*, 62(5):1155–1163, 2009.
- [136] A. J. Romano, P. B. Abraham, P. J. Rossman, J. A. Bucaro, and R. L. Ehman. Determination and analysis of guided wave propagation using magnetic resonance elastography. *Magn. Reson. Med.*, 54(4):893–900, 2005.
- [137] A. J. Romano, M. Scheel, S. Hirsch, J. Braun, and I. Sack. In vivo waveguide elastography of white matter tracts in the human brain. *Magn. Reson. Med.*, page epub ahead of print, 2012.
- [138] A. J. Romano, J. J. Shirron, and J. A. Bucaro. On the noninvasive determination of material parameters from a knowledge of elastic displacements theory and numerical simulation. *IEEE Trans. Ultrason., Ferroelectr., Freq. Control*, 45(3):751–759, 1998.
- [139] O. Rouvière, M. Yin, M. A. Dresner, P. J. Rossman, L. J. Burgart, J. L. Fidler, and R. L. Ehman. MR elastography of the liver: preliminary results. *Radiology*, 240(2):440–448, 2006.
- [140] A. A. Sabet, E. Christoforou, B. Zatlin, G. M. Genin, and P. V. Bayly. Deformation of the human brain induced by mild angular head acceleration. *J. Biomech.*, 41(2):307–315, 2008.
- [141] I. Sack, B. Beierbach, U. Hamhaber, D. Klatt, and J. Braun. Non-invasive measurement of brain viscoelasticity using magnetic resonance elastography. *NMR Biomed.*, 21(3):265–271, 2008.
- [142] I. Sack, B. Beierbach, J. Wuerfel, D. Klatt, U. Hamhaber, S. Papazoglou, P. Martus, and J. Braun. The impact of aging and gender on brain viscoelasticity. *NeuroImage*, 46(3):652–657, 2009.
- [143] I. Sack, J. Rump, T. Elgeti, A. Samani, and J. Braun. MR elastography of the human heart: noninvasive assessment of myocardial elasticity changes by shear wave amplitude variations. *Magn. Reson. Med.*, 61(3):668–677, 2009.
- [144] M. H. Sadd. *Elasticity: Theory, Applications, and Numerics*. Elsevier Inc., 2005.
- [145] R. A. Schapery. A method of viscoelastic stress analysis using elastic solutions. *J. Franklin Institute*, 279(4):268–289, 1965.

- [146] K. Schregel, E. Wuerfel, J. Wuerfel, D. Petersen, and R. Sinkus. Viscoelastic properties change at an early stage of cuprizone induced affection of oligodendrocytes in the corpus callosum of c57/black6 mice. In *International Society for Magnetic Resonance in Medicine*, 2010.
- [147] N. A. Shaw. The neurophysiology of concussion. *Prog. Neurobiol.*, 67(4):281–344, 2002.
- [148] L.Z. Shuck and S.H. Advani. Rheological response of human brain-tissue in shear. *J. Basic Eng.*, 94:905–911, 1972.
- [149] R. Sinkus, J. Lorenzen, D. Schrader, M. Lorenzen, M. Dargatz, and D. Holtz. High-resolution tensor MR elastography for breast tumour detection. *Phys. Med. Biol.*, 45(6):1649–1664, 2000.
- [150] R. Sinkus, K. Siegmann, T. Xydeas, M. Tanter, C. Claussen, and M. Fink. MR elastography of breast lesions: understanding the solid/liquid duality can improve the specificity of contrast-enhanced MR mammography. *Magn. Reson. Med.*, 58(6):1135–1144, 2007.
- [151] R. Sinkus, M. Tanter, S. Catheline, J. Lorenzen, C. Kuhl, E. Sondermann, and M. Fink. Imaging anisotropic and viscous properties of breast tissue by magnetic resonance elastography. *Magn. Reson. Med.*, 53(2):372–387, 2005.
- [152] R. Sinkus, M. Tanter, T. Xydeas, S. Catheline, J. Bercoff, and M. Fink. Viscoelastic shear properties of in vivo breast lesions measured by MR elastography. *Magn. Reson. Imaging*, 23(2):159–165, 2005.
- [153] D. Smith, K. Uryu, K. Saatman, J. Trojanowski, and T. McIntosh. Protein accumulation in traumatic brain injury. *NeuroMol. Med.*, 4(1):59–72, 2003.
- [154] D. H. Smith, D. F. Meaney, and W. H. Shull. Diffuse axonal injury in head trauma. *J. Head Trauma. Rehab.*, 18(4):307–316, 2003.
- [155] D. M. Sosin, J. E. Sniezek, and D. J. Thurman. Incidence of mild and moderate brain injury in the United States and 1991. *Brain Inj.*, 10(1):47–54, 1996.
- [156] A. J. M. Spencer. *Continuum Theory of the Mechanics of Fibre-Reinforced Composites*. Springer-Verlag, 1984.
- [157] E. O. Stejskal. Use of spin echoes in a pulsed magnetic-field gradient to study restricted diffusion and flow. *J. Chem. Phys.*, 43:3597–3603, 1965.
- [158] E. O. Stejskal and J. E. Tanner. Spin diffusion measurements: spin echoes in the presence of time-dependent field gradient. *J. Chem. Phys.*, 42:288–292, 1965.

- [159] K. J. Streitberger, I. Sack, D. Krefting, C. Pfüller, J. Braun, F. Paul, and J. Wuerfel. Brain viscoelasticity alteration in chronic-progressive multiple sclerosis. *PLoS One*, 7(1):e29888, 2012.
- [160] K. J. Streitberger, E. Wiener, J. Hoffmann, F. B. Freimann, D. Klatt, J. Braun, K. Lin, J. McLaughlin, C. Sprung, R. Klingebiel, and I. Sack. In vivo viscoelastic properties of the brain in normal pressure hydrocephalus. *NMR Biomed.*, 24:385–392, 2010.
- [161] S. J. Strich. Diffuse degeneration of the cerebral white matter in severe dementia following head injury. *J. Neurol. Neurosurg. Psychiatry*, 19(3):163–185, 1956.
- [162] S. J. Strich. Shearing of nerve fibres as a cause of brain damage due to head injury: a pathological study of twenty cases. *Lancet*, 278(7200):443–448, 1961.
- [163] E. G. Takhounts, R. H. Eppinger, J. Q. Campbell, R. E. Tannous, E. D. Power, and L. S. Shook. On the development of the SIMon finite element head model. *Stapp Car Crash J.*, 47:107–133, 2003.
- [164] E. G. Takhounts, S. A. Ridella, V. Hasija, R. E. Tannous, J. Q. Campbell, and et al. Investigation of traumatic brain injuries using the next generation of simulated injury monitor (SIMon) finite element head model. *Stapp Car Crash J.*, 52:1–31, 2008.
- [165] P. A. Taylor and C. C. Ford. Simulation of blast-induced early-time intracranial wave physics leading to traumatic brain injury. *J. Biomech. Eng.*, 131(6):061007, 2009.
- [166] K. L. Thibault and S. S. Margulies. Age-dependent material properties of the porcine cerebrum: effect on pediatric inertial head injury criteria. *J. Biomech.*, 31(12):1119–1126, 1998.
- [167] D. J. Thurman, C. Alverson, K. A. Dunn, J. Guerrero, and J. E. Snieszek. Traumatic brain injury in the United States: A public health perspective. *J. Head Trauma. Rehab.*, 14(6):602–615, 1999.
- [168] H. C. Torrey. Bloch equations with diffusion terms. *Phys. Rev.*, 104:563–565, 1956.
- [169] X. Trosseille, C. Tarriere, F. Lavaste, F. Guillon, and A. Domont. Development of a F.E.M. of the human head according to a specific test protocol. In *36th Stapp Car Crash*, 1992.
- [170] N.W. Tschoegl. *The Phenomenological Theory of Linear Viscoelastic Behavior: An Introduction*. Springer-Verlag, 1989.

- [171] K. Uryu, H. Laurer, T. McIntosh, D. Pratico, D. Martinez, S. Leight, V. M. Lee, and J. Q. Trojanowski. Repetitive mild brain trauma accelerates Abeta deposition, lipid peroxidation, and cognitive impairment in a transgenic mouse model of Alzheimer amyloidosis. *J. Neurosci.*, 22(2):446–454, 2002.
- [172] J. A. van Dommelen, T. P. van der Sande, M. Hrapko, and G. W. Peters. Mechanical properties of brain tissue by indentation: interregional variation. *J. Mech. Behav. Biomed. Mater.*, 3(2):158–166, 2010.
- [173] E. E. Van Houten, K. D. Paulsen, M. I. Miga, F. E. Kennedy, and J. B. Weaver. An overlapping subzone technique for MR-based elastic property reconstruction. *Magn. Reson. Med.*, 42(4):779–786, 1999.
- [174] J. Vappou, E. Breton, P. Choquet, C. Goetz, R. Willinger, and A. Constantinesco. Magnetic resonance elastography compared with rotational rheometry for in vitro brain tissue viscoelasticity measurement. *Magn. Reson. Mater. Phys.*, 20:273–278, 2007.
- [175] D. C. Viano, I. R. Casson, E. J. Pellman, L. Zhang, I. A. King, and K. H. Yang. Concussion in professional football: brain responses by finite element analysis: part 9. *Neurosurgery*, 57:891–916, 2005.
- [176] G. B. Whitham. *Linear and Nonlinear Waves*. Wiley, 1974.
- [177] J. Wuerfel, F. Paul, B. Beierbach, U. Hamhaber, D. Klatt, S. Papazoglou, F. Zipp, P. Martus, J. Braun, and I. Sack. MR-elastography reveals degradation of tissue integrity in multiple sclerosis. *NeuroImage*, 49(3):2520–2525, 2010.
- [178] M. Yin, J. Talwalkar, K. Glaser, A. Manduca, R. Grimm, P. Rossman, J. Fidler, and R. Ehman. Assessment of hepatic fibrosis with magnetic resonance elastography. *Clinical Gastroenterology and Hepatology*, 5:1207–1213, 2007.
- [179] M. Yin, J. Woollard, X. Wang, V. E. Torres, P. C. Harris, C. J. Ward, K. J. Glaser, A. Manduca, and R. L. Ehman. Quantitative assessment of hepatic fibrosis in an animal model with magnetic resonance elastography. *Magn. Reson. Med.*, 58(2):346–353, 2007.
- [180] J. Zhang, M. A. Green, R. Sinkus, and L. E. Bilston. Viscoelastic properties of human cerebellum using magnetic resonance elastography. *J. Biomech.*, 44(10):1909–1913, 2011.
- [181] L. Zhang, K. H. Yang, R. Dwarampudi, K. Omori, T. Li, and et al. Recent advances in brain injury research: a new human head model development and validation. *Stapp Car Crash J.*, 45:369–394, 2001.
- [182] L. Zhang, K. H. Yang, and A. I. King. A proposed injury threshold for mild traumatic brain injury. *J. Biomech. Eng.*, 126(2):226–236, 2004.

- [183] H. Zou, J. P. Schmiedeler, and W. N. Hardy. Separating brain motion into rigid body displacement and deformation under low-severity impacts. *J. Biomech.*, 40(6):1183–1191, 2007.

Vita

Erik H. Clayton

Date of Birth	July 29, 1979
Place of Birth	Grand Rapids, Michigan
Degrees	Ph.D. Mechanical Engineering, May 2012 M.S. Civil Engineering – Structures, May 2006 B.S. Summa Cum Laude, Civil Engineering, May 2003
Professional Experience	Engineer, Quartus Engineering Incorporated, 2006 – 2008 Sr. Eng. Assistant, ATA Engineering Inc., 2004 Eng. Intern, Mallia Engineering Company, 2002 – 2003
Awards	National Research Council Postdoctoral Fellowship (2012) National Science Foundation Graduate Research Fellowship Honorable Mention (2003)
Journal Publications	Bayly, P. V., Clayton, E. H. , Genin, G. M. (2012) Quantitative Imaging Methods for the Development and Validation of Brain Biomechanics Models. <i>Ann. Rev. Biomed. Eng.</i> (Accepted). Clayton, E. H. , Genin, G. M., Bayly, P. V. (2012) Transmission, Attenuation, and Reflection of Shear Waves in the Human Brain. (Submitted). Okamoto, R. J.*, Clayton, E. H.* , Bayly, P. V. (2011) Viscoelastic Properties of Soft Gels: Comparison of Magnetic Resonance Elastography and Dynamic Shear Testing in the Shear Wave Regime. <i>Phys. Med. Biol.</i> 56:6379-6400. (*Equal contributors.)

Select
Conference
Proceedings

Clayton, E. H., Garbow, J. R., Bayly, P. V. (2011) Frequency-Dependent Viscoelastic Parameters of Mouse Brain Tissue Estimated by MR Elastography. *Phys. Med. Biol.* 56:2391-2406.

Clayton, E. H., Genin, G. M., Bayly, P. V., “Viscoelastic Properties of Living Human Brain by Local Frequency Estimation Applied to Distortional Wave Fields,” *ASME Summer Bioengineering Conference, Fajardo, Puerto Rico, June 20–23, 2012*. **Award:** [Finalist Ph.D. Paper Competition](#).

Clayton, E. H., Priatna, A., Bolster, B. D., Bayly, P. V., “Quantitative Measurement of Brain Deformation Caused by Pressure Loading of the Skull,” *International Society for Magnetic Resonance in Medicine, Montreal, Canada, May 7–13, 2011*. **Award:** [Educational Stipend](#).

Clayton, E. H., Garbow, J. R., Bayly, P. V., “Strain Rate Dependent Response of Brain Tissue Measured by MR Elastography,” *16th US National Congress of Theoretical and Applied Mechanics, State College, Pennsylvania, June 27–July 2, 2010*. **Award:** [Travel Stipend](#).

Clayton, E. H., Genin, G. M., Bayly P. V., “Response of the Brain to Oscillating Pressure on the Skull Quantified by MR Elastography,” *National Neurotrauma Symposium, Las Vegas, Nevada, June 14–17, 2010*. **Award:** [Top Abstract](#).

Clayton, E. H., Wang Q., Song, S. K., Okamoto, R. J., Bayly, P. V., “Magnetic Resonance Elastography of the Mouse Vitreous Humor In Vivo,” *SEM Annual Conference and Exposition on Experimental and Applied Mechanics, Indianapolis, Indiana, June 7–10, 2010*. **Award:** [Best Doctoral Paper](#).

Clayton, E. H., Garbow, J. R., Bayly, P. V., “Frequency Dependence of Mouse Brain Tissue Stiffness Measured in vivo with MR Elastography,” *International Society for Magnetic Resonance in Medicine, Stockholm, Sweden, May 1–7, 2010.*
Award: [Educational Stipend.](#)

Clayton, E. H., Wang Q., Song, S. K., Bayly, P. V., “Non-invasive Measurement of Vitreous Humor Stiffness in the Mouse using MR Elastography,” *International Society for Magnetic Resonance in Medicine, Stockholm, Sweden, May 1–7, 2010.*
Award: [Educational Stipend.](#)

Clayton, E. H., Genin, G. M., Bayly, P. V., “Wave Propagation in the Human Brain and Skull Imaged in vivo by MR Elastography,” *Southern Biomedical Engineering Conference, University Park, Maryland, April 30–May 2, 2010.*
Award: [Best Doctoral Paper.](#)

Clayton, E. H., Qian, Y., Orjih, O., Dyke, S. J., Mita, A., Lu, C., “Off-the-Shelf Modal Analysis: Structural Health Monitoring with Motes,” *24th International Modal Analysis Conference, St. Louis, Missouri, January 31–February 3, 2006.*
Award: [D. J. DeMichele Award.](#)

Clayton, E. H., Koh, B. H., Xing, G., Fok, C. L., Dyke, S. J., Lu, C., “Damage Detection and Correlation-based Localization Using Wireless Mote Sensors,” *13th Mediterranean Conference on Control and Automation (MED05), Limassol, Cyprus, June 27-29, 2005.*
Award: [Best Session Presentation.](#)

Invited Talks

National Institute of Standards and Technology
Physical Measurement Laboratory - Magnetics Group
Boulder, Colorado, July 2011.

University of Illinois - Chicago
Department of Bioengineering
Chicago, Illinois, September 2011.

59th (NMR)2 Meeting**

Albuquerque, New Mexico, November 2011.

ABQMR

Albuquerque, New Mexico, November 2011.

ExxonMobil

Upstream Research Corporation
Houston, Texas, January 2012.

University of Illinois - Chicago

Department of Bioengineering
Chicago, Illinois, February 2012.

The Ohio State University

Department of Radiology
Columbus, Ohio, February 2012.

Uniformed Services University

Department of Radiology
Bethesda, Maryland, March 2012.

**Professional
Societies**

National Society of Professional Engineers (NSPE)
American Society of Mechanical Engineers (ASME)
International Society for Optics and Photonics (SPIE)
Society for Experimental Mechanics (SEM)
Int'l Soc. for Magnetic Resonance in Medicine (ISMRM)
National Neurotrauma Society (NNS)

May 2012

MRE of the Brain, Clayton, Ph.D. 2012